A THESIS

FOR THE DEGREE OF DOCTOR OF PHILOSOPHY

Improved Detectors of 24 GHz UWB Short Range Radar system in Automotive Applications

Purushothaman Surendran

Department of Electrical and Electronic Engineering

GRADUATE SCHOOL

JEJU NATIONAL UNIVERSITY

2013. 02

Improved Detectors of 24 GHz UWB Short Range Radar system in Automotive Applications

Purushothaman Surendran

(Supervised by Professor Seok-Jun Ko)

A thesis submitted in partial fulfillment of the requirement for the

Degree of Doctor of Philosophy

2013. 02

The thesis has been examined and approved.

.....

Thesis director, Yang-Hoi Doh, Professor, Department of Electronic Engineering

.....

Seok-Jun Ko, Professor, Department of Electronic Engineering

.....

Dr. Jong-Hun Lee, Daegu Gyeongbuk Institute of Science & Technology

.....

Kyung-Youn Kim, Professor, Department of Electronic Engineering

.....

Min-Jae Kang, Professor, Department of Electronic Engineering

2013. 02

.....

Date

Department of Electrical and Electronic Engineering

GRADUATE SCHOOL

JEJU NATIONAL UNIVERSITY

REPUBLIC OF KOREA

Dedicated to

My beloved parents and my wife

Acknowledgements

One of the greatest joys of completion of this dissertation is to look back the past journey and cherish the moments with all the family and friends who have made it possible, during the tough times. Mere “THANKS’ will not suffice to express my heartfelt gratitude to all of them.

First and foremost, I heartily thank my parents, parents-in-law, my beloved wife, brother, brother-in-law, and sister for their patience and unequivocal support and persistent love throughout my life, without whom i would have not crossed the barriers in life with ease.

My heartfelt gratitude and thanks to my supervisor Seok-Jun Ko. In the past four years, I have adored him as a philosopher, guide and principle centered person who has always brought out the best in me and not less. When I am lost in the fog of my research, his guidance at the prompt time, had built a challenging competency in me. Sans of his guidance and supervision, my enthusiasm and productivity in research would have reduced to a great extent. Not to mention his knowledge on Radar systems, his overly enthusiasm, integral view on research had made an incredible effect on the success of our team. Last by no means the least, iam really grateful to have professor Seok-Jun Ko in my life.

As a vital cog in my research team, Dr. Jong-Hun Lee deserves special thanks for his guidance, inspiring suggestions, and encouragement throughout my research period and during writing of this dissertation. His deep insights and wide knowledge in the field of UWB SRR was always of great assistance.

I would also thank the other members of my Ph.D. committee who monitored my work and kindly spared their time in reading and providing me with valuable suggestions in the earlier versions of thesis: Dr. Jong-Hun Lee, Prof. Yang Hoi Doh, Prof. Kyung Youn Kim and Prof. Min Jae Kang I thank you all. Also, I acknowledge with great thanks to the professors of my department Prof. Kyung-Sik Kim, Prof. Kwang-Man Lee, Prof. Yang Hoi Doh, Prof. Kyung-Youn Kim, Prof. Sung-Taek Ko, Prof. Min-Jae Kang for their inspiring and encouraging guidance for a deeper understanding of knowledge and conductive comments during my course work.

I owe a lot of gratitude and appreciation to people with whom I have worked directly or indirectly. Dr Myung-Hun Jang and Mr. Sang Dong Kim, who had helped me in my initial days had been my real mentor and had always provided constant support and motivation to achieve a higher altitude in life. It is enough to spend a few minutes with an expertise to gain

a renowned knowledge that will be memorable forever. In my research life, that was true with Dr. Bong Seok Kim, who had been very kind enough to guide me in using various tools like Latex and Matlab, which were highly significant during my research period.

Staying away from home is always challenging and tough and it is true that “A friend in need is a friend in deed”. My heartfelt special thanks to Dr. Gunasekaran, for his immense support during my hardships in Jeju. My life in Jeju was blessed with other intimate friends Dr. Anil, Dr. Hari, Dr. Ganesh, Dr. Shrikant, Dr. Saha, Dr. Ganesh Thangaraj, Dr. Karthikeyan, Dr. Rajneesh, Dr. Ahmar, Dr. Nauman, Dr. Ahsan, Dr. Mahinda, Dr. Neelesh, Dr. Simrinder Sodhi, Dr. Gandhi, Dr. Dharaneedharan, Naeem, Nandeesh, Chandran, Navaneethan, Saravanan, Thiyagarajan, Anantha kumar, Sebastian, Sridhar, Anji reddy, Ravi teja, Ajith, Anushka, Sanjaya, Niroshana, Umasuthan, Vivek, Zubair, Kamran Ali, Adnan Ali, Saleem, Arshad, Rahul, Murtuza and many more in Jeju. I thank them all with immense pleasure for making my life in Jeju a beautiful one with cherishable memories. I am indebted to all the members of JISO, for their strength and encouragement.

I am also grateful for the department of Electronic Engineering at Jeju National University for providing me an excellent work environment during my study and I also thank Suk-In Kang, Kyung Pill Ko and Sang-Cheol Yang for their cheerful assistance in the office work. Finally, I thank my lab mates Deayeon, Yeong Beom Ko, Park, and Sang Ho Lee for their kind help during my stay in Jeju.

I owe many thanks to Daegu Gyeongbuk Institute of Science & Technology (DGIST) and graduate School of Jeju National University for the financial support rendered during my studies. I thank Brain Korea 21 which provided the funds for presenting the research work held in Korea and abroad.

I would like to thank all those whom I have not mentioned above but helped me in numerous ways to my success.

Abbreviations and notations

UWB SRR	Ultra Wide Band Short Range Radar
RADAR	Radio Detection and Ranging
ACC	Adaptive Cruise Control
CA	Collision Avoidance
LRR	Long Range Radar
ADAS	Advanced Driver Assistance Systems
FCC	Federal Communications Commission
EIRP	Equivalent Isotropically Radiated Power
ETSI	European Telecommunications Standards Institute
CW	Continuous Wave
RF	Radio Frequency
DFT	Discrete Fourier Transform
FFT	Fast Fourier Transform
IFFT	Inverse Fast Fourier Transform
LO	Local Oscillator
PDF	Probability Density Function
IF	Intermediate Frequency
DSP	Digital Signal Processor
LNA	Low Noise Amplifier
PRI	Pulse Repetition Interval
PRF	Pulse Repetition Frequency
CFAR	Constant False Alarm Rate
RCS	Radar Cross Section
CPI	Coherent Pulse Interval
WGN	White Gaussian Noise
AWGN	Additive White Gaussian Noise
SNR	Signal-to-Noise Ratio
ADC	Analog to Digital Converter
FIR	Finite Impulse Response
IIR	Infinite Impulse Response
AR	Autoregressive

ACF	Autocorrelation Function
ZMNL	Zero-Mean nonlinear transformation
T_{PRI}	Pulse repetition interval
T_P	Pulse width
R_{max}	Maximum range
ΔR	Range resolution
N_c	Coherent integration number
N_{nc}	Non-coherent integration number
L	Sliding window
S/N, $\bar{E}/N_0$	Signal-to-noise ratio
τ	observation interval
P_D	Probability of detection
P_{FA}	Probability of false alarm
$\bar{E}$, E	Total received signal energy
p	a priori probability that the signal is present
q	a priori probability that the signal is absent
f_{PRF}	Pulse repetition frequency
A_T	Amplitude of single transmit pulse
f_c	Carrier frequency
φ_0	Initial phase of the transmit signal
φ_I	Phase of received signal
f_D	Doppler frequency
A_E	Amplitude of the received signal
S^2	Signal mean power
N_0	Noise power
N	Number of FFT points
Δf_D	Minimum Doppler frequency
Δv	Velocity resolution
T_{FFT}	FFT input time
K	Maximum range gate size
$T_{FFTmeasure}$	FFT measurement time

Contents

List of Figures

List of Tables

요약

이 논문에서는 자동차 응용 프로그램 분야에 필요한 UWB 레이더의 연구와 개발에 대하여 논하였다. 자동차 부문에서 24 GHz Ultra Wide Band short range radar는 도로 안전성과 승객의 안정을 높이고 충돌을 피하기 위한 좋은 발상으로서 최근 많은 관심을 받고 있다. UWB radar신호는 다른 신호 영역과 비교하여 고유의 주파수와 대역폭을 나타낸다. 24 GHz Ultra Wide Band Short Range Radar (UWB SRR)는 지정된 대상을 감지하기 위한 기술로 자동차 부문에서 그 수요가 크게 증가되고 있다. 이 연구에서는 자동차의 응용프로그램에 적용할 수 있는 24 GHz UWB SRR 감지기를 설계하는 것을 집중적으로 다루었다. 유럽 연합 집행 기관 European Commission 에서는 UWB SRR을 도로의 안전성을 향상시킬 수 있는 중요한 세계적인 기술 중 하나라고 발표했다. 또한 유럽에서는 자동차 응용프로그램에서 사용되는 주파수를 24 GHz 주파수 영역으로 고정하였다. 특히 UWB SRR에서 사용되는 주파수 영역은 21.625 GHz에서 26.625 GHz로 할당되었다.

이번 연구의 목적은 Monte Carlo 시뮬레이션을 이용하여 고정된 허위경고 가능성을 위한 24 GHz UWB SRR 감지기의 감지성능을 분석하는 것에 있다. 감지기의 감지 성능은 가우스 잡음 환경과 coherent weibull clutter 환경에서 고정되거나 이동하는 단일대상에 대하여 측정하였고 다수의 대상에 대해서는 다루지 않았다. 이 논문에서 보여주는 coherent weibull clutter 모델은 실제 도로에서 발생되는 상황과 거의 같도록 하였다. 또한 clutter 모델은 제로-평균 비선형 변환 블록 zero-mean non-linear transformation block (ZMNL) 을 사용하여 자동차 응용프로그램에 알맞은 clutter 환경으로 변경할 수 있도록 하였으며 다양한 도로사정에 따른 실험을 수행하여 고정 또는 이동 대상에 모두 적용할 수 있도록 하였다. 대상에서 반사되는 에너지가 분산된 경우 이번 연구에서 제안된 슬라이딩 윈도우 감지기 sliding window detector 는 현재 상용화된 감지기와 비교하였을 때 월등한 감지 성능을 가지고 있다. 모두가 아는 바와 같이 24 GHz UWB 감지기는 지정대상의 각 flare point 부터 반사되는 전체 에너지의 비율에 따라서 달라진다. 만약 UWB 신호와 같이 펄스나비 pulse width 가 매우 좁으면 에너지는 더 분산되며 이런 경우 슬라이딩 윈도우 감지기가 신호를 감지하기에 매우 적합하다. 마지막으로, 제안된 감지기는 시간과 기억장치를 효율적으로 사용할 수 있는 UWB 감지기로서 150 km/hr 이상인 지정대상의 최고상대속도를 측정할 수 있다.

논문에서 보여주는 pulse radar 는 먼저 대상 범위를 결정하고 결정된 범위 목록의 FFT 를 순차적으로 사용하여 지정대상의 속도를 계산한다. 그리하여 FFT 처리시간과 자동차 안전 응용 프로그램에서 사용되는 24 GHz UWB SRR 감지기의 기억장치의 요구사항을 줄일 수 있다. 이로써 자동차 응용 프로그램에서의 안전체계는 복잡한 하드웨어를 간소화하기 위해 최소의 처리시간과 적은 기억장치를 필요로 한다. 이 때문에 사고를 방지하고 많은 교통량을 확인하기 위해 사전충돌 및 에어백과 같은 안전장치에 대한 자동제동장치의 배치를 위한 반응시간이 우선적으로 순위가 부여된다.

1. Introduction

1.1 Radar Research and Development Challenges

The first RADAR (radio detection and ranging) system was invented by Christian Hulsmeyer (1881-1957) in 1904 to avoid vessel collisions on the river Rhine even in bad weather conditions. The first radar application was started intensively in the early 1970's considering road traffic situations. The idea behind this is to avoid vehicle collisions mainly in the cities where the traffic density is increasing day by day, e.g. to use it as an ACC (adaptive cruise control) system for comfortable driving and security of the passengers. The useful applications of radar sensors include parking aid system and pre-crash applications. Unlike airbag systems which react when an accident already happened, a radar system can even detect collisions before they happen and react very early to avoid an accident or minimize the consequences. Systems at the very early stage of development in the 1970s exceeded the acceptable geometrical product size for a passenger car, the target price for one unit and had a performance which was not yet convincing enough.

This situation changed in many aspects at the beginning of the 1990's, Microwave technology was now very much improved concerning cost and performance and a radar front-end became small enough to be integrated into a car. Additionally cost for processing hardware like DSPs (digital signal processors) decreased with still increasing processing power. Small and cheap electronic control units were now reality as well as the required low cycle times of a few milliseconds for a security system. Earlier experiences were picked up again and a very dynamic market of automotive radar system development was formed. Today almost all automotive companies and automotive system suppliers work on radar systems. It is important to be one step ahead in such a promising market. With a first forward looking 77 GHz pulse radar system of 150 m range, sold in cars since 1999, a leading car manufacturer broke the ice and showed that all key parameters e.g. like small cost at large volume production, size, performance can be fulfilled nowadays and that customers accept the functionality of an adaptive cruise control system as a security and comfort system [1].

Many publications describe the application of radar technology in modern passenger vehicles to meet the growing interest in security and safety systems. Until today most of the systems are narrow beam long range radars which are capable of measuring even targets of small radar cross section up to 150 m in front of the vehicle. Requirements for additional and future automotive radar applications (e.g. parking aid, pre-crash, stop & go) cannot be

fulfilled by typical ACC radars, due to some system limitations in angular coverage, range accuracy and range resolution, respectively. For this reason a completely new automotive radar system developed has been started years ago based on high powerful short range pulse radar sensors in the 24 GHz domain.

The Ultra Wide Band Short Range Radar technology is a new field of radar technology that uses ultra-short pulses of energy and complex trains for sensing. The distinguishing characteristic of ultra-wide band signals is their large ratio of instantaneous bandwidth to center frequency. For comparison, normal narrowband signals have bandwidth-to-center-frequency ratios that are around 0.01 or less, and wideband signals (e.g., spread spectrum signals) have bandwidth-to-center-frequency ratios that are about 0.01-0.25 [1]. However, UWB signals have a bandwidth-to-center-frequency ratios that are 0.25 or larger by the American definition (Russian texts classify UWB as having a bandwidth 100 percent of center frequency). Large bandwidth means that UWB signals can carry more information such as range resolution, target interaction, and data [1].

The radar system described in this thesis is based on short range radar of very high range resolution and accuracy. By means of ultra-short pulses of a pulse width below 2 ns, achieved by direct sampling of the received signal, a range resolution of a few centimeters can be realized. Range accuracy is below 30 cm for targets in a maximum range up to 15m [7].

The UWB short range radar also include a variety of applications such as

ACC support with stop & go functionality:

The warning of or reaction on cut-in collisions is a significant task for adaptive cruise control systems. Vehicles cutting in from adjacent lanes have to be detected very early to reduce speed in time. In very dense traffic situations this application can surely reduce a large amount of accidents.

The support of a long range radar sensor for adaptive cruise control and CA (collision avoidance) is possible. Long range radars show limitations e.g. in their angular coverage in azimuth. With such very narrow beam radars it is usually not possible to monitor the vehicle front corners which are also critical directions for accidents as shown in Fig. 1.1. Range accuracy and resolution in the very near range in front of the vehicle are also better if high resolution radars are used.

Blind Spot Detection:

Overseeing passing vehicles or vehicles on adjacent lanes by an inattentive driver can be avoided by a blind spot detection function of the sensor network. At least an acoustic warning for the driver in a critical situation would be very helpful.

Rear End Collision Warning:

Rear end collision warning can also be used like all other applications to initiate system reactions early in case of an accident, e.g. activating the airbags inside the vehicle or the brakes if a collision with a fast vehicle from the back cannot be avoided. This application can be seen as a special case of a complete pre-crash system monitoring only the rear of the car.

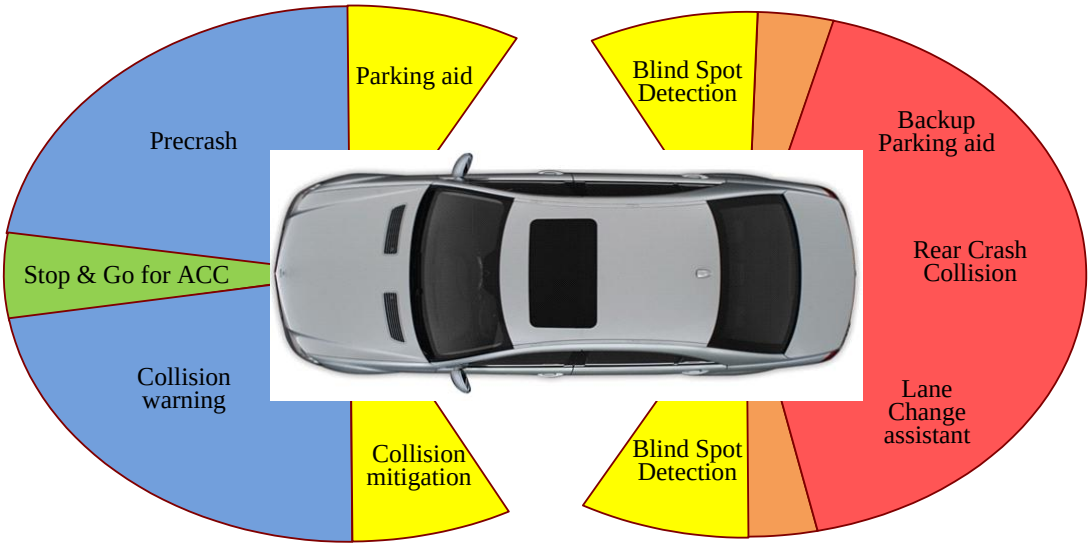

Figure 1.1 Short Range Radar–different kinds of applications.

Pre-Crash:

Last but not least the application of a radar sensor surrounding the vehicle for a so-called pre-crash application is an important development. The main idea is to react very fast with a pre-crash sensor and activate all necessary active components (brakes, or even steering) in the car to avoid an accident or at least minimize consequences of an impact with reduction of the vehicle's kinetic energy. Early activation of airbags is very important.

UWB Radar appears to be the best for automotive applications since it generates an Ultra-wideband pulse signal which is about a nanosecond in duration. In addition to this short duration pulses, these devices can be made with very high pulse repetition frequencies

on the order of 1 MHz (1 μs pulse repetition interval). Varying the interval between pulses can modulate the signals to carry information. By using correlation of pulse interval coded signals, these devices can measure distances very exactly. The UWB applications suggested here will use very low radiated power levels, usually less than a mill watt. These capabilities are possible with current solid state electronics and low-cost chips can be made to perform a wide range of applications, also UWB devices are relatively simple and accurate at an affordable price.

1.2 International technology development status

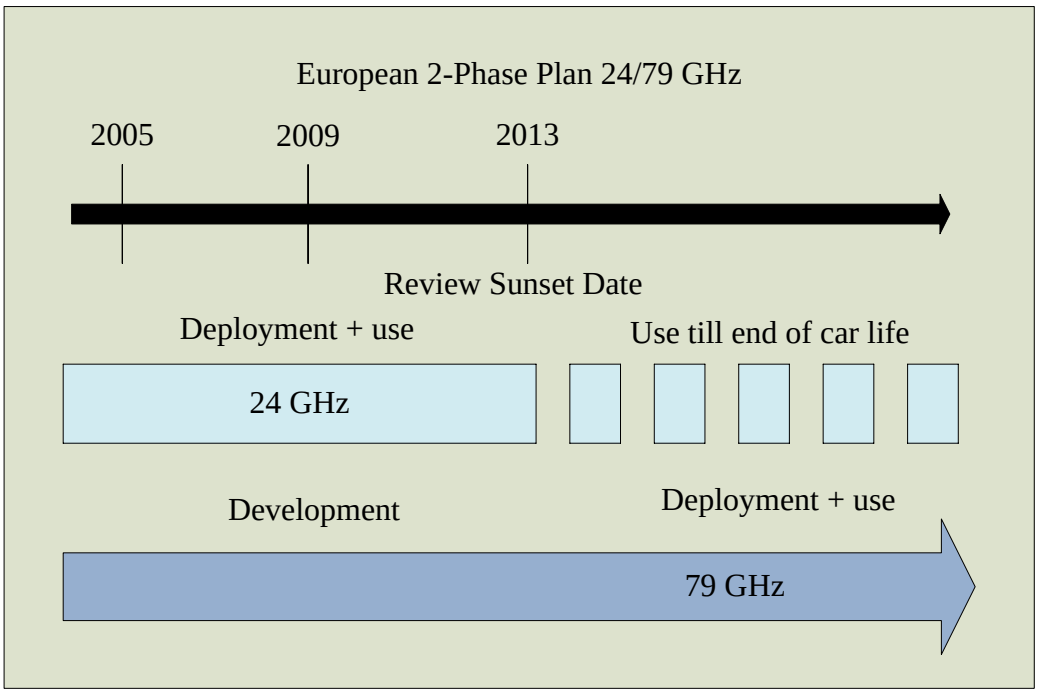

Figure 1.2 "PACKAGE SOLUTION" for automotive short range radar in Europe.

A consortium of automobile manufacturers and suppliers known as the SARA (Short Range Automotive Radar Frequency Allocation) is working on the allocation of 24 GHz frequency for UWB automotive radar worldwide. In USA, approval of the 24 GHz band was already granted unlimited in time and system numbers in 2002 by the US regulation authorities [1]. In Europe, on 17 January 2005 the European Commission approved the decision on allocation of the 24 GHz frequency band for automotive short-range radar. From 1 July 2005 until 30 June 2013 UWB automotive short range radar are being used temporarily and also includes the work towards an early introduction of equipments operating in 79 GHz band by means of research and development program [1]. From mid of 2013, new

cars have to be equipped with SRR sensors which operate in the frequency range between 77-81 GHz. The European approach of temporary use of 24 GHz with a transition to 79 GHz is called “PACKAGED SOLUTION”.

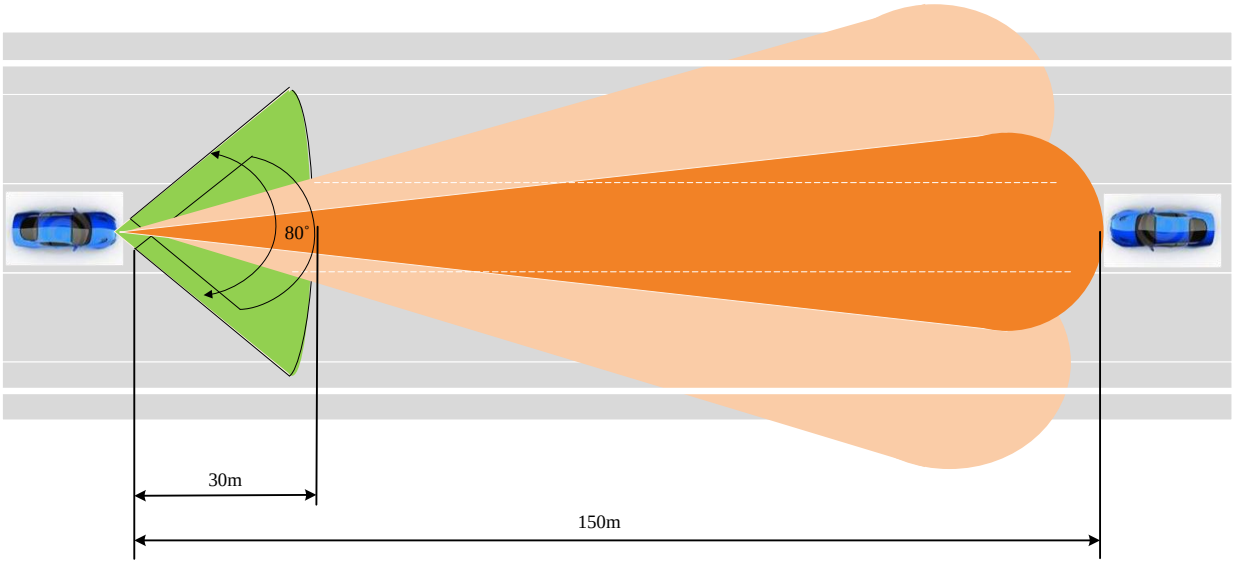

Figure 1.3 Combination of SRR and LRR for advanced safety features.

Especially the combination of LRR and SRR provides valuable data for advanced driver assistance systems (ADAS). Part of this has been realized for the first time in the Mercedes Benz S-Class, which has been celebrated its world premiere in autumn of 2005. In the new S-class, two radar systems are offered to monitor the traffic situation in front of the vehicle, which indicate newly developed short range radar based on 24 GHz technology works in tandem with the tired and proven 77 GHz radar employed in the DISTRONIC proximity cruise control system [1]. The two systems complement each other well; the DISTRONIC radar is designed to be able to track three motorway lanes over a distance of up to 150 meters with an angle of nine degrees and the new 24 GHz radar uses an angle of 80 degrees to monitor the immediate area up to 30 meters in front of the vehicle as shown in Fig. 2a [1].

The radar technology will be used to determine the distance to vehicles ahead, warn drivers when they get too close, and provide the necessary braking power if it appears that a collision is unavoidable. In those situations where drivers are forced to brake, the new brake assist PLUS system will calculate and generate the braking force needed for a given situation within fractions of a second.

1.3 Development of 24GHz UWB SRR in automobile industry

Stage 1 – Identification/description of the problems

In 2004, two frequency bands were identified for the introduction of automotive UWB SRR (Short Range Radar) technology in Europe:

- the 24 GHz frequency range (i.e. 21.65-26.65 GHz), as a temporary band for UWB SRR systems (24 GHz UWB SRR)
- the 79 GHz frequency range (i.e. 77-81 GHz), as a permanent band for UWB SRR systems (79 GHz UWB SRR)

The European frequency regulation currently requires UWB SRR to migrate from 24 GHz to 79 GHz spectrum in the year 2013. Decision 2005/50/EC on the 24 GHz frequency range stipulates that a fundamental review of the Decision should be carried out by 31 December 2009 [2].

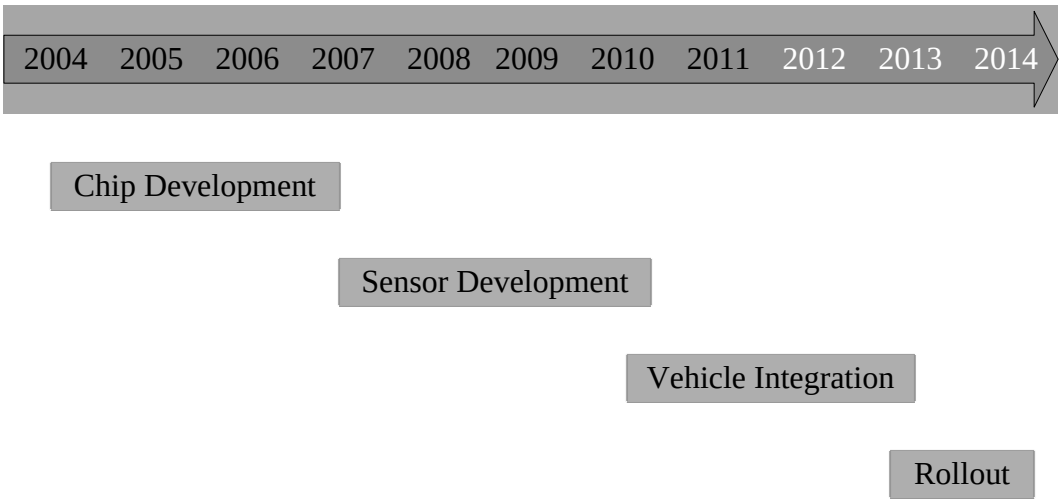

Figure 1.4 Time schedule towards the development and rollout of 79 GHz.

Stage 2 – Describe the policy issue and identify the objectives

The European Union's eSafety Initiative in 2003 established the goal to reduce the number of road fatalities by 50% up to the year 2010. There are over 40,000 fatalities on the EU25 roads every year, resulting from 1.4 million accidents, with an equivalent cost of around euro 200 billion/year, or 2% of EU GDP.

Some of the key constraints of car manufacturers are well described in CEPT Report 36 developed in response to Part 1 of the EC mandate on SRR, in particular the fact that the technology to be used in a car line must be fixed several years before start of production (SOP). A phase of car integration and extensive car tests will require several years in addition to the research and technology development phase in order to ensure that all safety aspects are correctly implemented. After product design, the release for series production in a car line is possible with modern production systems with a lead time of 2 to 4 years after sensors are available for car integration. During the production time of a car line a change of technology is very difficult. Strategic Automotive Radar frequency Allocation group (SARA) has provided in its response to the questionnaire on SRR the Fig. 1.6 below that illustrate the typical product life cycle (about 15 years) of a car line [2]-[3].

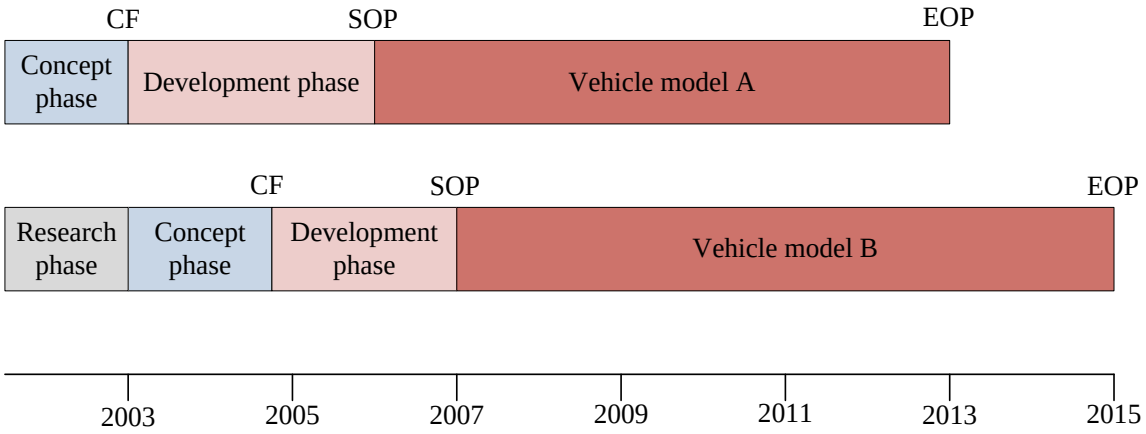

CF : Concept Freeze
SOP : Start of Production
EOP : End of Production

Figure 1.5 Research, Development and Production Cycles in the Automotive Industry.

ACEA (Association of European automotive manufactures) has also underlined the research and development up to 7 years, production time 7 to 8 years, vehicle life time of about 15 years. Statistics studies of direction of impacts on a vehicle from the institute GIDAS (German In-Depth Accident Study) – and NHTSA (National Highway Traffic Safety Administration) show that accidents on the lateral parts and rear parts of a vehicle are also important in comparison with the front of a vehicle. The global safety includes radar applications indicated in Appendix 1 of CEPT report 37 and the passive safety (seat belt pretension and airbags pre-firing for frontal and side/rear impact and whiplash prevention for side/rear impact).

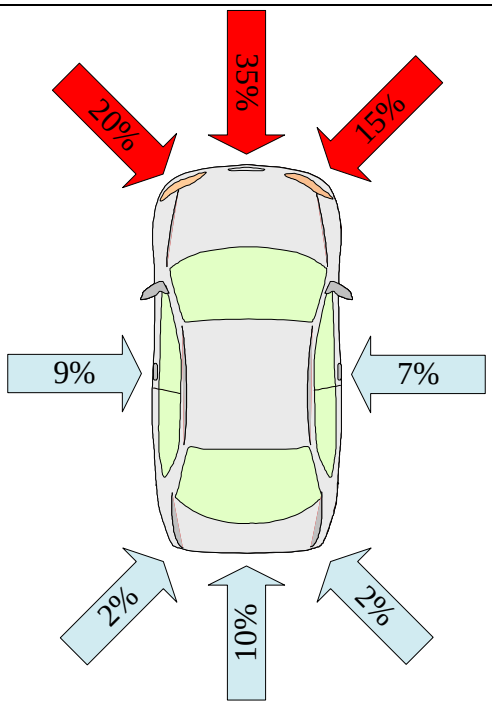

Collision Statistics :
GIDAS 13/12/06

Collisions statistics of frontal safety (70%).

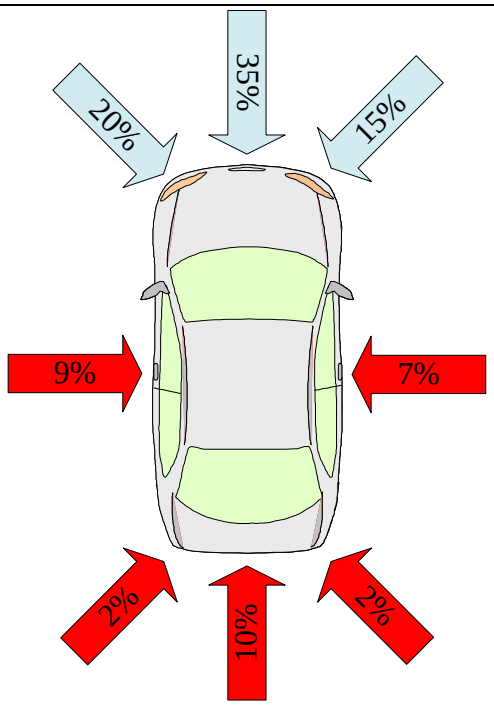

Collision Statistics :
GIDAS 13/12/06

Collisions statistics of rear and side safety (30%).

Figure 1.6 Collision Statistics.

1.4 Past and Present UWB Technology Work and Sources

There are a number of efforts across the world to develop UWB in to marketable devices. It is highly likely that UWB products may become commonplace due to their low cost and wide range of applications.

Dr. Henning Harmuth did much of the important early theoretical work in non sinusoidal impulse technology. He was with Catholic University in Washington for many years until he retired a few years ago. Now he still works on his own with Russian, Ukrainian, and other foreign researchers to develop a large current antenna device to make UWB devices capable of transmitting extremely high power [4].

Dr. Merrill I. Skonik, well known as the author of introduction to radar systems and editor of the radar handbook, was a long time Director of Radar for the Naval Research Laboratory in Washington, D.C. He became interested in UWB radar for military applications in 1980 and has written technical papers on the subject he has pursued UWB as a personal area of interest [6].

In 1994, Lawrence Livermore Laboratories announced the successful development of the Micro power Impulse Radar (MIR). They are currently licensing the technology for various commercial applications. They have released specifications for a wide range of chips with many potential applications including medical, speech, security, energy conservation, residential, commercial, industrial automation, transportation, and communication. The MIR devices are estimated to cost about $10 in sufficient production quantities, so the low cost and advantages of radar over competing technologies will make it competitive with ultrasonic and optical sensors. Amerigon has recently acquired a Lawrence Livermore license to investigate MIR technology for short-range vehicle applications [4].

Aetherwire & Location, Inc., based in California, continues to do some of the most advanced work on cooperative UWB location and communication. They have used ARPA funds and venture capital to develop a chip that can co-locate other chips with centimeter accuracy and communicate with the devices. These devices will use cooperative ranging and be capable of much longer ranges than the Lawrence Livermore devices that use a one-way travel path. Also, they have implemented a sophisticated receiver front end to carry out a large amount of signal correlation that can uniquely identify each chip. Indications from the company are that the devices can be made for $20 in quantity. As the system is released, more information will be made available to the public.

Pulson Communications is a small company that has a number of patents on UWB technology as it related to communications. The company has made breadboard-type demonstrations of UWB communications over long ranges. One demonstration involved sending music over a link separated by several kilometers. Also they have worked with Professor R. A. Scholtz, from the University of Southern California, to show the multiple access communication capabilities of UWB technology.

Lieutenant Colonel James D. Taylor, USAF (retired), edited and published Introduction to Ultra-wideband Radar Systems in 1995. This was the first book specifically written to present a complete overview of ultra-wideband theory, phenomenology, technology, and systems design. The annual SPIE Aerosense technical conferences have been the principal UWB technical forum since 1992. These yearly conferences present the latest work in UWB radar and related signal processing. The IEEE Radar Electromagnetic Compatibility annual conferences also present UWB work. There are also yearly conferences on ground probing radar sponsored by NIST and the electromagnetic pulse (EMP) conferences sponsored by the U.S. Air Force Philips Laboratory in Albuquerque, NM, which cover related technology and practical applications [4]-[5].

At the 1995 ITS America annual meeting, authors from the Virginia Tech Center for Transportation Research (CTR) published a paper titled "An Infrastructure Controlled Cooperative Approach to automated Highways." The National Automated Highway System Consortium selected that concept as one of the initial concepts it will explore. At this stage, there are many concepts being studied, and only a few will be chosen by the consortium for prototype development.

Prof. Hermann Rohling is with the Technical University Hamburg-Harburg, Germany where he has developed an international reputation for radar signal processing, CFAR detection theory and FMCW waveform design especially in the application field of automotive radars. Smart Microwave Sensors Company is a specialist in Radar technology founded by Professor Hermann Rohling and Dr Ralph Mende. It has been working with automotive customers since its founding in 1997. Today not only automotive radars are being developed, but the successful business has been extended to other fields of radars such as traffic radar, security radar, and airborne radar [7].

In 2002, Michael Klotz has described about short range radar sensors of very high range resolution and accuracy. By means of Ultra-short pulses of a pulse length of below 1 ns, technically achieved by high speed switches, a range resolution of few centimeters can be realized. Range accuracy is below 3 cm for all targets in a maximum range up to 20 m. Due to the fact that the technology is very cheap, numerous of these small sensors surrounding even the complete vehicle. Radars of this performance were never used before in a sensor network for automobiles and a network of this kind is also a new development [9]-[10].

In 2003, F. Kruse *et al*. described about classification of object with automotive radar [11]. In 2004, Ian Gresham *et al.* presented an overview of the requirements for UWB short-range sensors in automotive applications. Also, described about second generation pulsed short range radar sensors, time gated correlation receiver architecture, and generic short range sensor requirements for object detection [12]. In 2005, Dr Ralph Mende introduced 24GHz radar sensor applicable for advanced driver assistance system function ACC (Adaptive Cruise Control) on automobiles [13]. Meinecke *et al.* presented a radar system for side-pre-crash recognition for passenger cars in 2006 [14]. Pedestrian detection and recognition with UWB radar sensors by Rohling *et al*. in 2007; Kouemou in 2008; He *et al.* in 2010; Benitez *et al*. in 2011; mostly used complex signal features, machine learning for classification and often human gait models for interpreting micro Doppler signatures [15]-[17]-[18]-[19]. The impact of the pedestrian's direction of movement, occlusion, antenna beam elevation angle, linear vehicle movement, and other factors are investigated and discussed in A. Bartch *et al*. in 2012

[20]. In 2012, Bruno Neri *et al* discussed the architecture, performance of pulsed and CW highly integrated radars and the design criteria for FMCW and pulsed radars [21].

1.5 Scope and Contents of the Thesis

The purpose of this dissertation is to analyze the detection performance of proposed 24 GHz UWB SRR detector for fixed false alarm probability by using Monte Carlo simulation. The detection performance of proposed detectors is analyzed in Gaussian noise environment and coherent weibull clutter environment for single stationary and moving target. Therefore, multiple target case is not considered in this dissertation. The coherent weibull clutter model developed in this dissertation is more appropriate to actual road clutter in real situation. Also, the clutter model can be changed to the most appropriate clutter environment for automobile applications by using zero-mean non-linear transformation block (ZMNL) for both stationary and moving target by performing experiments on various road conditions. The proposed sliding window detector has better detection performance in comparison with the conventional detector when the energy reflected from the target is more distributed. As we know detection performance of 24 GHz UWB detectors depends on the percentage of total energy reflected from each flare point of the target. If the pulse width is very narrow such as UWB signal, then the energy is more spread and the proposed detector with sliding window is superior. Finally, the proposed detector is a time and memory efficient UWB SRR detector for measuring the target maximum relative velocity of up to 150 km/hr. The proposed pulse radar first decides the target range and then computes the target velocity by using FFT at the decided range index sequentially. Therefore, we can reduce the FFT processing time and the memory requirement of proposed 24 GHz UWB SRR detector used for automobile safety applications. Since, the safety system used in automobile applications requires minimum processing time and less memory in order to reduce the hardware complexity. Because, the reaction time for the deployment of auto braking systems for pre-crash and security devices such as airbags are given high priority in order to avoid accidents or simply to monitor a high traffic road.

This thesis contains five chapters. Chapter 1 gives a brief introduction about UWB radar research and development challenges in the field of automotive applications, the unique nature of the UWB radar signal by comparing its frequency and bandwidth with the other bands of signal and the current status and development of 24 GHz short range radar. It also

presents the application of 24 GHz Ultra Wide Band short range radar in automobile sector with an idea to avoid collision and increase road safety and passenger's security.

Chapter 2 deals with the automotive radar technology development standards, the key elements of the part 153 ruling governing UWB radars for vehicular applications and the associated spectrum mask. Finally, it presents the parameter specification and the information available for the UWB radar echo.

In chapter 3, the correlated coherent weibull clutter generation method is presented. First, a coherent correlated Gaussian sequence obtained from coherent white Gaussian noise is presented. Secondly, coherent correlated weibull sequence obtained from the generated coherent correlated Gaussian sequence is explained. The developed clutter model is more appropriate to actual road situation. It also presents the mathematical procedure and corresponding statistical properties to obtain correlated weibull sequence for 24GHz UWB SRR system in automobile applications.

Chapter 4 and 5 present the core part of the thesis. Two cases are described, first is the stationary target case and the other for moving target case. Chapter 4 deals with the stationary target case in which the conventional and proposed UWB SRR detector is explained. The detection performance of proposed and conventional detector in Gaussian noise environment and weibull clutter environment for stationary target case is analyzed and discussed.

Chapter 5 is about moving target case. The proposed and conventional UWB SRR detector is described. First, the detection performance of proposed and conventional detector is analyzed in Gaussian noise environment. Secondly, the correlated coherent weibull clutter using experimental datas developed in chapter 2 is used to analyze the detection performance of proposed and conventional detector in weibull clutter environment.

Finally, in chapter 6 the conclusions of the dissertation are given.

2. Automotive Radar Technology Development Standards

2.1 Global Deployment of 24GHz UWB-SRR

US: Regulation in force - since February 2002

EU: European Commission decided- February 2005

Russia: verbally confirmed - 7 May 2007

Australia: regulated in July 2006

Canada: Frequency allocation from first half of 2007.Interim allowance was given to start using vehicles equipped with UWB SRR.

Japan: Compatibility Study group since December 2006.

Since cars are offered worldwide, a globally harmonized frequency regulation is very important. More than 50 countries in the world have approved 24GHz UWB SRR for contribution to their road safety.

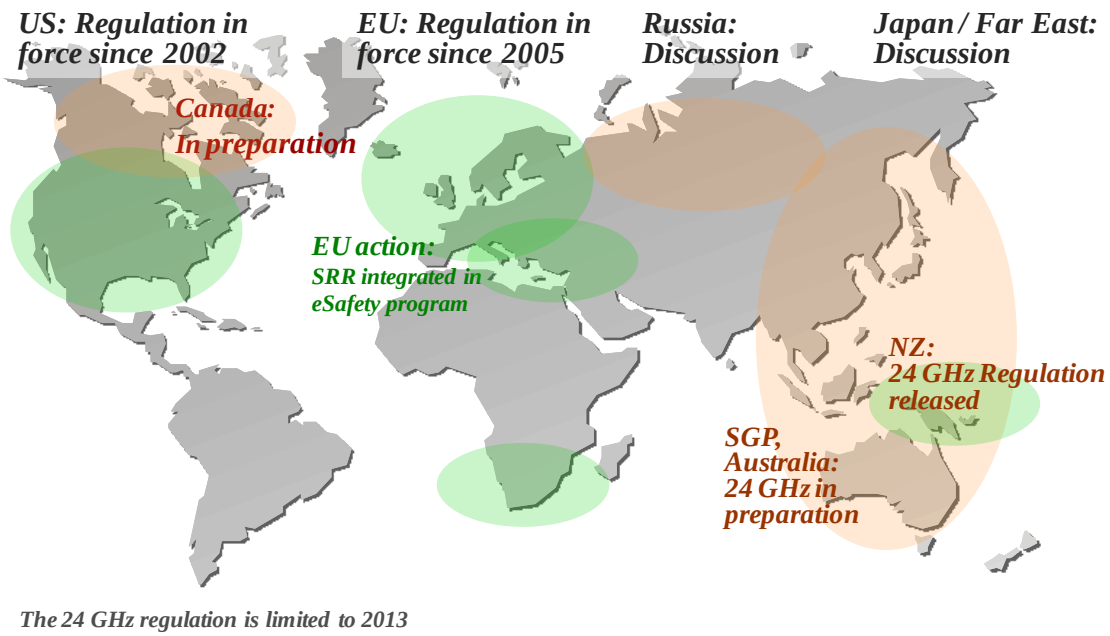

Figure 2.1 Global Deployment of 24GHz UWB Short Range Automotive Radars.

2.2 FCC part 15 Ruling

The specification is written in terms of an emitted power spectral density, or effective isotropic radiated power (EIRP), which allows for either a reduction in the peak transmitted power or, as is more likely, a reduction in the elevation side lobes of the Tx antenna. Similar

proposals in Europe are at the time of writing still under consideration by the ETSI. One mitigating solution that is the subject of much research notably by the Radar net consortium is the proposal by SARA in conjunction with the European Radio or ten years after their introduction, whichever is later. In conjunction, SRR sensors would slowly migrate in frequency to be based at 79 GHz. This would set an upper limit on the maximum number of sensors produced at 24 GHz and, thus, limit the increase in background noise that the EESS sensors would be exposed to. It should be noted that the corresponding spectrum at 79 GHz has also yet to be allocated [12].

Table 2.1 Key Elements of FCC Ruling Governing UWB Radars.

FCC UWB Ruling, FCC 02-48,Section 15.515
Sensor operating only when engine running, or upon specific activation
Minimum Signal bandwidth 20% or 500 MHz(whichever is smaller) (Bandwidth defined as -10dB below peak emission points)
Bandwidth contained between 22GHz – 29GHz Centre frequency greater than 24.075GHz
Average Radiated Emission (22GHz to 29GHz) Limited to -41.3 dBm EIRP, 1MHz BW, 1ms average
Peak Radiated Emission 0dBm EIRP in 50MHz around highest emission frequency
Emission 23.6GHz-24GHz 30°above horizon -25dB below spec limit by 2005 -30dB below spec limit by 2010 -35dB below spec limit by 2014

Table 2.1 summarizes the key elements of the Part 153 ruling governing UWB radars for vehicular applications. The associated spectral mask is illustrated in Fig. 2.2. To be considered an UWB device, the fractional bandwidth of the spectrum measured at the 10-dB point from the peak must be at least 20% or 500 MHz, regardless of the fractional bandwidth. The vehicular radars must operate between 22–29 GHz in such a way that the center frequency and the frequency at which the highest level emission occurs must be greater than 24.075 GHz. Thus, to be considered UWB, the vehicular radar must have at least 500-MHz

bandwidth to satisfy the regulations. Normally, the spectral density of the average mission in this band should not exceed 41.3 dBm/MHz To reduce potential interference with radio astronomy observations and passive earth sensing satellites, the FCC further limits the radiated emissions by requiring that, in the 23.6–24.0-GHz band, the EIRP of the antenna side lobes beyond 30 above the horizontal plane not exceed 66.3 dBm/MHz until 2010, and dropping to 76.3 dBm/MHz beyond 2014 [12].

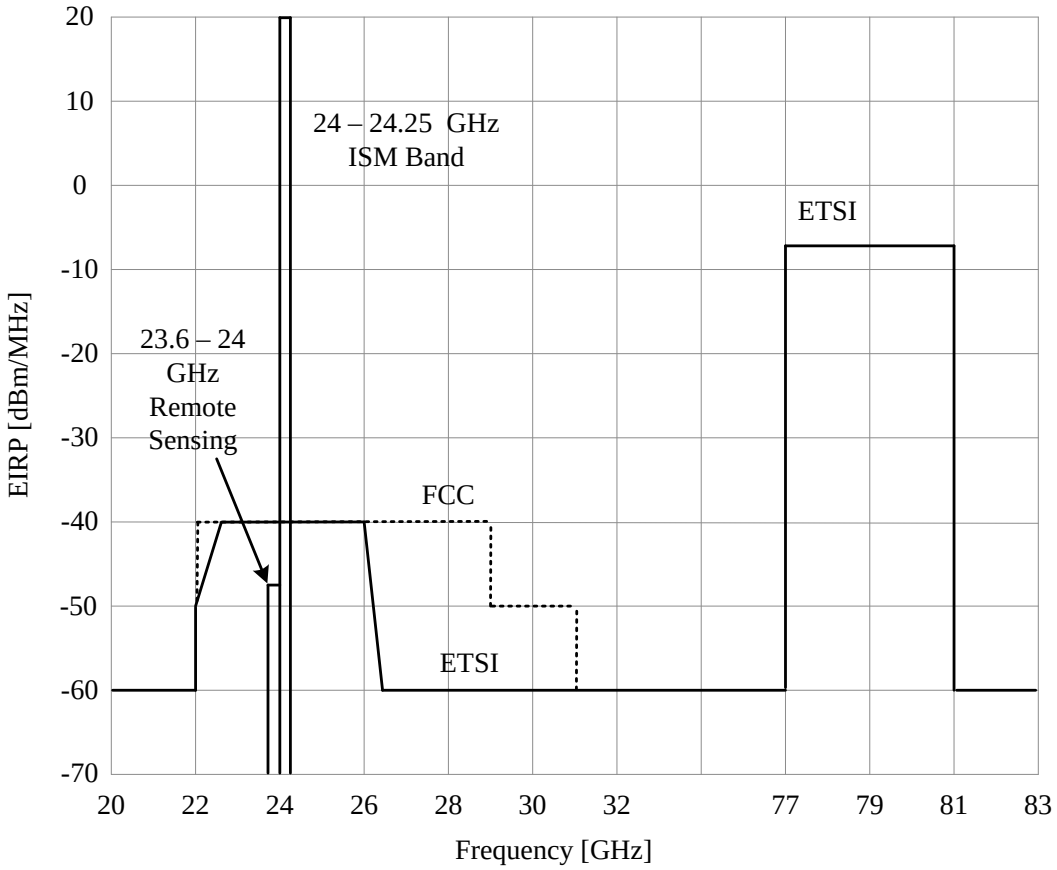

Figure 2.2 Spectral mask of the UWB ruling for vehicular radar.

In addition to the average limit of 41.3dBm/MHz, the FCC also effectively limits the peak EIRP density emission to 17dBm/MHz in a 50-MHz band around the frequency of the highest power emission. These two constraints effectively dictate a maximum duty cycle for a sensor in pulsed operation to around 0.4% to take full advantage of the average power specifications.

2.3 Parameter Specification

In UWB automotive short range radar the K band frequency of 24.125 GHz is used as centre frequency with the System Bandwidth of 500 MHz, Pulse Repetition Interval of 500 ns and Pulse Duration of 2ns.

2.4 Information available for radar echo

UWB Automotive Radar technology is a key enabling technology for innovative driver assistance systems and safety systems. High resolution UWB SRR systems are capable of reliable object tracking, to predict the path of encountering obstacles .This is vital to predict potential car crashes. Although the name radar is derived from radio detection and ranging, radar is capable of providing more information about the target than is implied by its name. Detection of a target signifies the discovery of its presence. It is possible to consider detection independently of the process of information extraction, but it is not often that one is interested in knowing only that a target is present without knowing something about its location and its nature. The extraction of useful target information is therefore an important part of radar operation.

The ability to consider detection independent of information extraction does not mean that there is no relation between the two. The extraction of information generally requires a matched filter, or its equivalent, for optimum processing. The more information that is known about the target a priori, the more efficient will be the detection. For example, if the target location were known, the antenna could be pointed in the proper direction and energy or time need not be wasted searching empty space. Or, if the relative velocity were known, the receiver could be pre tuned to the correct received frequency, negating the need to search the frequency band over which the Doppler shift might occur.

The usual radar provides the location of a target in range and angle. The rate of change of target location can also be measured from the change in range and angle with time, from which the track can be established. In many radar applications detection is not said to occur until its track has been established.

Radar with sufficient resolution in one or more coordinates can determine a target's size and shape. Polarization allows a measure of the symmetry of a target. In principle, radar can also measure the surface roughness of a target and determine something about its dielectric properties.

2.5 Range

The ability to determine range by measuring the time for the radar signal to propagate to the target and back is probably the distinguishing and most important characteristic of conventional radar. No other sensor can measure range to the accuracy possible with radar, at such long ranges, and under adverse weather conditions. Radar has demonstrated its ability to measure interplanetary distances to an accuracy limited only by the accuracy to which the velocity of propagation is known. At more modest distances, the measurement of range can be made with a precision of a few centimeters. The usual radar waveform for determining range is the short pulse. The shorter the pulse, the more precise can be the range measurement.

2.6 Radial Velocity

From successive measurements of range the rate of change of range, or radial velocity, can be obtained. The Doppler frequency shift of the echo signal from a moving target also provides a measure of radial velocity. However, the Doppler frequency measurement in many pulse radars is highly ambiguous, thus reducing its utility as a direct measurement of radial velocity. When it can be used, it is often preferred to successive range measurements since it can achieve a more accurate measurement in a shorter time. Any measurement of velocity, whether by the rate of change of range or by the Doppler frequency shift, requires time. The longer the time of observation, the more accurate can be the measurement of velocity. A longer observation time also can increase the signal-to-noise ratio, another factor that results in increased accuracy. Although the Doppler frequency shift is used in some applications to measure radial velocity (as, for example, in such diverse applications as the police speed meter and satellite surveillance radars), it is more widely employed as the basis for sorting moving targets from unwanted stationary clutter echoes, as in MTI, AMTI (airborne MTI), pulse Doppler, and CW radars.

2.7 Size

If the radar has sufficient resolution, it can provide a measurement of the target's extent, or size. Since many targets of interest have dimensions in meters, resolution must be several meters or less. Resolutions of this order can be readily obtained in the range coordinate. With conventional antennas and the usual radar ranges, the angular resolution is considerably poorer than what can be achieved in range. However, target resolution in the

cross-range (angle) dimension can be obtained comparable with that obtained in range by the use of resolution in the Doppler frequency domain. This requires that there be relative motion between the various parts of the target and the radar.

2.8 Shape

The size of a target is seldom of interest in itself, but its shape and its size are important for recognizing one type of target from another. High resolution radar that obtains the profile of a target in both range and cross range provides the size and shape of the target. The shape of an object can also be obtained by tomography, in which a two dimensional image of a three-dimensional object is reconstructed from the measurement of phase and amplitude, at different angles of observation. (The radar might rotate around the fixed object, or the radar can be fixed and the object rotated about its own axis.) Range resolution is not necessary with the coherent tomographic radar method. As mentioned earlier, comparison of the scattered fields for different polarizations provides a measure of target asymmetry. It should be possible to distinguish targets with different aspect ratios (shapes). The complete exploitation of polarization requires the measurement of phase, as well as amplitude of the echo signal at two orthogonal polarizations and a cross-polarization component. Such measurements (which define the polarization matrix) should allow in principle the recognition of one class of target from another, but in practice it is not easy to do.

One characteristic of target shape is its surface roughness. This measurement can be of particular interest for echoes from the ground and the sea. Rough targets scatter the incident electromagnetic energy diffusely, smooth targets scatter specularly. By observing the nature of the backscatter as a function of the incident angle it should be possible to determine whether a surface is smooth or rough. Surface roughness is a relative measure and depends on the wavelength of the illuminating signal. A surface that appears rough at one wavelength might appear smooth when illuminated with longer-wavelength radiation. Thus another method for determining surface roughness is by varying the frequency of the illuminating radiation and observing the transition from specular to diffuse scatter. A direct method for determining roughness is to observe the scatter from the object with a resolution that can resolve the roughness scale.

3. Weibull Clutter Generation Method

3.1 Introduction

Clutter is the term used by radar engineers to denote unwanted echoes from natural environment. Clutter is generally distributed in spatial extent in that it is much larger in physical size than the radar resolution cell. The radar system has been identified as a significant technology for the improvement of road safety. High range-resolution radar using Ultra wideband (UWB) radio offers many applications to vehicle such as pre-crush warning system stop and go operation, spot assist and lane change assist. Apart from the ability to resolve closely spaced targets in range, it is possible to detect a target more accurately by high resolution range profile because the radar resolution is smaller than the vehicle size. In order to suppress the clutter, a pulse integration and Constant False Alarm Rate (CFAR) has been employed. It is therefore important to investigate the more appropriate clutter model to resemble the clutters in automobile applications. In high resolution radars, the log normal and weibull clutters are proved to be better suited for clutter model in automobile applications. The Weibull clutter model has received much attention in recent years**.** This is due to the fact that it represents the clutter amplitude more accurately in modern radar systems, such as high-resolution radars. The purpose of this section is to develop a generation scheme for Weibull clutter samples with a specified complex Autocorrelation Function (ACF). The simulation scheme can be used for UWB radar system performance analysis and evaluation [23]-[24].

3.2 Coherent Weibull Clutter Model

In this section, we present the coherent correlated weibull sequence generation model. They consist of two blocks as shown in Fig. 3.1; the first block is correlator filter, which is used to generate coherent correlated Gaussian sequence by using the covariance matrix and a zero mean and unit variance coherent white Gaussian sequence. The covariance matrix depends on power, the correlation coefficient of the coherent weibull sequence and its Doppler frequency. The correlated weibull sequence is obtained by feeding correlated Gaussian sequence to a zero-mean nonlinear transformation block (ZMNL). The initial step to achieve our objective is to generate a coherent white Gaussian noise which can be represented as follows

$$z[k] = x_1[k] + jy_1[k] \tag{3.1}$$

where *k* denotes the k-*th* instance of the sequence and the x_1 and y_1 are real valued Gaussian sequences with zero mean and unit variance [27].

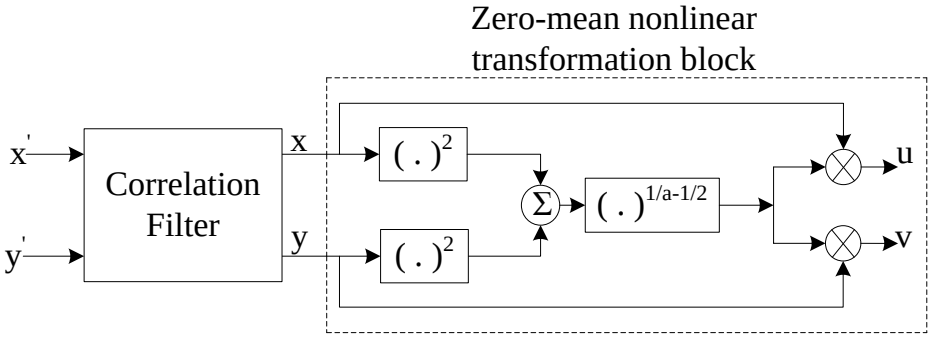

Figure 3.1 Coherent weibull generator model.

In order to transform the coherent white Gaussian sequence present at the input of the correlation filter to correlated Gaussian sequence, the filter makes a transformation of the input sequence as follows

$$x[k] = -\sum_{n=1}^{p} a_n * x[k-n] + z[k] \tag{3.2}$$

where a_n is the filter coefficients obtained by solving the Yule walker equation as shown below using Levinson algorithm

$$\begin{bmatrix} R_c(0) & R_c(-1) & \cdots & R_c(-p) \\ R_c(1) & R_c(0) & & R_c(-(p-1)) \\ \vdots & \vdots & \vdots & \vdots \\ R_c(p) & R_c(p-1) & \cdots & R_c(0) \end{bmatrix} \begin{bmatrix} 1 \\ a_1 \\ \vdots \\ a_p \end{bmatrix} = \begin{bmatrix} \sigma_p^2 \\ 0 \\ \vdots \\ 0 \end{bmatrix} \tag{3.3}$$

$R_c(p)$ is the correlation coefficient between two consecutive samples, which can be expressed as follows

$$R_c(k) = r_{xx}(k) - j r_{xy}(k) \tag{3.4}$$

The relation between the correlation coefficient of coherent correlated weibull clutter ($r_{uu}(k)$, $r_{uv}(k)$) and coherent correlated Gaussian ($r_{xx}(k)$, $r_{xy}(k)$)sequence is expressed as follows

$$r_{uu}(k) = \frac{r_{xx}(k) \cdot a}{2\Gamma\left(\frac{2}{a}\right)} [1 - r_{xx}^2(k) - r_{xy}^2(k)]^{\left(\frac{2}{a}+1\right)} \Gamma^2\left(\frac{1}{a}+\frac{3}{2}\right) F\left(\frac{1}{a}+\frac{3}{2}, \frac{1}{a}+\frac{3}{2}, 2, r_{xx}^2(k) + r_{xy}^2(k)\right) \tag{3.5}$$

$$r_{uv}(k) = \frac{r_{xy}(k)\cdot a}{2\Gamma\left(\frac{2}{a}\right)}[1 - r_{xx}^2(k) - r_{xy}^2(k)]^{\left(\frac{2}{a}+1\right)}\Gamma^2\left(\frac{1}{a}+\frac{3}{2}\right)F\left(\frac{1}{a}+\frac{3}{2},\frac{1}{a}+\frac{3}{2},2,r_{xx}^2(k)+r_{xy}^2(k)\right) \quad (3.6)$$

where $\Gamma()$ is the gamma function and $F()$ is the Gauss hyper geometric function, a is the shape parameter (i.e., skewness parameter) of the weibull sequence. As a check when a = 2, the weibull process becomes Gaussian, the correlation coefficients $r_{uu}(k)$ is same to $r_{xx}(k)$. Fig. 3.2-3.3 shows the covariance mapping between $r_{uu}(k)$ and $r_{xx}(k)$ for a = 0.5,1.5, 1.0 and 2.0 [32]. Finally, we implement correlation filter with specified $R_c(p)$, and the method to obtain the filter coefficients (a_n) by using levinson algorithm is presented as follows.

3.3 Yule-Walker equation

It is well known that any regular stationary random process can be represented as the output of a linear shift-invariant filter driven by white noise. One common method for modeling random signals is to represent them as the output of an **all-pole** linear filter driven by white noise. Although this may not be the most efficient representation of the random process (in terms of the number of parameters required) it nevertheless leads to a simple modeling procedure. Since the power spectrum of the filter output is given by the constant noise spectrum (σ_w^2) multiplied by the squared magnitude of the filter, random signals with desired spectral characteristics can be produced by choosing a filter with an appropriate denominator polynomial.

The linear prediction problem leads to a method for performing this modeling. Recall that the prediction error filter that produces $\varepsilon[n]$ from $x[n]$ is an FIR filter whose output is given by

$$\varepsilon[n] = x[n] + a_1^* x[n-1] + a_1^* x[n-1] + a_1^* x[n-1] + \cdots + a_p^* x[n-P] \quad (3.7)$$

This filter depicted has a transfer function given by

$$A(z) = 1 + a_1^* z^{-1} + a_2^* z^{-2} + \cdots + a_p^* z^{-P} \quad (3.8)$$

Further recall that if the prediction order P of the filter is sufficiently large, then the output is approximately a white noise process with variance σ_ε^2.

Suppose now this procedure is turned around. That is, the filter is inverted and driven with a white noise sequence of variance $\sigma_w^2 = \sigma_\varepsilon^2$ as shown in Fig. 3. This system will then produce a random sequence with the same statistical characteristics as those of the original sequence $x[n]$. Thus it represents a model for the process $x[n]$. Let us thus consider a system of the form

$$x[n] = -a_1 x[n-1] - a_2 x[n-2] - \cdots - -a_p x[n-P] + w[n] \tag{3.9}$$

The above equation (3.10) is equivalent to (3.8) except the coefficients a_i* have been replaced by the coefficients a_i and $\varepsilon[n]$ has been replaced by $w[n]$. The equation has also been rewritten in recursive form. As such, it is in the form of a statistical regression, where the "dependent" variable $x[n]$ is represented as a linear combination of "independent" variables $x[n\text{-}1]$ through $x[n\text{-}P]$. Since both independent and dependent variables belong to the same random process, $x[n]$ is called and autoregressive or AR process; the process is seen to be "regressed upon itself". The filter in the AR model is an IIR filter with transfer function

$$H(z) = \frac{1}{A(z)}$$

Where

$$A(z) = 1 + a_1 z^{-1} + a_2 z^{-2} + \cdots + a_p z^{-P}$$

Since $A(z)$ involves only negative powers of z, the filter has a P^{th} -order zero at the origin but otherwise has only poles. The AR model is therefore said to be an "all-pole" model. Moreover, it is later shown that as long as the denominator coefficients a_i are found by solving normal equations with a positive definite correlation function; the poles all lie with the unit circle. Since $H(z)$ corresponds to a casual filter, this implies that it is minimum-phase (i.e., it is a casual stable filter with a casual stable inverse). Direct form realizations for the prediction error filter and the corresponding AR model filter are shown in Fig. 8.2 of [30].

Since the AR model is obtained by inverting the prediction error filter, it should be possible to show directly that the parameters a_1, a_2,..., a_P and σ_w^2 of any AR model can be found by solving normal equations. This can be done as follows. Begin with a postulated model for a random process of the form (3.10) and write this as

$$x[n] + a_1 x[n-1] + a_2 x[n-2] + \cdots + a_p x[n-P] = w[n] \tag{3.10}$$

Then it follows from the results of linear shift invariant system, that the correlation function satisfies the difference equation

$$R_x[l] + a_1 R_x[l-1] + a_2 R_x[l-2] + \cdots + a_p R_x[l-P] = R_{wx}[l] \tag{3.11}$$

Now further recall that if $h[n]$ is the impulse response of (3.11), the R_{xw} is given by

$$R_{xw}[l] = h[l] * R_w[l] = h[l] * \sigma_w^2 \delta[l] = \sigma_w^2 h[l] \tag{3.12}$$

so

$$R_{wx}[l] = \sigma_w^2 h^*[-l] \tag{3.13}$$

Substituting (3.13) in to (3.11) produces

$$R_x[l] = a_1 R_x[l-1] + \cdots + a_P R_x[l-P] = \sigma_w^2 h^*[-l] \tag{3.14}$$

Since $h[n]$ is the impulse response of a casual filter, $h[n]$ is equal to 0 for $n < 0$, and from the Initial Value Theorem

$$h[0] = \lim_{z\to\infty} H(z) = \lim_{z\to\infty} \frac{1}{1 + a_1 z^{-1} + \cdots + a_P z^{-P}} = 1 \tag{3.15}$$

With these considerations (3.14) can be evaluated for $l = 1, 2, 3, \ldots, P$. For $l = 0$ the right side of (3.14) will be equal to σ_w^2, while for $l>0$ the right side will be equal to 0. If this set of equations is written in matrix form the result is

$$\begin{bmatrix} R_x[0] & R_x[-1] & \cdots & R_x[-P] \\ R_x[1] & R_x[0] & \cdots & R_x[-P+1] \\ \vdots & & \vdots & \vdots \\ R_x[P] & R_x[P-1] & \cdots & R_x[0] \end{bmatrix} \begin{bmatrix} 1 \\ a_1 \\ \vdots \\ a_P \end{bmatrix} = \begin{bmatrix} \sigma_w^2 \\ 0 \\ \vdots \\ 0 \end{bmatrix} \tag{3.16}$$

We refer to the above equation (3.16) for the AR model as the Yule-Walker equation.

3.4 Levinson Algorithm

The Levinson recursion provides a fast method of solving the Normal equations by beginning with a filter of order 0 and recursively generating filters of order 1, 2, 3 and so on, up to the desired order P. At each stage the filter parameters of order p are computed by simple and elegant operations on the filter parameters of order $p-1$. The total computational effort grows as P^2 and thus the method is more computationally efficient than solving the Normal equations by matrix inversion, where the computational effort grows as P^3.

The Levinson recursion can be derived by considering the Normal equations of order p, which are written as

$$\tilde{\mathrm{R}}_x^{(p)} \mathrm{a}_p = \begin{bmatrix} \sigma_p^2 \\ 0 \\ \vdots \\ 0 \end{bmatrix} \tag{3.17}$$

where

$$\tilde{\mathrm{R}}_x^{(p)} = \begin{bmatrix} R_x[0] & R_x[1] & \cdots & R_x[P] \\ R_x[-1] & R_x[0] & \cdots & R_x[P-1] \\ \vdots & \vdots & \vdots & \vdots \\ R_x[-P] & R_x[-P+1] & \cdots & R_x[0] \end{bmatrix} \tag{3.18}$$

and

$$\mathrm{a}_p = \begin{bmatrix} 1 \\ a_1^{(P)} \\ \vdots \\ a_p^{(p)} \end{bmatrix} \tag{3.19}$$

The backward Normal equations of order p likewise have the form

$$\mathrm{R}_x^{(p)}\mathrm{b}_p = \begin{bmatrix} \sigma_p'^2 \\ 0 \\ \vdots \\ 0 \end{bmatrix} \tag{3.20}$$

where

$$\mathrm{R}_x^{(p)} = \begin{bmatrix} R_x[0] & R_x[1] & \cdots & R_x[-P] \\ R_x[1] & R_x[0] & \cdots & R_x[1-p] \\ \vdots & \vdots & \vdots & \vdots \\ R_x[P] & R_x[P-1] & \cdots & R_x[0] \end{bmatrix} \tag{3.21}$$

and

$$\mathrm{b}_p = \begin{bmatrix} 1 \\ b_1^{(P)} \\ \vdots \\ b_p^{(p)} \end{bmatrix} \tag{3.22}$$

now consider equation (3.19) the term $\boldsymbol{r}_p$ can be defined as

$$\mathrm{r}_p = \begin{bmatrix} R_x[1] \\ R_x[2] \\ \vdots \\ R_x[p+1] \end{bmatrix} \tag{3.23}$$

then the reversed correlation matrix of order p can be partitioned as

$$\tilde{\tilde{\mathrm{R}}}_x^{(p)} = \begin{bmatrix} \tilde{\tilde{\mathrm{R}}}_x^{(p-1)} & | & \tilde{\mathrm{r}}_{p-1} \\ ---- & -|- & -- \\ \tilde{\mathrm{r}}_{p-1}^{*T} & | & R_x[0] \end{bmatrix} \tag{3.24}$$

now assume that the linear prediction parameters of order *p-1* are known. These satisfy (3.18) with *p* replaced by *p-1*. Then consider an augmented set of normal equations for the forward problem of the form

$$\tilde{\tilde{\mathrm{R}}}_x^{(p)} \begin{bmatrix} \mathrm{a}_{p-1} \\ -- \\ 0 \end{bmatrix} = \begin{bmatrix} \tilde{\tilde{\mathrm{R}}}_x^{(p-1)} & | & \tilde{\mathrm{r}}_{p-1} \\ ---- & -|- & -- \\ \tilde{\mathrm{r}}_{p-1}^{*T} & | & R_x[0] \end{bmatrix} \begin{bmatrix} \mathrm{a}_{p-1} \\ -- \\ 0 \end{bmatrix} = \begin{bmatrix} \sigma_{p-1}^2 \\ 0 \\ \vdots \\ \Delta_p \end{bmatrix} \tag{3.25}$$

where the term Δ_p is seen to be

$$\Delta_p = \tilde{\mathrm{r}}_{p-1}^{*T} \tilde{\mathrm{a}}_{p-1} = \mathrm{r}_{p-1}^{*T} \tilde{\mathrm{a}}_{p-1} \tag{3.26}$$

also consider a corresponding set of Normal equations for the backward problem

$$\mathrm{R}_x^{(p)} \begin{bmatrix} \mathrm{b}_{p-1} \\ -- \\ 0 \end{bmatrix} = \begin{bmatrix} \mathrm{R}_x^{(p-1)} & | & \tilde{\mathrm{r}}_{p-1}^{*} \\ ---- & -|- & -- \\ \tilde{\mathrm{r}}_{p-1}^{T} & | & R_x[0] \end{bmatrix} \begin{bmatrix} \mathrm{b}_{p-1} \\ -- \\ 0 \end{bmatrix} = \begin{bmatrix} \sigma_{p-1}'^2 \\ 0 \\ \vdots \\ \Delta_p' \end{bmatrix} \tag{3.27}$$

where the term Δ_p' is seen to be

$$\Delta_p' = \tilde{\mathrm{r}}_{p-1}^{T} \mathrm{b}_{p-1} = \mathrm{r}_{p-1}^{T} \tilde{\mathrm{b}}_{p-1} \tag{3.28}$$

Suppose that all the terms of (3.28) are reversed. The result is as follows

$$\tilde{\tilde{\mathrm{R}}}_x^{(p)} \begin{bmatrix} 0 \\ -- \\ \tilde{\mathrm{b}}_{p-1} \end{bmatrix} = \begin{bmatrix} \Delta_p \\ 0 \\ \vdots \\ \sigma_{p-1}^2 \end{bmatrix} \tag{3.29}$$

If this equation is multiplied by a constant c_1 and added to (3.27), the combined result is

$$\tilde{\tilde{\mathrm{R}}}_x^{(p)} \left(\begin{bmatrix} \mathrm{a}_{p-1} \\ -- \\ 0 \end{bmatrix} + c_1 \begin{bmatrix} 0 \\ -- \\ \tilde{\mathrm{b}}_{p-1} \end{bmatrix} \right) = \begin{bmatrix} \sigma_{p-1}'^2 \\ 0 \\ \vdots \\ \Delta_p' \end{bmatrix} + c_1 \begin{bmatrix} \Delta_p' \\ 0 \\ \vdots \\ \sigma_{p-1}'^2 \end{bmatrix} \tag{3.30}$$

Now compare this result with (3.17), the Normal equations of order p. Since the solution to (3.17) is unique, if c_1 is chosen so that

$$\begin{bmatrix} \sigma'^2_{p-1} \\ 0 \\ \vdots \\ \Delta'_p \end{bmatrix} + c_1 \begin{bmatrix} \Delta'_p \\ 0 \\ \vdots \\ \sigma'^2_{p-1} \end{bmatrix} = \begin{bmatrix} \sigma^2_p \\ 0 \\ \vdots \\ 0 \end{bmatrix} \tag{3.31}$$

Then it must follow that

$$\begin{bmatrix} a_{p-1} \\ -- \\ 0 \end{bmatrix} + c_1 \begin{bmatrix} 0 \\ -- \\ \tilde{\mathrm{b}}_{p-1} \end{bmatrix} = \mathrm{a}_p \tag{3.32}$$

Equation (3.31) requires that

$$\sigma^2_{p-1} + c_1 \Delta'_p = \sigma^2_p \tag{3.33}$$

$$\Delta_p + c_1 \sigma'^2_{p-1} = 0 \tag{3.34}$$

All of these relations turn out to be necessary in the recursion. Now let us repeat this procedure for the backward system of equations. First reverse all of the terms in (3.25) to obtain

$$\mathrm{R}_x^{(p)} \begin{bmatrix} 0 \\ -- \\ \tilde{\mathrm{a}}_{p-1} \end{bmatrix} = \begin{bmatrix} \Delta_p \\ 0 \\ \vdots \\ \sigma^2_{p-1} \end{bmatrix} \tag{3.35}$$

Then multiply this equation by a constant c_2 and add it to (3.27)

$$\mathrm{R}_x^{(p)} \left[\begin{bmatrix} \mathrm{b}_{p-1} \\ -- \\ 0 \end{bmatrix} + c_2 \begin{bmatrix} 0 \\ -- \\ \tilde{\mathrm{a}}_{p-1} \end{bmatrix} \right] = \begin{bmatrix} \sigma'^2_{p-1} \\ 0 \\ \vdots \\ \Delta'_p \end{bmatrix} + c_2 \begin{bmatrix} \Delta_p \\ -- \\ \sigma^2_{p-1} \end{bmatrix} \tag{3.36}$$

Finally, compare this to the backward Normal equations (3.20), we get

$$\sigma'^2_{p-1} + c_1 \Delta_p = \sigma'^2_p \tag{3.37}$$

$$\Delta'_p + c_1 \sigma^2_{p-1} = 0 \tag{3.38}$$

Then it follows that

$$\begin{bmatrix} \mathrm{b}_{p-1} \\ -- \\ 0 \end{bmatrix} + c_2 \begin{bmatrix} 0 \\ -- \\ \tilde{\mathrm{a}}_{p-1} \end{bmatrix} = \mathrm{b}_p \tag{3.39}$$

The equations (3.26), (3.28), (3.32), (3.33), (3.37) and (3.39) form the main part of the recursion. To complete the procedure, the needed constants c_1 and c_2 can be found from (3.35)

$$c_1 = -\frac{\Delta_p}{\sigma'^2_{p-1}} \tag{3.40}$$

$$c_2 = -\frac{\Delta'_p}{\sigma^2_{p-1}} \tag{3.41}$$

This completes the process. Since c_1, c_2, Δ_p and Δ'_p are defined in terms of the correlation function and the parameters of order p-1, these quantities can be computed immediately. Once these are determined, the backward and forward filter parameters and the prediction error variances can be computed from (3.32), (3.33), (3.37) and (3.39). The parameters $-c_1 = \gamma_p$ and $-c_2 = \gamma'_p$ are known as the forward and backward reflection coefficients. The recursion is initialized with

$r_0 = R_x[1]$, $a_0 = 1$, $\sigma_0^2 = R_x[0]$

An alternative formula for step IV is given in the table. This is easily obtained by solving (3.38) for Δ'_p and substituting the results in (3.33) as follows

$$\sigma_p^2 = (1 - c_1 c_2)\sigma_{p-1}^2 = (1 - \gamma_p \gamma'_p)\sigma_{p-1}^2 \tag{3.42}$$

Similarly solving (3.34) for Δ_p and substituting in (3.37) yields

$$\sigma'^2_p = (1 - c_2 c_1)\sigma'^2_{p-1} = (1 - \gamma'_p \gamma_p)\sigma'^2_{p-1} \tag{3.43}$$

Table 3.1 Levinson recursion, role of the forward and backward variables.

Initialization: $r_0 = R_x[1]$, $a_0 = 1$, $\sigma_0^2 = R_x[0]$		
I	$\Delta_p = \mathrm{r}_{p-1}^{*T}\,\tilde{\mathrm{a}}_{p-1}$	$\Delta'_p = \mathrm{r}_{p-1}^{T}\,\tilde{\mathrm{b}}_{p-1}$
II	$\gamma_p = \dfrac{\Delta_p}{\sigma'^2_{p-1}}$	$\gamma'_p = \dfrac{\Delta'_p}{\sigma^2_{p-1}}$
III	$\mathrm{a}_p = \begin{bmatrix} \mathrm{a}_{p-1} \\ -- \\ 0 \end{bmatrix} - \gamma_p \begin{bmatrix} 0 \\ -- \\ \tilde{\mathrm{b}}_{p-1} \end{bmatrix}$	$\mathrm{b}_p = \begin{bmatrix} \mathrm{b}_{p-1} \\ -- \\ 0 \end{bmatrix} - \gamma_p \begin{bmatrix} 0 \\ -- \\ \tilde{\mathrm{a}}_{p-1} \end{bmatrix}$
IV	$\sigma_p^2 = (1-\gamma_p\gamma'_p)\sigma_{p-1}^2$	$\sigma'^2_p = (1-\gamma_p\gamma'_p)\sigma'^2_{p-1}$

Although the equations of table I clearly show the interaction between the forward and the backward models. Specifically we know that

$\mathrm{b}_{p-1} = \mathrm{a}^*_{p-1}$ and $\sigma'^2_{p-1} = \sigma^2_{p-1}$

Therefore, it follows from the first step in table 3.1 as

$$\Delta'_p = \mathrm{r}_{p-1}^{T}\,\tilde{\mathrm{b}}_{p-1} = \mathrm{r}_{p-1}^{T}\,\tilde{\mathrm{a}}^*_{p-1} \tag{3.44}$$

And application of this result to the second step in the table produces

$$\gamma'_p = \frac{\Delta'_p}{\sigma^2_{p-1}} = \frac{\Delta^*_p}{\sigma'^2_{p-1}} = \gamma^*_p \tag{3.45}$$

By using these additional relations and combining steps I and II, the equations in table I can be written as a single thread recursion, which is all that is necessary for the purposes of computation. The equations are

$\Delta_p = \mathrm{r}_{p-1}^{*T}\,\tilde{\mathrm{a}}_{p-1}$

the constant γ_p is called the reflection coefficient which is determined as follows at every increment of p

$$\gamma_p = \frac{\Delta_p}{\sigma^2_{p-1}}$$

$$\mathrm{a}_\mathrm{p} = \begin{bmatrix} \mathrm{a}_{p-1} \\ -- \\ 0 \end{bmatrix} - \gamma_p \begin{bmatrix} 0 \\ -- \\ \tilde{\mathrm{a}}^*_{p-1} \end{bmatrix}$$

$$\sigma^2_p = (1 - |\gamma_p|^2)\sigma^2_{p-1}$$

Which are applied for $p = 1, 2, \ldots, P$ with initial conditions

$r_0 = R_x[1]$, $a_0 = 1$, $\sigma_0^2 = R_x[0]$

Example

Consider the first three values of correlation function as

$R[0] = 3$, $R[1] = R[-1] = 2$, $R[2] = R[-2] = 1$

Therefore the normal Yule walker equation can be represented as

$$\begin{bmatrix} 3 & 2 & 1 \\ 2 & 3 & 2 \\ 1 & 2 & 3 \end{bmatrix} \begin{bmatrix} 1 \\ a_1 \\ a_2 \end{bmatrix} = \begin{bmatrix} \sigma_2^2 \\ 0 \\ 0 \end{bmatrix}$$

By applying levinson algorithm to the above equation

$r_0 = R[1] = 2$, $a_0 = 1$, and $\sigma_0^2 = R[0] = 3$

$$\gamma_1 = \frac{r_0 a_0}{\sigma_0^2} = \frac{2 \times 1}{3} = \frac{2}{3}$$

$$a_1 = \begin{bmatrix} a_0 \\ -- \\ 0 \end{bmatrix} - \gamma_1 \begin{bmatrix} 0 \\ -- \\ \tilde{a}_0 \end{bmatrix} = \begin{bmatrix} 1 \\ 0 \end{bmatrix} - \frac{2}{3}\begin{bmatrix} 0 \\ 1 \end{bmatrix} = \begin{bmatrix} 1 \\ -2/3 \end{bmatrix}$$

$$\sigma_1^2 = (1-|\gamma_1|^2)\sigma_0^2 = (1-(2/3)^2)\cdot 3 = 5/3$$

$$\gamma_2 = \frac{r_1^{*T}\tilde{a}_1}{\sigma_1^2} = \frac{1}{5/3}\begin{bmatrix}2 & 1\end{bmatrix}\begin{bmatrix}-2/3\\ 1\end{bmatrix} = -1/5 = -0.2$$

$$a_2 = \begin{bmatrix}a_1\\ --\\ 0\end{bmatrix} - \gamma_2\begin{bmatrix}0\\ --\\ \tilde{a}_1\end{bmatrix} = \begin{bmatrix}1\\ -2/3\\ 0\end{bmatrix} - (-1/5)\begin{bmatrix}0\\ -2/3\\ 1\end{bmatrix} = \begin{bmatrix}1\\ -0.8\\ 0.2\end{bmatrix}$$

$$\sigma_2^2 = (1-|\gamma_{21}|^2)\sigma_1^2 = (1-(-1/5)^2)\cdot(5/3) = 1.6$$

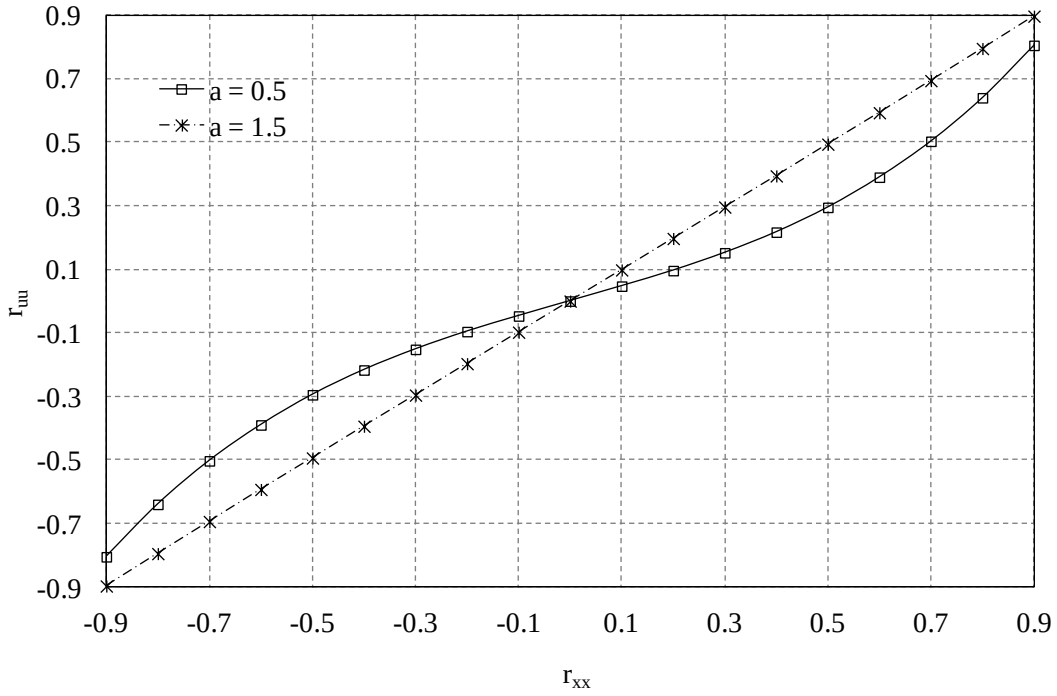

Figure 3.2 Covariance mapping between r_{uu} and r_{xx} for a = 0.5 and 1.5.

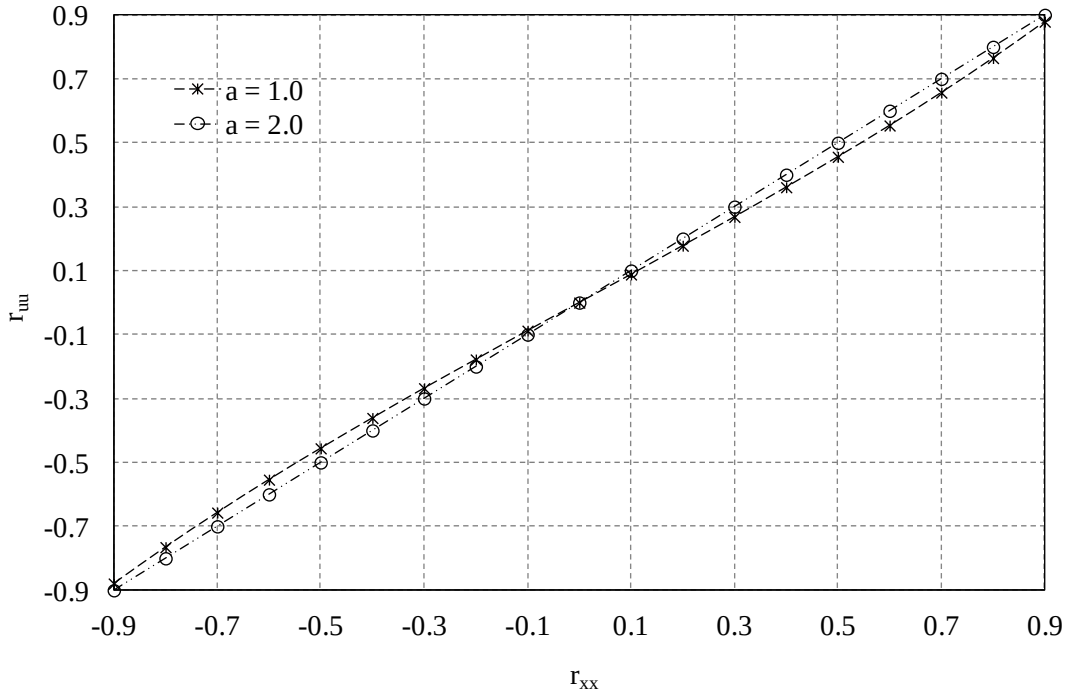

Figure 3.3 Covariance mapping between r_{uu} and r_{xx} for a = 1.0 and 2.0.

Table 3.2 r_{xx} and r_{uu} for various skewness values (a).

a = 0.5		**a = 1**		**a = 1.5**		**a = 2**	
$\mathbf{r_{xx}}$	$\mathbf{r_{uu}}$	$\mathbf{r_{xx}}$	$\mathbf{r_{uu}}$	$\mathbf{r_{xx}}$	$\mathbf{r_{uu}}$	$\mathbf{r_{xx}}$	$\mathbf{r_{uu}}$
-0.9	-0.805	-0.9	-0.879	-0.9	-0.897	-0.9	-0.9
-0.8	-0.64	-0.8	-0.765	-0.8	-0.795	-0.8	-0.8
-0.7	-0.503	-0.7	-0.657	-0.7	-0.694	-0.7	-0.7
-0.6	-0.39	-0.6	-0.554	-0.6	-0.593	-0.6	-0.6
-0.5	-0.295	-0.5	-0.456	-0.5	-0.494	-0.5	-0.5
-0.4	-0.217	-0.4	-0.361	-0.4	-0.394	-0.4	-0.4
-0.3	-0.152	-0.3	-0.268	-0.3	-0.296	-0.3	-0.3
-0.2	-0.096	-0.2	-0.178	-0.2	-0.197	-0.2	-0.2
-0.1	-0.047	-0.1	-0.088	-0.1	-0.098	-0.1	-0.1
0	0	0	0	0	0	0	0
0.1	0.047	0.1	0.088	0.1	0.098	0.1	0.1
0.2	0.096	0.2	0.178	0.2	0.197	0.2	0.2
0.3	0.152	0.3	0.268	0.3	0.296	0.3	0.3
0.4	0.217	0.4	0.361	0.4	0.394	0.4	0.4
0.5	0.295	0.5	0.456	0.5	0.494	0.5	0.5
0.6	0.39	0.6	0.554	0.6	0.593	0.6	0.6
0.7	0.503	0.7	0.657	0.7	0.694	0.7	0.7
0.8	0.64	0.8	0.765	0.8	0.795	0.8	0.8
0.9	0.805	0.9	0.879	0.9	0.897	0.9	0.9

Algorithm for Coherent Weibull Clutter Simulator

STEP 1: Declare the required arrays dynamically and generate Gaussian noise with zero mean and unit variance.

STEP 2: Create the XL file to print the autocorrelation and PDF of the coherent weibull clutter simulator separately.

STEP 3: Determine the coefficients of correlation filter by using Levinson algorithm function. The input for the levinson algorithm function is r_{xx} or r_{xy} obtained by using (3.5), (3.6) and the experimental data r_{uu} or r_{uv} as mentioned in this document.

STEP 4: Implement correlation filter by using the coefficients obtained from levinson algorithm function.

STEP 5: The output of the correlation filter is converted to coherent weibull random variable by using ZMNL function.

STEP 6: The autocorrelation and PDF of the ZMNL function complex output is printed in XL file separately.

STEP 8: end.

3.5 Simulation Result

The purpose of the simulation is to generate coherent weibull clutter model for conventional and proposed detectors. First, we use the experimental result from [23] and obtain the covariance mapping values for various r_{uu} and r_{xx} as mentioned in table 3.2 above. And then the probability density function is obtained at the output of the coherent weibull clutter model. A large enough number of trials are used to obtain each point of the probability density functions. The number of trials is about 1000000 times.

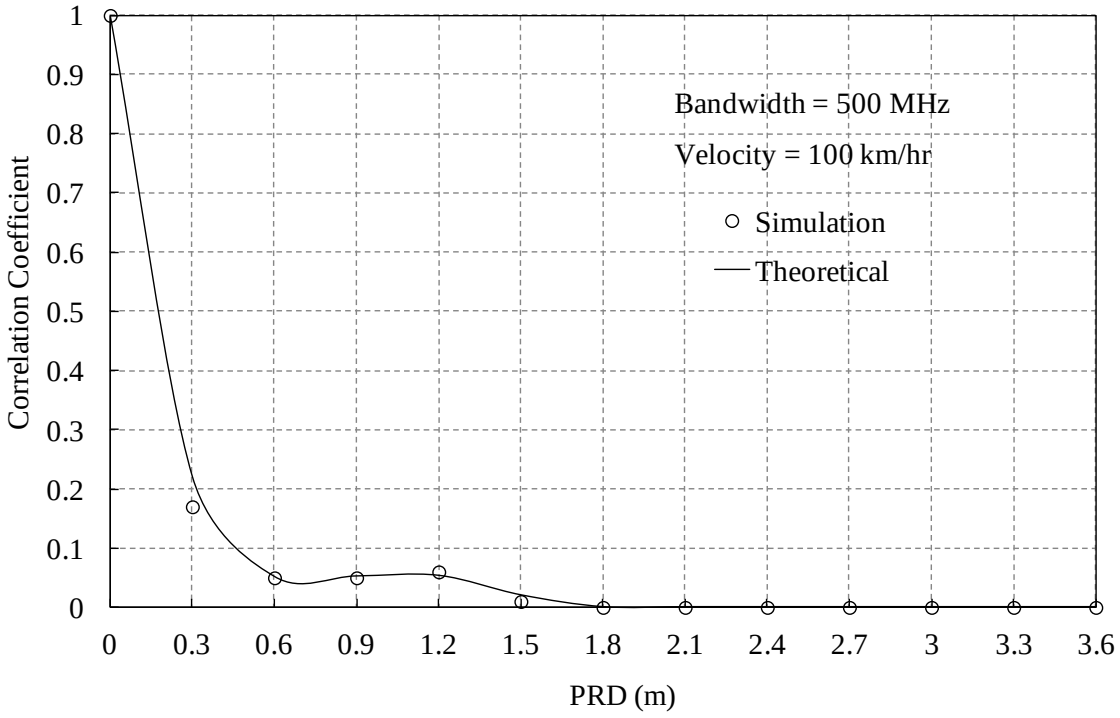

Figure 3.4 Correlation coefficient as a function of pulse repetition distance.

3.5.1 Correlation Co-efficients

In this section, we present the computer simulation results for weibull clutter model by using the experimental result from [23]. The cross-correlation coefficient of the clutter as a function of pulse repetition distance (PRD) for velocity of 100 km/h is presented in Fig. 3.4. From the Fig. 3.4 we can observe that the experimental cross-correlation coefficient and the simulation result are found to be in good agreement. Thus, the clutter model developed in this thesis resembles to the actual clutter environment and the same can be used to analyze the detection performance of UWB SRR system efficiently in automobile application.

3.5.2 Probability Density Function

The probability density function obtained at the output of the coherent weibull clutter model is presented in Fig. 3.5. A large enough number of trials are used to obtain each point of the probability density functions. The number of trials is about 1000000 times.

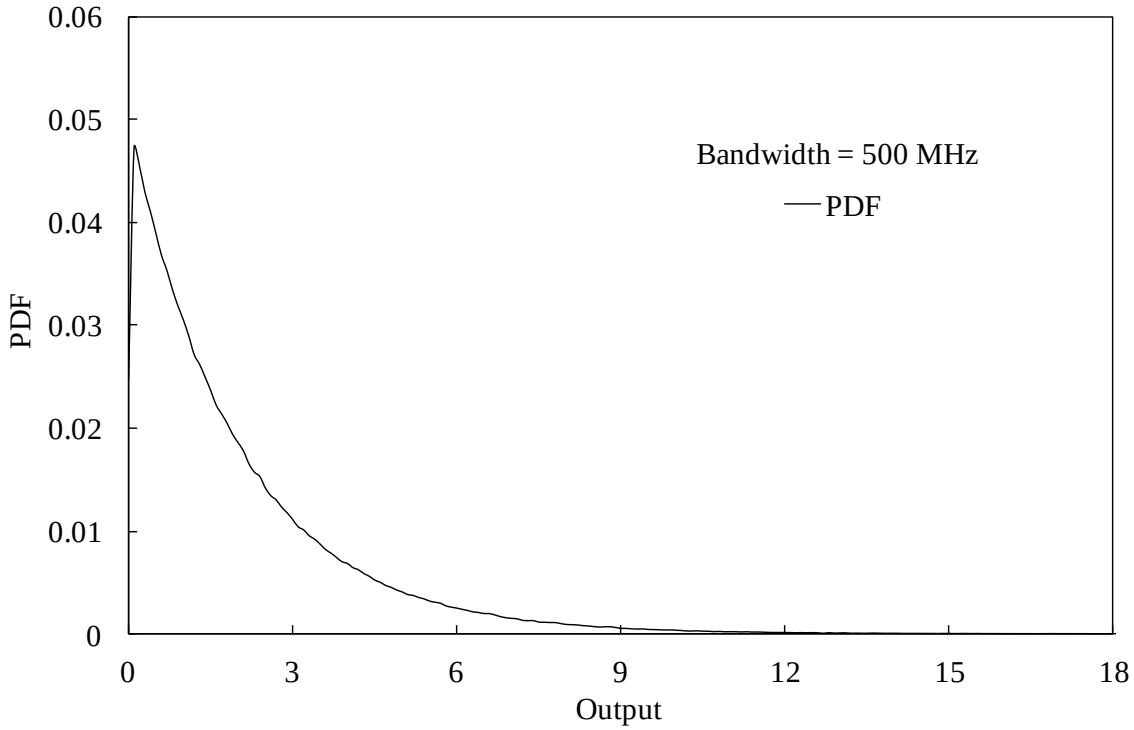

Figure 3.5 PDF at the output of coherent weibull clutter model.

4. Stationary Target

The key idea behind the development of Short Range Radar (SRR) in automotive applications is collision avoidance and reduces traffic fatality. The demand for short range radar sensors which are used for target detection has increased fabulously in automotive sector. The source for target detection and velocity measure is the radar signals reflected by the target and the received radar signal is a mixture of noise and varied signals. The designed system must provide the optimal technique to obtain the desired target detection and velocity, preferred detection can be determined by using specific algorithm for measuring the energy of the received signals in the receiver side [1].

4.1 Conventional Detection Algorithm

Single pulse detection refers to the detection of either single RF pulses or a single coherent pulse train made up of a series of coherent RF pulses. The problem of single pulse detection is to take known information about a reflected single pulse signal $s(t)$, to observe a received signal $v(t)$ over some observation interval in some resolution cell, and to determine from the observation of $v(t)$ whether a signal of the form $s(t)$ exists in the resolution cell. Typically, the duration of $s(t)$ is known and set equal to the observation interval τ . Single pulse detection, sometimes called detection subject to pre-detection or coherent integration, is performed on a reflected signal with an exactly known RF structure, except for time of occurrence (range delay), Doppler frequency shift, and angle of arrival, initial RF phase, and amplitude [8].

It can be shown [50] that for the detection of signals of unknown delay, Doppler frequency shift, and angle of arrival, in a white , Gaussian noise environment, the optimum Bayes detection criteria corresponds to a separate likelihood ratio test in each range-angle-Doppler resolution cell. The dimensions of each resolution cell are approximately: the antenna beam width in angle $\Delta\tau$ in range and $1/\tau$ in Doppler frequency, where $\Delta\tau$ and τ are the single (coherent) pulse width (after pulse compression, for the case of phase coded signals) and the signal duration, respectively. Since the same test is performed in each resolution cell, then to determine the optimal Bayes detection strategy it is sufficient to determine the optimal Bayes receiver in a typical range-angle-Doppler cell. For simplicity, the cell chosen (for the purpose of determining a Bayes decision rule) is from an arbitrary bin, in an arbitrary antenna beam, having zero Doppler.

Suppose, then, that the antenna is pointed some arbitrary direction within the search volume, that detection is to be performed for zero Doppler signals, and that the range bin under consideration is defined by

$$RB = \frac{ct}{2} \qquad t_d \le t \le t_d + \Delta\tau \tag{4.1}$$

where t_d is the range delay of the reflected signal, $\Delta\tau$ is the single (coherent) pulse width (after pulse compression, for the case of phase coded signals), and c is the speed of light. Further, suppose t_d is known. Then, range, angle and Doppler are assumed to be known and the detection problem is to develop a Bayes decision rule for the determination of the presence or absence of a reflected signal in the range-angle-Doppler resolution cell under the conditions that detection is performed in an exactly-known, unvarying, white, Gaussian noise environment and the reflected signal amplitude and initial RF phase are unknown.

Since the received signal, initial phase is not known to within a fraction of 2π radians; it is generally assumed to be a uniformly distributed random variable with a uniform density function in the interval $[0,2\pi]$. A uniform probability density function is used because it assumes the least a priori information about initial phase.

When the received-signal amplitude is unknown, a statistical model for amplitude must be assumed. The classical models for target RCS (reflected signal amplitude) fluctuations are the Swerling models. The Swerling models are of two types: non-fluctuating and fluctuating. A Bayes decision rule for the detection of non-fluctuating single-pulse signals with unknown initial RF phase is developed in section 3.4.1.1 of [32]. A Bayes decision rule for the detection of Swerling fluctuating single-pulse signals with unknown initial RF phase will be developed in section 3.4.1.2 of [32].

A reflected radar signal, denoted $s(t)$, is an image of a transmitted radar signal, denoted $s_t(t)$,shifted in time by the transmission delay time (t_d), in frequency by the Doppler frequency shift (taken here to be zero), and in amplitude. A single transmitted pulse, or single coherent pulse train (see Fig. 4.1), can be expressed as

$$s_t(t) = A' a(t) \cos\left[\omega_0 t + \theta(t) + \phi'\right], \qquad 0 \le t \le \tau \tag{4.2}$$

where,

A' is the transmitted signal amplitude

$a(t)$ is the time modulation on A'

ω_0 is a constant carrier frequency

$\theta(t)$ is a phase modulation on ω_0. In order to extend the detection range, each RF pulse may be phase coded upon transmission and subject to pulse compression upon reception.

ϕ' is the initial phase at time t=0, the start of transmission

τ is the waveform duration

functions $a(t)$ and $\theta(t)$ vary slowly in comparison with $\cos(\omega_0 t)$

Then, the reflected radar signal, for zero Doppler, can be written as,

$$s(t) = Aa(t-t_d)\cos[\omega_0(t-t_d)+\theta(t-t_d)+\phi], \qquad t_d \le t \le t_d+\tau \tag{4.3}$$

where,

A is the received signal amplitude

t_d is the target echo delay

ϕ is the initial phase at time $t=t_d$

$\theta(t)$, $a(t)$, τ, and ω_0 are as defined above for the transmitted signal.

As described above, for the purpose of determining optimum Bayes detection criteria, t_d is assumed to be known. Then, without loss of generality, t_d can be set equal to zero. This amounts to a shift in the time axis, so that time t=0 begins when the reflected signal reaches the receiving antenna. Then, $s(t)$ can be expressed as

$$s(t) = Aa(t)\cos[\omega_0 t+\theta(t)+\phi], \qquad 0 \le t \le \tau \tag{4.4}$$

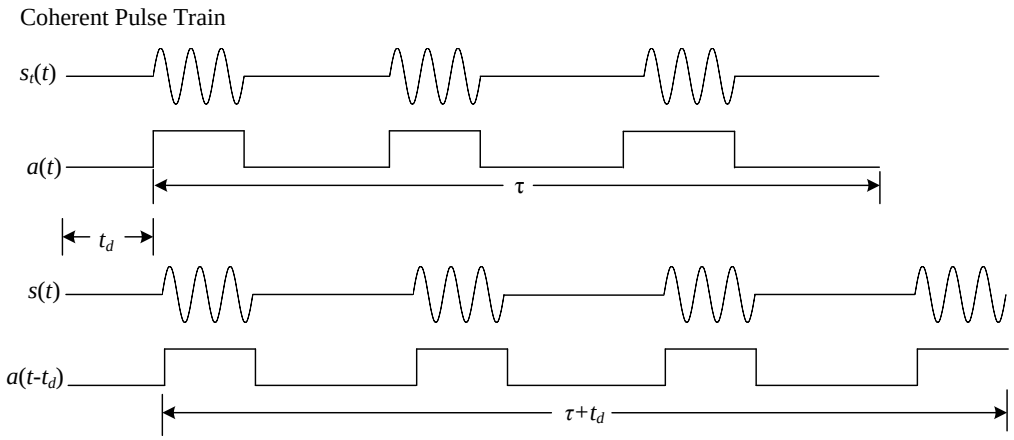

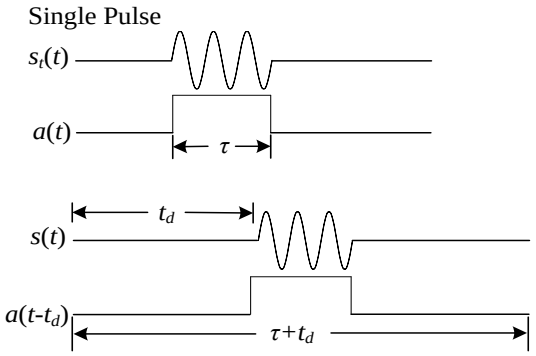

Figure 4.1 Radar single pulse waveforms.

Suppose that a signal $v(t)$ is observed in a background of exactly known, unvarying, white, Gaussian noise, of zero mean, over the interval $0 \le t \le \tau$; and a reflected radar signal $s(t)$, if present in the observation interval, has the form given in equation (4.4). Then, the problem under consideration is the development of Bayes decision rule to determine from the observation of $v(t)$ whether a signal of the form $s(t)$ exists in the resolution cell. When $s(t)$ has the form given in equation (4.4), the likelihood ratio can be expressed as:

$$l(v) = \exp\left[-\lambda + \frac{2}{N_0} \int_0^{\tau} v(t)s(t)dt \right] \tag{4.5}$$

where,

$N_0/2$ is the two sided noise power spectral density

$\lambda = E/N_0$ is the pre-detector received signal-to-noise energy ratio

E is the total received signal energy, at the antenna

The energy, E, of signal $s(t)$ is given by

$$E = \int_0^{\tau} s^2(t)dt \tag{4.6}$$

Bayes decision rules are developed for the reception of $s(t)$, for each of the following assumptions on amplitude A:

a. A is unknown and nonfluctuating

b. A is a random variable with Rayleigh distribution

c. A is a random variable with a one dominant plus Rayleigh distribution

It is assumed that the initial RF phase, ϕ, is unknown and follows a uniform distribution on interval $[0,2\pi]$. And further, it is assumed that detection is performed over an

arbitrary test cell in a background of exactly-known, unvarying, white, Gaussian noise with zero mean and a two-sided noise power spectral density of $N_0/2$. That is,

$$E[n(t)] = 0 \qquad 0 \le t \le \tau \tag{4.7}$$

and

$$E[n(t_1)n(t_2)] = \frac{N_0}{2}\delta(t_1 - t_2) \qquad 0 \le t_1 \le \tau, \quad 0 \le t_2 \le \tau \tag{4.8}$$

4.1.1 Single Pulse Linear Detection of Non-fluctuating Target

Suppose that the reflected radar signal $s(t)$ has the form given in equation (4.4), that amplitude A is unknown and non-fluctuating, and that initial RF phase, ϕ, is a uniformly distributed random variable on interval $[0,2\pi]$. Suppose further that $v(t)$ is a signal observed in a resolution cell over the interval $0 \le t \le \tau$. Then, the problem under consideration is the development of a Bayes decision rule to determine from the observation of $v(t)$ whether a signal of the form $s(t)$, under these assumptions, exists in the resolution cell. Let,

$$u_I(t) = a(t)\cos[\omega_0 t + \theta(t)], \qquad 0 \le t \le \tau \tag{4.9}$$

$$u_Q(t) = a(t)\sin[\omega_0 t + \theta(t)], \qquad 0 \le \mathrm{t} \le \tau \tag{4.10}$$

Then $u_I(t)$ and $u_Q(t)$ are called the quadrature components of signal $s(t)$, and

$$s(t) = Au_I(t)\cos\phi - Au_Q(t)\sin\phi \tag{4.11}$$

The total energy in $s(t)$, E, can be expressed as,

$$\begin{aligned} E &= A^2 \int_0^\tau u_I^2(t)dt \\ &= A^2 \int_0^\tau u_Q^2(t)dt \end{aligned} \tag{4.12}$$

Let,

$$\begin{aligned} \varepsilon &\underline{\Delta} \int_0^\tau u_I^2(t)dt \\ &= \int_0^\tau u_Q^2(t)dt \end{aligned} \tag{4.13}$$

Then $E=A^2\varepsilon$.

From equations (4.5) and (4.10), for a given ϕ, the likelihood ratio can be written as,

$$l(v|\phi) = e^{-\lambda} \exp\left[\frac{2A}{N_0}\int_0^{\tau} v(t)u_I(t)dt\cos\phi - \frac{2A}{N_0}\int_0^{\tau} v(t)u_Q(t)dt\sin\phi\right] \tag{4.14}$$

Let $I(v)$ and $Q(v)$ be defined as,

$$I(v) = k\int_0^{\tau} v(t)u_I(t)dt \quad \text{and} \quad Q(v) = k\int_0^{\tau} v(t)u_Q(t)dt \tag{4.15}$$

for some $k \neq 0$.

Since $u_I(t)$ and $u_Q(t)$ take non-zero values only on $[0,\tau]$, then $I(v)$ and $Q(v)$ are, respectively, the outputs of filters matched to $u_I(t)$ and $u_Q(t)$ having filter gain k.

Let,

$$D(v) = \sqrt{I^2(v) + Q^2(v)} \tag{4.16}$$

$$\alpha(v) = \arctan\left[\frac{Q(v)}{I(v)}\right] \tag{4.17}$$

Then,

$$\begin{aligned} l(v|\phi) &= e^{-\lambda} \exp\left\{\frac{2A}{kN_0}\left[I(v)\cos\phi - Q(v)\sin\phi\right]\right\} \\ &= e^{-\lambda} \exp\left\{\frac{2A}{kN_0}\sqrt{I^2(v) + Q^2(v)}\cos\left[\phi + \alpha(v)\right]\right\} \\ &= e^{-\lambda} \exp\left\{\frac{2A}{kN_0}D(v)\cos\left[\phi + \alpha(v)\right]\right\} \end{aligned} \tag{4.18}$$

Therefore,

$$\begin{aligned} l(v) &= E_\phi\left[l(v|\phi)\right] \\ &= \int_\phi e^{-\lambda} \exp\left\{\frac{2A}{kN_0}D(v)\cos\left[\phi + \alpha(v)\right]\right\} f_\phi(\phi)d\phi \\ &= \frac{1}{2\pi}\int_0^{2\pi} e^{-\lambda} \exp\left\{\frac{2A}{kN_0}D(v)\cos\left[\phi + \alpha(v)\right]\right\} d\phi \\ &= e^{-\lambda} I_0\left[\frac{2A}{kN_0}D(v)\right] \end{aligned} \tag{4.19}$$

where, $I_0(\cdot)$ is modified Bessel function of the first kind and order zero, defined by

$$I_0(a) \triangleq \frac{1}{2\pi}\int_0^{2\pi} e^{a\cos(\theta+\xi)}d\theta \tag{4.20}$$

where, ξ is an arbitrary angle.

Then, from equations (4.5) and (4.19), a Bayes decision rule for optimal single-pulse detection of reflected target signals with unknown, nonfluctuating amplitude, and unknown, uniformly distributed initial phase, in a background of exactly-known, unvarying, white Gaussian noise of zero mean, can be obtained as follows

Decide a target is present when,

$$I_0\left[\frac{2A}{kN_0}D(v)\right] \geq e^{\lambda}\kappa \tag{4.21}$$

Decide a target is not present when,

$$I_0\left[\frac{2A}{kN_0}D(v)\right] < e^{\lambda}\kappa \tag{4.22}$$

where κ is given as

decide d_1 ($s(t)$ present) when $l(v) \geq \kappa$

decide d_0 ($s(t)$ absent) when $l(v) < \kappa$

$$\kappa = \frac{qL(s=0|d_1)}{pL(s\neq 0|d_0)} \tag{4.23}$$

p is the a priori probability that the signal is present

q is the a priori probability that the signal is absent

Given $p_{l|n}(x)$ and $p_{l|y}(x)$, κ can be obtained by solution of equation following as

$$P_{fa} = \int_{\kappa}^{\infty} p_{l|n}(x)dx \tag{4.24}$$

and (P_d, P_{fa}, S/N) curves can be developed from below equation,

$$\begin{aligned} P_d &= P_r[l(v) \geq \kappa | s(t) \text{ is present }] \\ &= 1 - F_{l|y}(\kappa) \\ &= \int_{\kappa}^{\infty} p_{l|y}(x)dx \end{aligned} \tag{4.25}$$

However, density functions $p_{l|n}(x)$ and $p_{l|y}(x)$ are difficult to develop, and a receiver structure to implement this decision rule is difficult to construct, because of the need to develop the modified Bessel function. The decision rule can be simplified greatly by taking advantage of

the fact that $I_0(x)$ is a monotonically increasing function of x. This fact and the functional relationship between $I_0(x)$ and $D(v)$ insure that there exists a threshold T such that

$$D(v) \geq T \Leftrightarrow l(v) \geq \kappa \tag{4.26}$$

and

$$D(v) < T \Leftrightarrow l(v) < \kappa \tag{4.27}$$

So that Bayes decision rule reduce to,

Decide a target is present when

$$D(v) \geq T \tag{4.28}$$

Decide a target is not present when

$$D(v) < T \tag{4.29}$$

The receiver structure necessary to implement this test is illustrated in Fig. 1.2. This structure is much simpler than that employing the modified Bessel function and can be constructed without difficulty, at least approximately, using standard hardware and digital filter techniques. Detectors having the receiver structure described in tests (4.28) and (4.29) are called single pulse linear detectors.

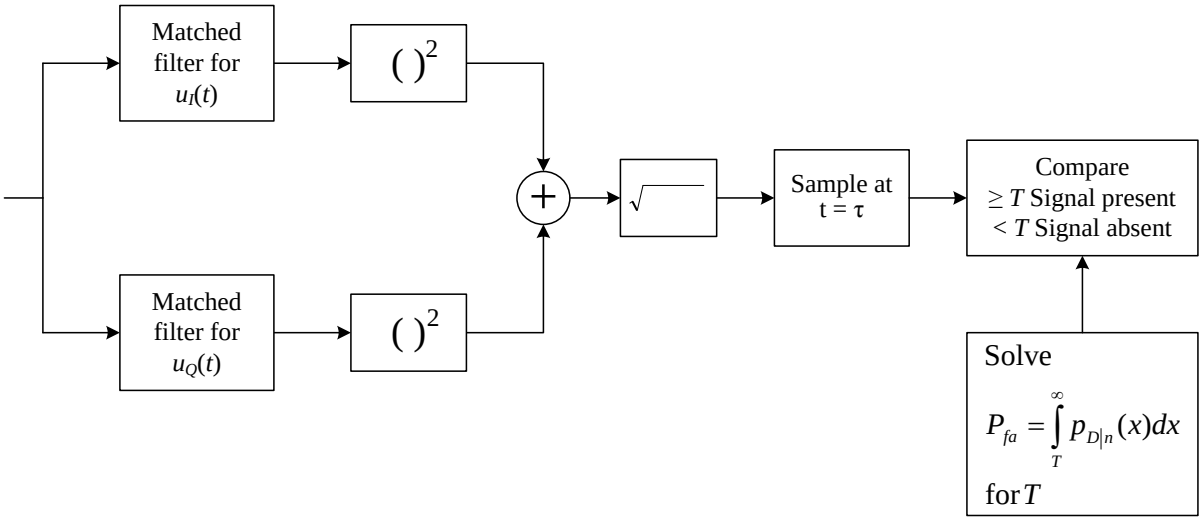

Figure 4.2 Optimal Single Pulse receiver.

Since $D(v)$ is a function of $v(t)$, a signal of duration τ, and $v(t)$ may be thought of as being a sampled function of one of two different random processes: $v|_n(t)$ and $v|_n(t)$, then when τ is fixed, $D(v)$ can be thought of as being a sampled function of one of two different

random variables: $D|_n(v)$ and $D|_y(v)$; where $D|_n(v)$ is sample $D(v)$ under the condition that no signal is present, and $D|_y(v)$ is sample $D(v)$ under the condition that both signal and noise are present.

Expressions for the density functions of $D|_n(v)$ and $D|_y(v)$, denoted $p_{D|n}(x)$ and $p_{D|y}(x)$, can be formed and used to determine threshold T and the (P_d,P_{fa},S/N) relationship. From Equations (4.27) and (4.28), for bayes decision receiver, the false alarm and detection probabilities associated with the detection of a signal $s(t)$ from observation $v(t)$ made over interval τ, are

$$\begin{aligned} P_{fa} &= \Pr[D(v) \geq T | s(t) \text{ is absent}] \\ &= 1 - F_{D|n}(T) \end{aligned} \tag{4.30}$$

and

$$\begin{aligned} P_d &= \Pr[D(v) \geq T | s(t) \text{ is present}] \\ &= 1 - F_{D|y}(T) \end{aligned} \tag{4.31}$$

where P_{fa} and P_d are the false alarm and detection probabilities, respectively, for detection over observation interval τ.

In modern radar systems, the principles of optimal single-pulse detection are applied primarily for optimal binary detection first threshold determination in systems with multiple CPIs at each resolution angle. They apply equally well to systems transmitting only one coherent pulse-train per resolution angle, or one single noncoherent pulse, although this application is less frequent. When only one coherent pulse-train is transmitted in a resolution angle, then the observation interval τ includes the entire resolution angle; so that P_{fa} and P_d, as given in equations (4.29) and (4.30), are typically the specified system false alarm and detection probabilities. In binary detection systems, the observation interval τ is a CPI and does not span the entire resolution angle; so that P_{fa} and P_d, associated with the detection of $s(t)$ (one coherent pulse-train), are not equal to the specified values for detection over the entire resolution angle. For binary detection strategies, P_{fa} and P_d, are the single-pulse false alarm and detection probabilities denoted $P_{fa}|_{sp}$ and $P_d|_{sp}$ respectively, for the detection of one of several transmitted coherent pulse-trains in the resolution angle. $P_{fa}|_{sp}$ and $P_d|_{sp}$ can be obtained from the specified values by the binary detection methods.

Given the P_{fa} for detection of waveform $s(t)$, detection threshold T in tests (4.28) and (4.29) can be obtained by a solution of

$$P_{fa} = \int_{T}^{\infty} p_{D|n}(x)dx \tag{4.32}$$

where, $p_{D|n}(x)$ is the probability density function of $D|_n(v)$.

Then, given T, the (P_{fa}, Pd, S/N) relationship can be obtained from

$$P_d = \int_{T}^{\infty} p_{D|y}(x)dx \tag{4.33}$$

where, $p_{D|n}(x)$ is the probability density function of $D|_y(v)$.

In the remaining paragraphs of this section, an expression for detection threshold T is first developed, then used to determine the classical (P_d, P_{fa}, S/N) relationship for detection according to tests (4.28) and (4.29), when detection is performed in an exactly-known, unvarying, white, Gaussian noise environment to distinguish reflected signals of the form given in equation (4.4), with unknown nonfluctuating amplitude, and initial RF phase a uniformly distributed random variable on the interval [0,2π].

4.1.2 Detection Threshold Determination

By definition,

$$\begin{aligned} P_{fa} &= \Pr[\, D(v) \geq T \,|\, s(t) \text{ is absent} \,] \\ &= \int_{T}^{\infty} p_{D|n}(x)dx \end{aligned} \tag{4.34}$$

From equation (4.16),

$$D(v) = \sqrt{I^2(v) + Q^2(v)} \tag{4.35}$$

where $I(v)$ and $Q(v)$ are given in equation (4.16).

Then, when $s(t)$ is not present in the resolution cell over observation interval τ,

$$v(t) = n(t) \qquad 0 \leq t \leq \tau \tag{4.36}$$

So that, $I(v)$ and $Q(v)$ are

$$I(v) = k\int_{0}^{\tau} n(t)u_I(t)dt \tag{4.37}$$

$$Q(v) = k\int_{0}^{\tau} n(t)u_Q(t)dt \tag{4.38}$$

for some filter gain $k \neq 0$.

Then, $D|n(v)$ is

$$D|n(v) = \sqrt{\left[k\int_0^\tau n(t)u_I(t)dt\right]^2 + \left[k\int_0^\tau n(t)u_Q(t)dt\right]^2} \tag{4.39}$$

$I(v)$ and $Q(v)$ are independent normal random variables with mean 0 and variance $N_0k^2\varepsilon/2$, and $D|n(v)$ is therefore to have a Rayleigh distribution with probability density function:

$$p_{D|n}(x) = \frac{2x}{N_0k^2\varepsilon}e^{-x^2/N_0k^2\varepsilon} \quad x \geq 0 \tag{4.40}$$

from equations (4.34) and (4.40),

$$\begin{aligned} p_{fa} &= \int_T^\infty \frac{2x}{N_0k^2\varepsilon}e^{-x^2/N_0k^2\varepsilon}dx \\ &= -e^{-x^2/N_0k^2\varepsilon}\Big|_T^\infty \\ &= -e^{-T^2/N_0k^2\varepsilon} \end{aligned} \tag{4.41}$$

or,

$$\begin{aligned} T &= \sqrt{N_ok^2\varepsilon\ln(P_{fa}^{-1})} \\ &= \sigma\sqrt{2\ln(P_{fa}^{-1})} \end{aligned} \tag{4.42}$$

where $\sigma = k\sqrt{N_0\varepsilon/2}$ is the Rayleigh parameter. Therefore, given P_{fa}, detection threshold T can be determined from equation (4.42) if N_0 and ε are known. ε is a function of known parameters and can be determined from equation (4.13). So, T can be determined from equation (4.42) whenever N_0 is known. In environments where noise energy is due to solely to receiver noise, N_0 is constant and measurable, so that detection threshold T is constant, known, and given by equation (4.42).

Equation (4.42) can also be written as

$$T = E\left[D|n(v)\right]\sqrt{\frac{4}{\pi}\ln(P_{fa}^{-1})} \tag{4.43}$$

where $E[D|n(v)]$ is the statistical expectation of $D|n(v)$. Often, in varying noise or Rayleigh envelope clutter environments, when N_0 cannot be measured or accurately estimated, equation (4.42) is used to provide an estimate for detection threshold T. Typically, in these

cases, T is developed by forming estimates of $E[D|n(v)]$ from resolution cells surrounding the cell under test. This is the underlying principle of cell averaging (sliding window) CFAR.

4.1.3 P_D, P_{FA}, S/N Curves

In this section, the classical (P_d,P_{fa},S/N) relationship is developed for detection according to test (4.13), when detection is performed in an exactly-known, unvarying, white, Gaussian (thermal or receiver) noise environment to distinguish reflected signals, of the form given in equation (4.4), with unknown nonfluctuating amplitude, and initial RF phase: a uniformly distributed random variable on the interval $[0,2\pi]$. In order to determine the (P_d,P_{fa},S/N) relationship, an expression for P_d is developed that includes P_{fa} and S/N as variables. To develop this expression for P_d, recall that by definition

$$\begin{aligned} P_d &= P_r[D(v) \geq T | s(t) \text{ is present }] \\ &= \int_T^{\infty} p_{D|y}(x)dx \end{aligned} \tag{4.44}$$

where, $P_{D|n}(x)$ is the probability density function of $D(v)$ under the condition that both signal and noise are present in the resolution cell under test.

When signal $s(t)$ is present in the resolution cell over observation interval τ,

$$v(t) = s(t) + n(t) \quad 0 \leq t \leq \tau \tag{4.45}$$

Then,

$$\begin{aligned} I(v) &= k\int_0^{\tau} [s(t) + n(t)]u_I(t)dt \\ &= k\int_0^{\tau} [Au_I(t)u_I(t)\cos\phi - Au_Q(t)u_I(t)\sin\phi + n(t)u_I(t)]dt \\ &= kA\varepsilon\cos\phi - kA\sin\phi\int_0^{\tau} u_Q(t)u_I(t)dt + k\int_0^{\tau} n(t)u_I(t)dt \end{aligned} \tag{4.46}$$

The second term above can be shown to be approximately zero, so that

$$I(v) = kA\varepsilon\cos\phi + k\int_0^{\tau} n(t)u_I(t)dt \tag{4.47}$$

Similarly,

$$
\begin{aligned}
Q(v) &= k\int_0^{\tau}\left[s(t)+n(t)\right]u_Q(t)dt \\
&= k\int_0^{\tau}\left[Au_I(t)u_Q(t)\cos\phi - Au_Q(t)u_Q(t)\sin\phi + n(t)u_Q(t)\right]dt \\
&= kA\cos\phi\int_0^{\tau}u_I(t)u_Q(t) - kA\varepsilon\sin\phi + k\int_0^{\tau}n(t)u_Q(t)dt \\
&= -kA\varepsilon\sin\phi + k\int_0^{\tau}n(t)u_Q(t)dt
\end{aligned}
\tag{4.48}
$$

Suppose ϕ is given. Let $I|_{\phi}(v)$ and $Q|_{\phi}(v)$ be functions $I(v)$ and $Q(v)$, respectively , under the condition that ϕ is given. Then, since $n(t)$ is a Gaussian random process, $I|_{\phi}(v)$ and $Q|_{\phi}(v)$ are Gaussian random variables. Further, it can be shown that

$$
E\left[I\big|_{\phi}(v)Q\big|_{\phi}(v)\right] = E\left[I\big|_{\phi}(v)\right]E\left[Q\big|_{\phi}(v)\right] \tag{4.49}
$$

So, $I|_{\phi}(v)$ and $Q|_{\phi}(v)$ are independent random variables. It can also be shown that both $I|_{\phi}(v)$ and $Q|_{\phi}(v)$ have variance: $N_0k^2\varepsilon/2$; and means

$$
E\left[I\big|_{\phi}(v)\right] = kA\varepsilon\cos\phi \tag{4.50}
$$

and

$$
E\left[Q\big|_{\phi}(v)\right] = -kA\varepsilon\sin\phi \tag{4.51}
$$

Therefore, for a given initial phase ϕ, the joint probability density function of random variables $I(v)$ and $Q(v)$ under the assumption that a signal is present in the resolution cell over observation interval τ, denoted $P_{I,Q|y,\phi}(x,z)$, is given by

$$
p_{I,Q|y,\phi}(x,z) = \frac{1}{\pi N_0k^2\varepsilon}\exp\left\{-\frac{1}{N_0k^2\varepsilon}\left[(x-kA\varepsilon\cos\phi)^2 + (z+kA\varepsilon\sin\phi)^2\right]\right\} \tag{4.52}
$$

Let,

$$
\alpha(v) = \arctan\left[\frac{Q(v)}{I(v)}\right] \tag{4.53}
$$

Then, since

$$
D\big|_y(v) = \sqrt{I^2(v)+Q^2(v)} \tag{4.54}
$$

by applying a change of variables to equation (4.52), for a given initial phase ϕ, the joint density function of random variables $D|_y(y)$ and $\alpha(v)$ under the assumption that a signal is present in the resolution cell over observation interval τ, denoted $P_{D,\alpha|y,\phi}(r,a)$, is given by

$$\begin{aligned} p_{D,\alpha|y,\phi}(r,a) &= \frac{r}{\pi N_0 k^2 \varepsilon} \exp\left\{ -\frac{1}{N_0 k^2 \varepsilon} \left[(r\cos a - kA\varepsilon\cos\phi)^2 + (r\sin a + kA\varepsilon\sin\phi)^2 \right] \right\} \\ &= \frac{r}{\pi N_0 k^2 \varepsilon} \exp\left\{ -\frac{1}{N_0 k^2 \varepsilon} \left[(r^2 - 2kA\varepsilon r\cos(a+\phi) + k^2 A^2 \varepsilon^2 \right] \right\} \end{aligned} \tag{4.55}$$

Then the density function of $D|_y(v)$ for a given initial phase ϕ, denoted $P_{D|y,\phi}(r)$, can be obtained by integrating $P_{D,\alpha|y,\phi}(r,a)$ over the range of variable α. So that,

$$\begin{aligned} p_{D|y,\phi}(r) &= \int_0^{2\pi} p_{D,\alpha|y,\phi}(r,a)da \\ &= \int_0^{2\pi} \frac{r}{\pi N_0 k^2 \varepsilon} \exp\left\{ -\frac{1}{N_0 k^2 \varepsilon} \left[(r^2 - 2kA\varepsilon r\cos(a+\phi) + k^2 A^2 \varepsilon^2 \right] \right\} da \\ &= \frac{2r}{N_0 k^2 \varepsilon} \exp\left\{ -\left[\lambda + \frac{r^2}{N_0 k^2 \varepsilon} \right] \right\} I_0\left[\frac{2A}{kN_0} r \right], \qquad \text{where } \lambda = \frac{E}{N_0} \end{aligned} \tag{4.56}$$

The probability density function of $D|_y(v)$ can be obtained from $P_{D|y,\phi}(r)$ by assuming a distribution for ϕ and forming the expectation of $P_{D|y,\phi}(r)$ with respect to ϕ. That is

$$p_{D|y}(r) = E_\phi[p_{D|y,\phi}(r)] \tag{4.57}$$

Since ϕ is assumed to be a uniformly distributed random variable on interval $[0,2\pi]$, then,

$$\begin{aligned} p_{D|y}(r) &= \frac{1}{2\pi} \int_0^{2\pi} p_{D|y,\phi}(r)d\phi \\ &= \frac{2r}{N_0 k^2 \varepsilon} \exp\left\{ -\left[\lambda + \frac{r^2}{N_0 k^2 \varepsilon} \right] \right\} I_0\left[\frac{2A}{kN_0} r \right] \end{aligned} \tag{4.58}$$

From equation (4.44) and (4.58),

$$\begin{aligned} p_d &= \int_T^\infty p_{D|y}(x)dx \\ &= \frac{2}{N_0 k^2 \varepsilon} \int_T^\infty r \exp\left\{ -\left[\lambda + \frac{r^2}{N_0 k^2 \varepsilon} \right] \right\} I_0\left[\frac{2A}{kN_0} r \right] dr \end{aligned} \tag{4.59}$$

Letting $y = r\sqrt{\frac{2}{N_0 k^2 \varepsilon}}$

$$p_d = \int_{T\sqrt{\frac{2}{N_0 k^2 \varepsilon}}}^{\infty} y \exp\left\{-\left[\lambda + \frac{y^2}{2}\right]\right\} I_0\left[y\sqrt{2\lambda}\right] dy \tag{4.60}$$

And, from equation (4.41),

$$p_d = \int_{\sqrt{2\ln(p_{fa}^{-1})}}^{\infty} y \exp\left\{-\left[\lambda + \frac{y^2}{2}\right]\right\} I_0\left[y\sqrt{2\lambda}\right] dy \tag{4.61}$$

Equation (4.61) shows P_d to be a function of P_{fa} and λ. When the receiver is matched to the reflected signal $s(t)$, it can be shown that the average single-pulse signal-to-noise power ratio at the detector output (S/N) is equal to λ. Then, equation (4.61), can be solved numerically to provide the classical (P_d,P_{fa},S/N) curves for detection according to tests (4.28) and (4.29), when detection is performed in an exactly-known, unvarying, white, Gaussian noise environment to distinguish reflected single-pulse radar signals of the form given in equation (4.4), with unknown, nonfluctuating amplitude and uniformly distributed initial phase. Plots of this relationship are commonly called the Swerling curves for single-pulse detection on nonfluctuating targets or, the Swerling case 0 curves for a single-pulse pulse-train. Equation (4.61) has been solved and plotted in Fig. 4.4.1.1.2-1 [32] for several important values of P_{fa}.

4.2 Proposed Detection Algorithm

The block diagram of a UWB radar system is split into two; the transmitter part and the receiver part. In the transmitter part, the pulses are initiated by the Pulse Repetition Frequency (PRF) generator which triggers the pulse generator. Then Gaussian pulses with sub-nano second duration as shown in Fig. 4.3 are generated in turn by pulse generator.

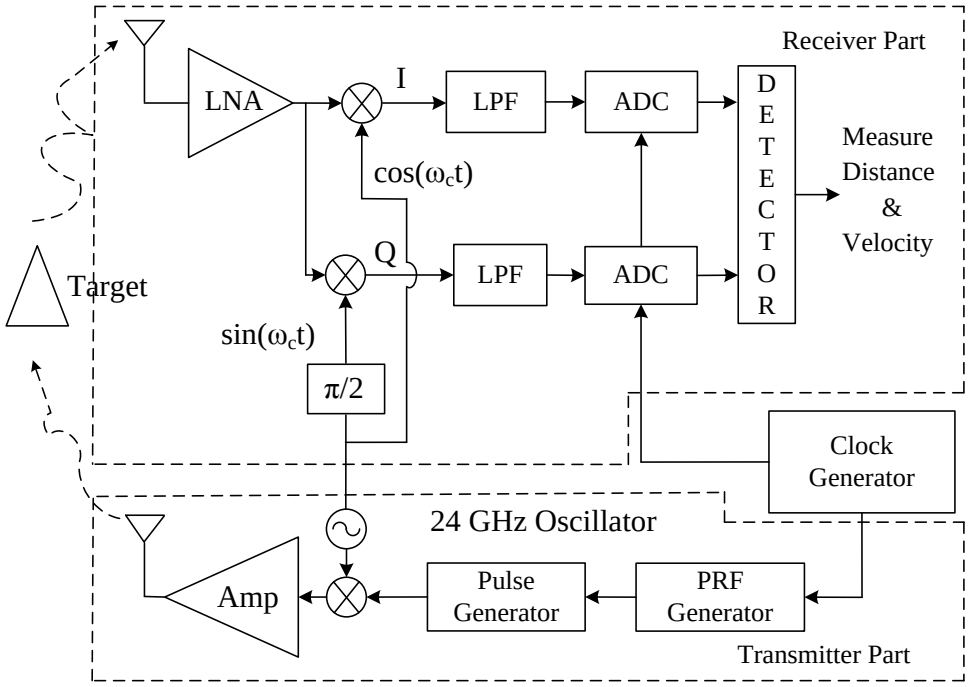

Figure 4.3 Block Diagram of UWB radar system.

The Pulse Repetition Interval (PRI) is controlled by the maximum range of the radar. The maximum range for unambiguous range depends on the pulse repetition frequency and can be written as follows

$$R_{\max} = \frac{c}{2 \cdot f_{PRF}} \tag{4.62}$$

where f_{PRF} is pulse repetition frequency and c is the velocity of light. And the range resolution can be written as

$$\Delta R = \frac{c \cdot T_P}{2} \tag{4.63}$$

where T_p is pulse width and c is the velocity of light. And then the transmitted signal can be written as follows

$$s(t) = A_T \cdot \cos(2\pi f_c t + \varphi_0) \cdot \sum_{n=-\infty}^{\infty} p(t - n \cdot T_{PRI}) \tag{4.64}$$

where $p(t)$ is the Gaussian pulse as follows

$$p(t) = \exp\left[-2\pi \left(\frac{t}{\tau_p} \right)^2 \right] \tag{4.65}$$

The parameters employed in this UWB radar system are described as follows.

- τ_p is the time normalization factor that decide the pulse width
- A_T is the amplitude of single transmit pulse
- f_c is the carrier frequency
- φ_0 is the initial phase of the transmit signal
- T_{PRI} is the pulse repetition interval.

The form of the transmitted signal in this system is known, but the received signal usually is not completely known. Since the range resolution of this UWB radar system is much less than the extent of the target, the received signal is the summation of the time-spaced echoes from the individual scattering centers that constitute the target [5]. In this sub-chapter, we assume that the target is stationary and the target has L independent reflecting cells. Then the target model is written as

$$h(t) = \sum_{l=0}^{L-1} \delta(t - \tau_l) \tag{4.66}$$

where L is the number of scatters, the amplitude of the scatters α_l, and the time delays of the scatters τ_l are all unknown. We assume that the τ_0 in Fig. 4.4 indicates the target range.

The radiated electromagnetic signals generated by the transmit antenna is reflected by the target and they are received in the receiver antenna. First, the received signal is pre-amplified by the Low Noise Amplifier (LNA). Then the signal is multiplied with local carrier signal and divided between the in-phase and quadrature-phase baseband signal as shown in Fig. 4.3. We assume that the low pass filter will match the pulse envelope spectral shape as close as possible to provide a fully matched optimum filter.

Then the baseband received signal $r(t)$ is written as

$$r(t) = A_T \sum_{n=-\infty}^{+\infty} \sum_{l=0}^{L-1} \alpha_l \cdot e^{j\theta_l} p(t - nT_{PRI} - \tau_l) + n(t) \tag{4.67}$$

Where $n(t)$ is the white Gaussian noise (WGN) with two-sided power spectral density $N_0/2$ and θ_l is the arbitrary phase of l-th scatter that can be written as $\theta_l = -2\pi f_c \tau_l + \varphi_0$. The sampling rate of the A/D converters is same to the pulse width. And we assume that the baseband received signal is sampled at peak point of $p(t)$ as like the Fig. 1.4. When the target size is greater than the radar resolution, then the echo consists of a signal characterized by equation (4.66) and Fig. 4.4; the received signal will be composed of individual short duration signals. A gain rather than a loss can be obtained when a high-resolution waveform resolves the individual scatters of a distributed target such as the UWB radar system. Because there will be no signal addition from close scattering centers, detection will be depend on the reflected strength of individual centers for weak returns [5]-[34].

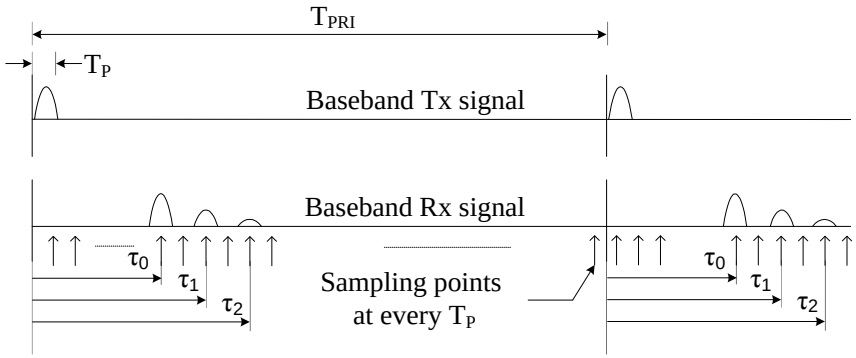

Figure 4.4 Transmitted signal and received baseband signal.

4.2.1 Squared Sliding Window Detector

The detector of the UWB radar receiver must determine that a signal of interest is present or absent. And then the UWB radar processes it for some useful purpose such as range determination, movement, and etc [5]. In this chapter, we propose the detection algorithm for the range determination, as shown in Fig. 4.5. The proposed detector consists of the coherent integration, squared sliding window and non-coherent integration. The proposed detector with the squared sliding window can gather the total reflected signals. The in-phase (I) and quadrature (Q) sampled values at every T_p are used as the input of the detector. It is assumed that the sampling rate (T_p) is same to the pulse width of 2 ns and the range resolution can be 30cm from equation (4.63). Also it is assumed that the maximum target range is 30m and by using equation (4.62) we can get T_{PRI} of 200 ns. From the above-mentioned range resolution and maximum target range, the range gates of at least 100 are required to detect the target. It is equal to the number of memory in the coherent and non-coherent integration. The sampled value at every T_p is applied to the switch I of the coherent integration. The switch I

is shifted at every T_p sample, i.e., the range gate. It takes $N_c \cdot T_{PRI}$ to coherently integrate and dump for all of the range gates.

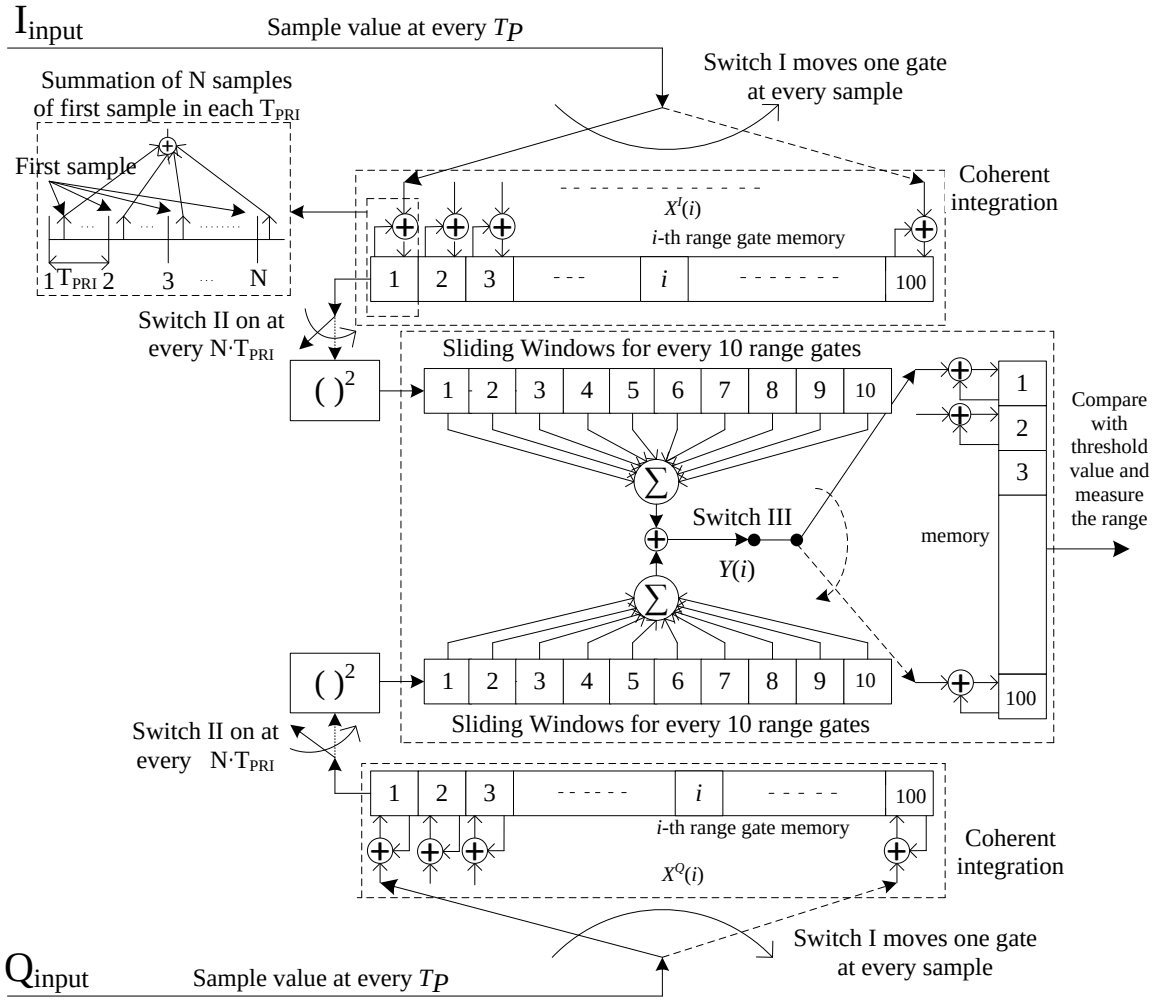

Figure 4.5 Block Diagram of the proposed detector.

Also it is assumed that the maximum target range is 30*m* and by using equation (4.62) we can get T_{PRI} of 200*ns*. From the above mentioned range resolution and maximum target range, the range gates of at least 100 are required to detect the target. It is equal to the number of memory in the coherent and non-coherent integration. The sampled value at every T_p is applied to the switch I of the coherent integration. The switch I is shifted at every T_p sample i.e., the range gate. It takes $N_c.T_{PRI}$ to coherently integrate and dump for all of the range gates. The coherent integration for the *i*-th range gate in I branch can be expressed as follows

$$X^I(i) = \frac{1}{N_c}\sum_{n=1}^{N_c} \mathrm{Re}\left\{r_n(iT_p)\right\} \tag{4.68}$$

where

$$r_n(iT_p) = A_T \sum_{l=0}^{L-1} \alpha_l \cdot e^{j\theta_l} p((nT_{PRI} + iT_p) - nT_{PRI} - \tau_l) + \mathrm{n}'(nT_{PRI} + iT_p) \tag{4.69}$$

and where n' $(nT_{PRI}+iT_p)$ is a sampled value of $n(t)$ at $nT_{PRI}+iT_p$. Then the summations for each gate are stored in each memory of the coherent integration. Therefore it is possible to achieve an improvement of signal-to-noise ratio (SNR) as much as $10\cdot\log(N_c)$ [dB].

The squared sliding window with size 10 receives sample values from the coherent integration. The squared sliding window operates at every $N_c \cdot T_{PRI}$. The squared 10 range gate samples are combined and then both I and Q branch values are summed. The output of the squared sliding window $Y(i)$ can be represented as

$$Y(i) = \sum_{\mathrm{j}=1}^{10} \left\{X^I(i+j)\right\}^2 + \left\{X^Q(i+j)\right\}^2 \tag{4.70}$$

All of the reflected signals from the distributed target can be added non-coherently.

The value $Y(i)$ is stored in the i-th register of the non-coherent integration at every $N_c \cdot T_{PRI}$ for $N_c \cdot N_{nc} \cdot T_{PRI}$. The output of the non-coherent integration $Z(i)$ can be written as

$$Z(i) = \sum_{m=1}^{N_{nc}} Y_m(i) \tag{4.71}$$

where $Y_m(i)$ is the output of the squared sliding window at $N_{nc} \cdot N_c \cdot T_{PRI}$. If the above result is greater than the defined threshold, then we can determine that a target is present. And the index i represents the position of the target; the target range indicates $i \cdot 30$ cm. It takes $N_c \cdot N_{nc} \cdot T_{PRI}$ to decide the target range.

4.2.2 Non-coherent Detector

The detector of the UWB radar receiver must determine that a signal of interest is present or absent. And then the UWB radar processes it for some useful purpose such as range determination, movement, and etc. In this thesis, we analyze the performance of non-coherent detectors against a background of white Gaussian noise for range determination, as shown in Fig. 3. The non-coherent detectors consist of coherent integration, non-coherent detector and non-coherent integration.

The in-phase (I) and quadrature (Q) sampled values at every T_p are used as the input of the detector. It is assumed that the sampling rate (T_p) is same to the pulse width of 2 ns and the range resolution can be 30cm from (4.63). Also it is assumed that the maximum target range is 30m and by using (4.62) we can get T_{PRI} of 200 ns. From the above-mentioned range resolution and maximum target range, the range gates of at least 100 are required to detect the target. It is equal to the number of memory in the coherent and non-coherent integration. The sampled value at every T_p is applied to the switch I of the coherent integration. The switch I is shifted at every T_p sample, i.e., the range gate. It takes $N \cdot T_{PRI}$ to coherently integrate and dump for all of the range gates.

The coherent integration for the *i*-th range gate in I branch can be expressed as follows

$$X^I(i) = \frac{1}{N_c} \sum_{n=1}^{N_c} \mathrm{Re}\left\{ r_n(iT_p) \right\} \tag{4.72}$$

where

$$r_n(iT_p) = A_T \sum_{l=0}^{L\text{-}1} \alpha_l \cdot e^{j\theta_l} p((nT_{PRI} + iT_p) - nT_{PRI} - \tau_l) + \mathrm{n}'(nT_{PRI} + iT_p) \tag{4.73}$$

and where $n'(nT_{PRI}+iT_p)$ is a sampled value of $n(t)$ at $nT_{PRI}+iT_p$. Then the summations for each gate are stored in each memory of the coherent integration. Therefore it is possible to achieve an improvement of signal-to-noise ratio (SNR) as much as $10 \cdot \log(N)$ [dB].

The sample value received from the coherent integration is squared and operates at every $N \cdot T_{PRI}$. The squared range gate samples are combined and then both I and Q branch values are summed as shown in Fig. 4a. The output after squaring $Y(i)$ is known as square law detector can be represented as

$$Y(i) = \left\{ X^I(i) \right\}^2 + \left\{ X^Q(i) \right\}^2 \tag{4.74}$$

In the case of a linear detector as shown in Fig. 4b the sample value received from the coherent integration is squared and operates at every $N \cdot T_{PRI}$. The squared range gate samples are combined and then both I and Q branch values are summed and square root is applied to the summed value. The output of the linear detector $Y(i)$ can be represented as

$$Y(i) = \sqrt{\left\{ X^I(i) \right\}^2 + \left\{ X^Q(i) \right\}^2} \tag{4.75}$$

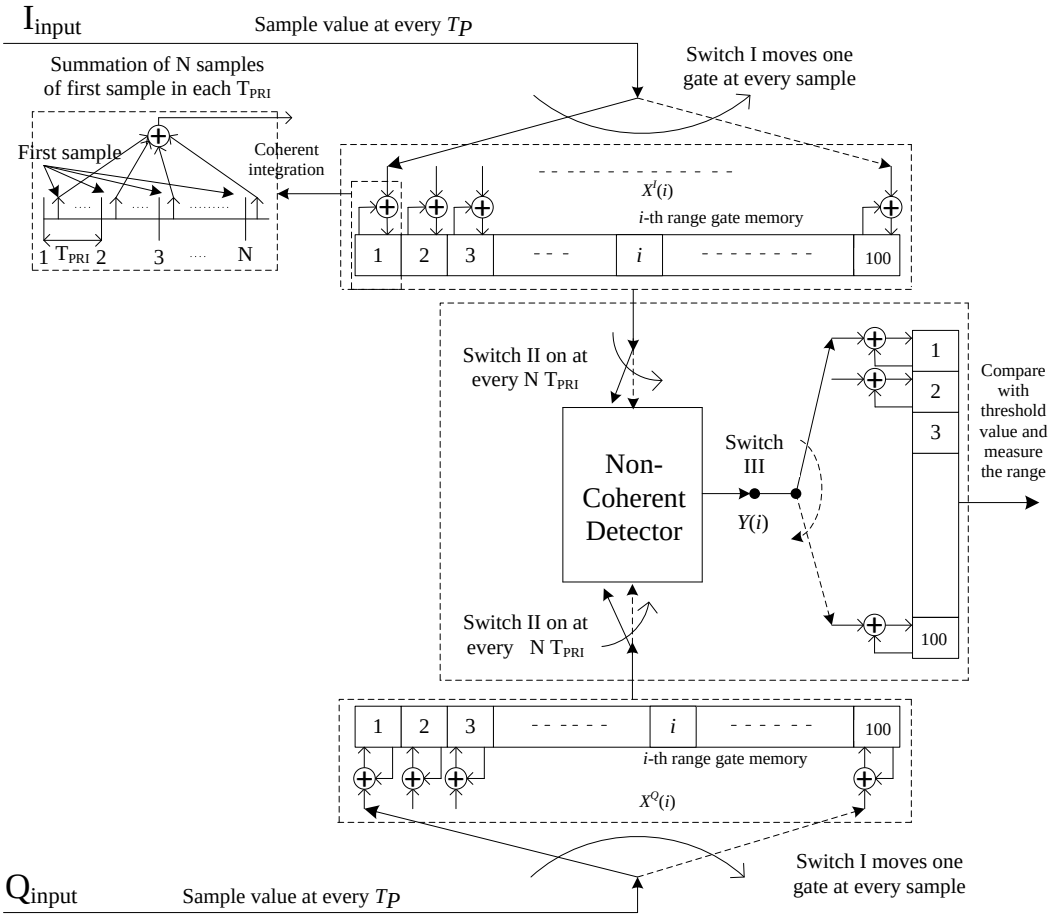

Figure 4.6 Block Diagram of the proposed non-coherent detector.

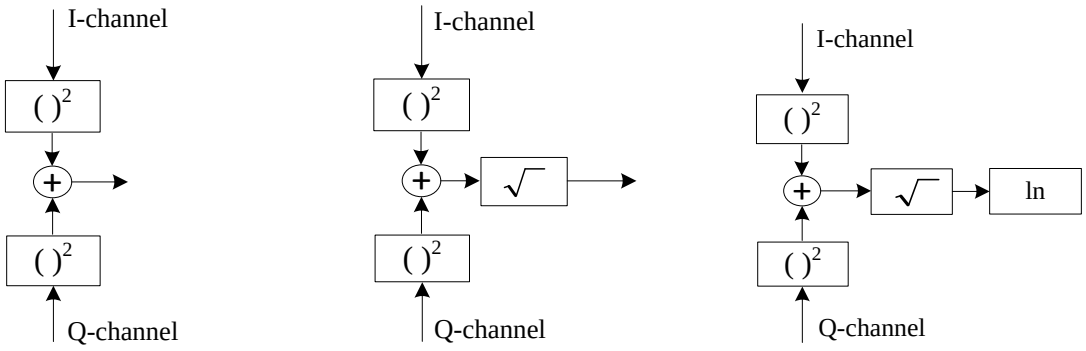

(a)Square Law (b) Linear (c) Logarithmic Detector

Figure 4.7 Non-coherent detectors.

In Logarithmic detector as shown in Fig. 4c the sample value received from the coherent integration is squared and operates at every $N \cdot T_{PRI}$. The squared range gate samples are combined and then both I and Q branch values are summed and square root is applied to

the summed value and natural logarithm is taken. The output of the logarithmic detector $Y(i)$ can be represented as

$$Y(i) = \ln\left(\sqrt{\left\{X^I(i)\right\}^2 + \left\{X^Q(i)\right\}^2} \right) \tag{4.76}$$

All of the reflected signals from the distributed target can be added non-coherently.

The value $Y(i)$ is stored in the i-th register of the non-coherent integration at every $N_c \cdot T_{PRI}$ for $N_c \cdot N_{nc} \cdot T_{PRI}$. The output of the non-coherent integration $Z(i)$ can be written as

$$Z(i) = \sum_{m=1}^{N_{nc}} Y_m(i) \tag{4.77}$$

where $Y_m(i)$ is the output of the squared sliding window at $N_{nc} \cdot N_c \cdot T_{PRI}$. If the above result is greater than the defined threshold, then we can determine that a target is present. And the index i represents the position of the target; the target range indicates $i \cdot 30$ cm. It takes $N_c \cdot N_{nc} \cdot T_{PRI}$ to decide the target range.

4.3 Detection and False Alarm Probability

To calculate the detection characteristics, the probability density functions $p_0(z)$ and $p_1(z)$ of $Z(i)$ should be determined. If the echo signal is absent, then the probability density function $p_0(z)$ is determined at the detector output by using the following expression [36].

$$p_0(z) = \frac{1}{\sigma^2 2^{n/2} \Gamma(n/2)} z^{(n/2)-1} e^{-z/2\sigma^2} \tag{4.78}$$

Where the central chi-square distribution $p_0(z)$ with n degree of freedom has zero mean and variance σ^2. And if the echo signal is present, then the probability density function $p_1(z)$ is determined as following [11].

$$p_1(z) = \frac{1}{2\sigma^2}\left(\frac{z}{s^2}\right)^{(n-2)/4} e^{-(s^2+z)/2\sigma^2} I_{(n/2)-1}\left(\sqrt{z}\,\frac{s}{\sigma^2}\right) \tag{4.79}$$

where $I_{n/2\text{-}1}$ is the n-th order modified Bessel function of the first kind. The non-central chi-square distribution $p_1(z)$ with n degree of freedom has mean s^2 and variance σ^2.

To get the detection and false alarm probability, we must calculate the following integral; the probability of false alarm can be written as

$$P_{FA} = \int_{u_{th}}^{\infty} \frac{1}{\sigma^2 2^{n/2} \Gamma(n/2)} z^{(n/2)-1} e^{-z/2\sigma^2} dz \tag{4.80}$$

and the probability of detection is given as

$$P_D = \int_{u_{th}}^{\infty} \frac{1}{2\sigma^2}\left(\frac{z}{s^2}\right)^{(n-2)/4} e^{(s^2+z)/2\sigma^2} I_{(n/2)-1}\left(\sqrt{z}\,\frac{s}{\sigma^2}\right) dz \tag{4.81}$$

where u_{th} is the threshold value. On the basis of the above mentioned formulas, the detection characteristics of the received echo signal is determined for proposed detector.

4.4 Simulation result in Gaussian noise environment for squared sliding window detector

The purpose of the simulation is to assess the performance of the proposed detector. First, we compare theoretical results with computer simulation results by using the probability density function. And then the probabilities of detection and false alarm are evaluated. In the simulation we use the target model with flare points locations and percentage of total energy reflected from each flare point as given in table 4.1. We simulate

the probability density functions using the parameters as given in table 4.2. A large enough number of trials are used to obtain each point of the probability density functions. The number of trials is about 1000000 times. The signal-to-noise ratio (SNR) is defined as $\bar{E}/N_0$, where $\bar{E}$ represents the total average energy reflected from a target.

Table 4.1 Target model with flare points locations [33].

Model Number	Cell Number									
	1	**2**	**3**	**4**	**5**	**6**	**7**	**8**	**9**	**10**
1	1	0	0	0	0	0	0	0	0	0
2	1/2	0	1/2	0	0	0	0	0	0	0
3	1/3	0	1/3	0	1/3	0	0	0	0	0
4	1/4	0	1/4	0	1/4	0	1/4	0	0	0
5	1/5	0	1/5	0	1/5	0	1/5	0	1/5	0
6	1/6	1/6	1/6	0	1/6	0	1/6	0	1/6	0
7	3/4	0	1/4	0	0	0	0	0	0	0
8	3/4	0	1/8	0	1/8	0	0	0	0	0
9	3/4	0	1/16	0	1/16	0	1/16	0	1/16	0
10	1/2	0	1/4	0	1/4	0	0	0	0	0

Table 4.2 System parameters for stationary target.

Parameter	**Notation**	**Value**
Pulse Repetition Interval	T_{PRI}	200ns
Pulse Width	T_P	2ns
Maximum Target Range	R_{max}	30m
Range Resolution	ΔR	30cm
Number of coherent integration	N_c	10
Number of non-coherent integration	N_{nc}	1
Sliding window size	L	10

4.4.1 Probability Density Function

Fig. 4.8 shows the result of the probability density functions (PDF) $p_0(z)$ and $p_1(z)$ for model number 9 at $\bar{E}/N_0$=4dB. The method without sliding window refers to the conventional non-coherent detector and detects the maximum flare point. The simulation result with sliding window (S_W) and without sliding window is compared with the theoretical result. It shows that the simulation result and the theoretical result are in excellent agreement. And the PDF with sliding window has 20 degrees of freedom and the average signal energy is 1. On the other hand, the PDF without sliding window has 2 degrees of freedom and the average signal energy is 3/4. Therefore the PDF with sliding window is more spread than without sliding window. By using the probability density functions, the detection characteristics of the detector can be plotted.

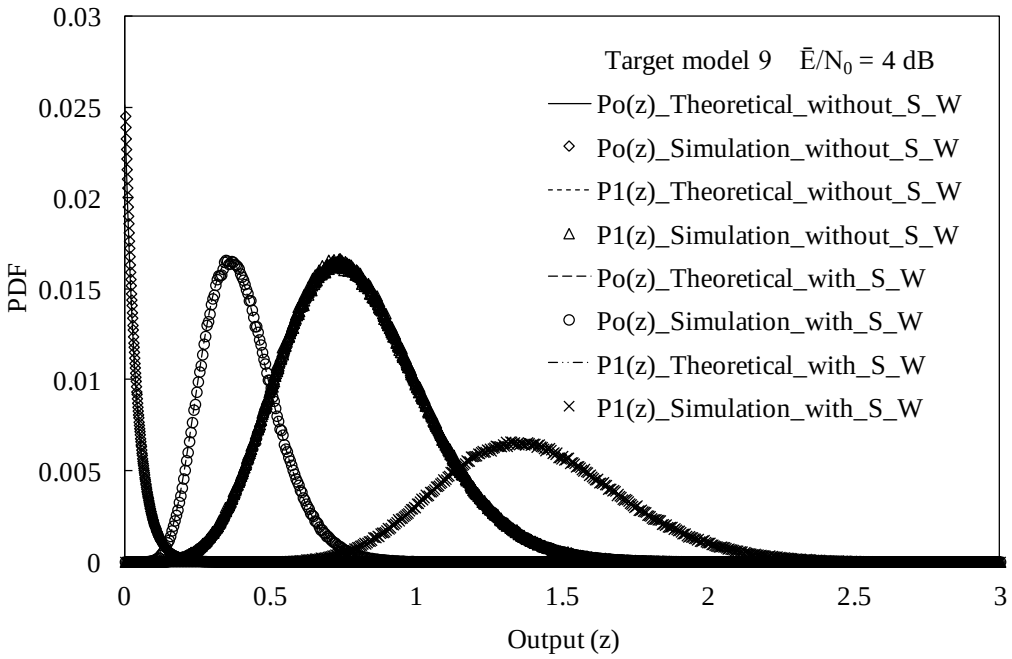

Figure 4.8 The probability density function.

4.4.2 Region of Convergence (ROC)

Fig. 4.9 shows the detection probability versus the false alarm probability for various stationary target models at $\bar{E}/N_0$=0dB. The proposed detector with sliding window has same average signal energy for all target models. On the other hand, the method without sliding window has different average signal energy such as 1/2, 1/3, 1/4, 1/6, and 3/4 because the maximum flare point is only used. The result shows that the performance of the detector with

sliding window is found to be better as the energy reflected from the target is more distributed. But the performance of the detector without sliding window is reduced as the target is more distributed. We can predict that if the pulse width is very narrow such as sub-nano second duration, then the energy is more spread and the proposed detector with sliding window is superior.

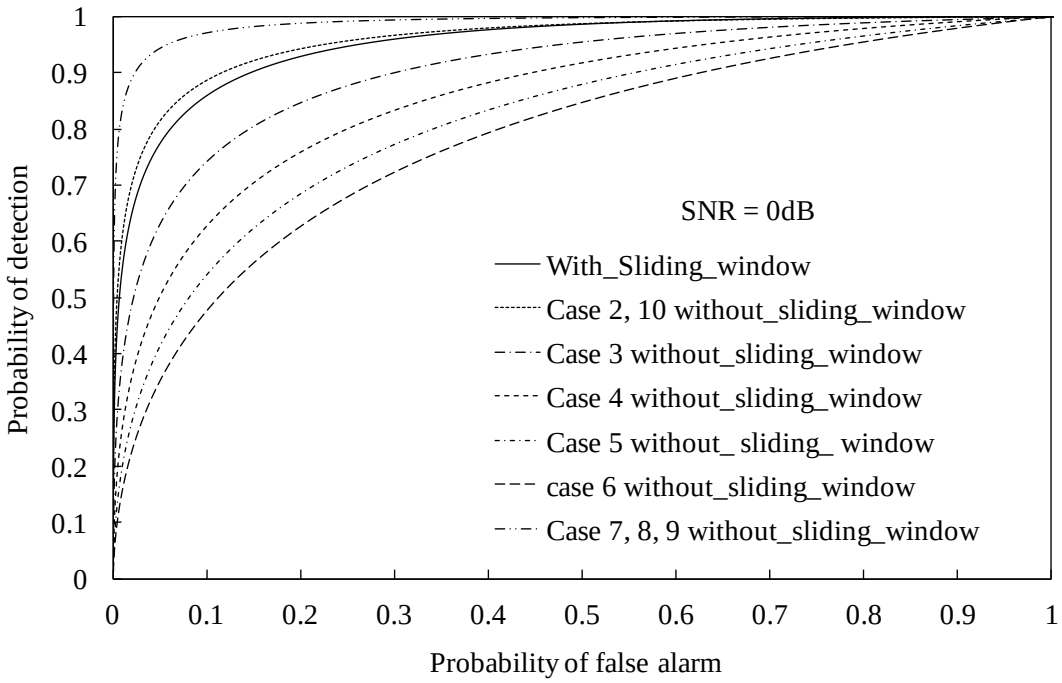

Figure 4.9 P_D vs P_{FA} for various target models.

Fig. 4.10 shows the detection probability versus the false alarm probability for stationary target model 3 at $\bar{E}/N_0$=0dB with sliding window (SW) size 2, 4, 6, 8, 10 and noncoherent integration number 8. The proposed detector with various sliding window size has different average signal energy for target model 3 depending on the sliding window size.

The result shows that the performance of the detector with sliding window size 6 is found to be better as the energy reflected from the target has average signal energy as 1. But the performance of the detector without sliding window is reduced as the target has average signal energy as 1/3 because the maximum flare point is only used.

We can predict that if the pulse width is not very narrow such as sub-nano second duration, then the energy is not more spread and the proposed detector with sliding window size 6 is superior due to the percentage of total energy reflected from each flare point, compared to sliding window size 2, 4, 8, and 10 when we consider the target model 3.

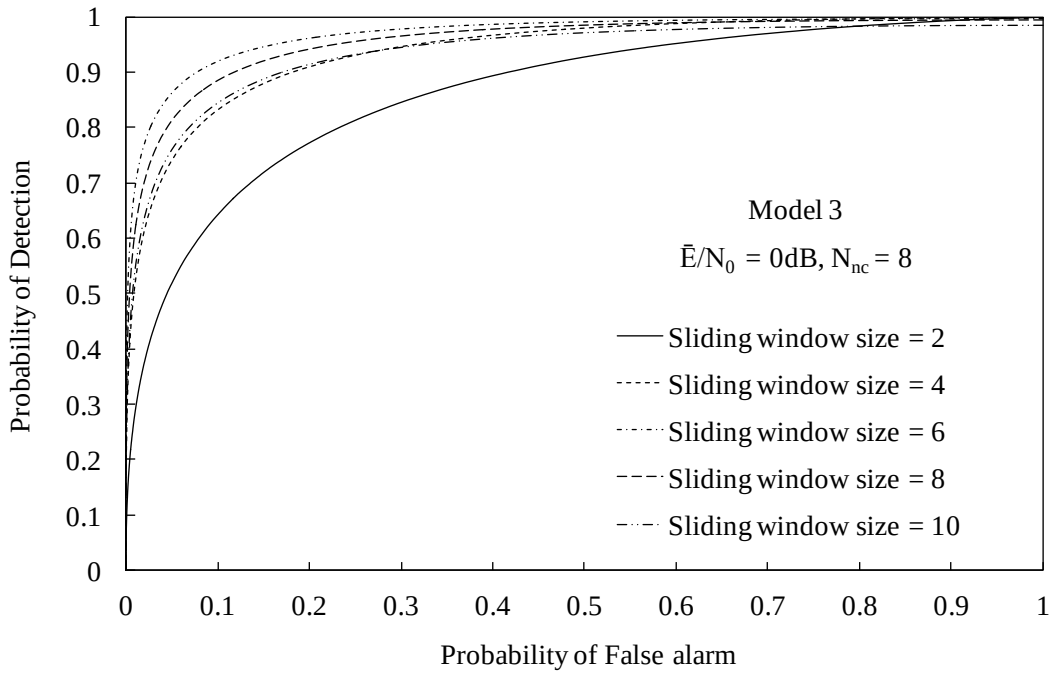

Figure 4.10 P_D vs P_{FA} for target model 3.

Fig. 4.11 shows the detection probability versus the false alarm probability for stationary target model 9 at $\bar{E}/N_0$=0dB with sliding window (SW) size 2, 4, 6, 8, 10 and noncoherent integration number (N_{nc}) 8. The proposed detector with various sliding window size has different average signal energy for target model 9 depending on the sliding window size. The result shows that the performance of the detector with Sliding window size 2 is found to be better as the energy reflected from the target has average signal energy as 3/4. But the performance of the detector without sliding window is reduced as the target has average signal energy as 3/4 because the maximum flare point is only used. The proposed detector with sliding window size 2 is superior due to the percentage of total energy reflected from each flare point, compared to sliding window size 4, 6, 8, and 10 when we consider the target model 9.

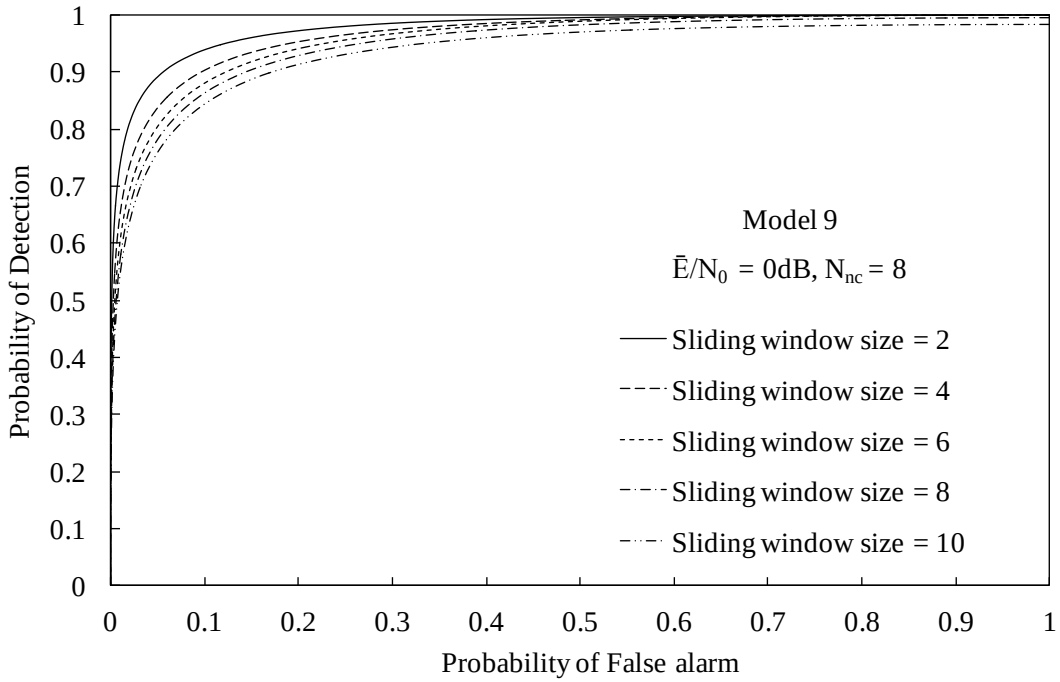

Figure 4.11 P_D vs P_{FA} for target model 9.

4.4.3 Detection Probability (P_D) vs $\bar{E}/N_0$

Fig. 4.12 shows the detection probability versus $\bar{E}/N_0$ for various stationary target models at P_{FA}=0.01. The proposed detector is superior to the detector without sliding window for model 3, 4, 5, and 6 which are distributed target model. However the detector without sliding window has better detection probability because the energy is concentrated on the main flare point. The proposed detector has better performance in comparison with the detector without sliding window (conventional non-coherent detector) when the energy reflected from the target is more distributed. Detection depends on the percentage of total energy reflected from each flare point of the target. If the pulse width is very narrow like UWB signal, then the energy is more spread and the proposed detector with sliding window is superior. Also in order to get the detection probability to be above 0.9 for P_{FA}= 0.01, $\bar{E}/N_0$ is required to be more than 2dB. Therefore it is necessary that the number of coherent integration must be increased.

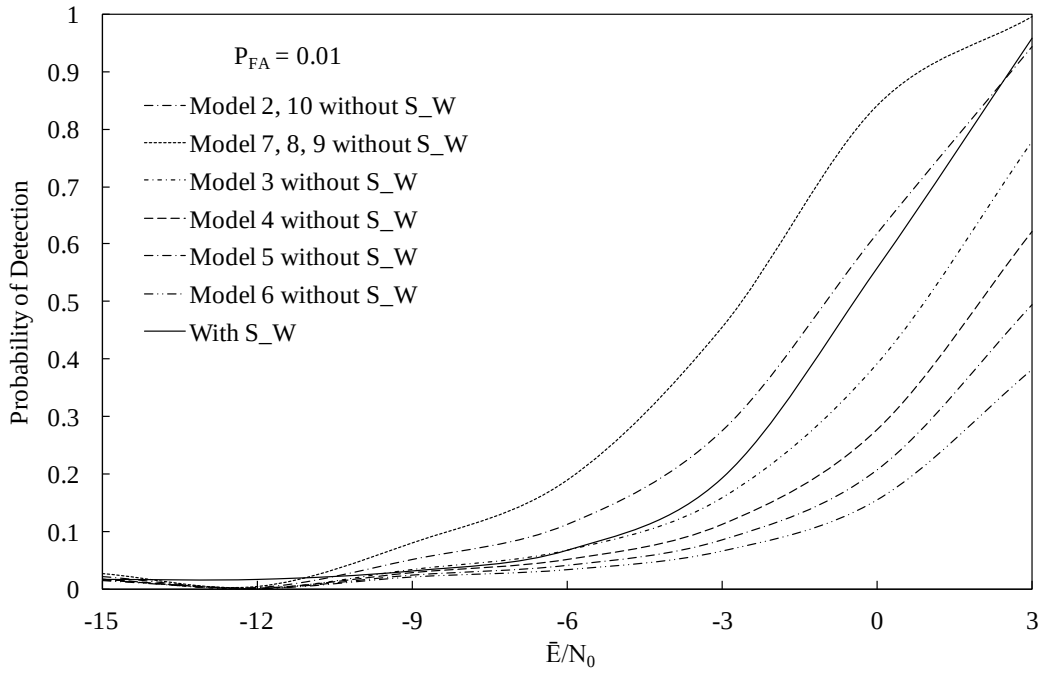

Figure 4.12 The detection probability vs. $\bar{E}/N_0$ for various target models at P_{FA}= 0.01.

4.5 P_D vs $\bar{E}/N_0$ in Gaussian noise environment for non-coherent detectors

Fig. 4.13 shows the detection probability versus $\bar{E}/N_0$ for stationary target at P_{FA}=0.01. The non-coherent detectors have detection probability of 1 at $\bar{E}/N_0$=3dB and the performance of all the three detectors is same. Fig. 4.14 – Fig. 4.16 shows the detection probability versus $\bar{E}/N_0$ for various stationary target at P_{FA}=0.01. The non-coherent detectors have better detection probability as the number of non-coherent integration increases. The simulation result shows that at $\bar{E}/N_0$=-6dB the probability of detection is approximately 1 for non-coherent integration number of 8 for all the detectors, On the other hand the probability of detection reduces by 0.2 when the number of non-coherent integration reduces to 4.We can also predict that the performance of all the detectors is almost same when we use the same number of non-coherent integration. Therefore we can use any of the three detectors for automobile applications.

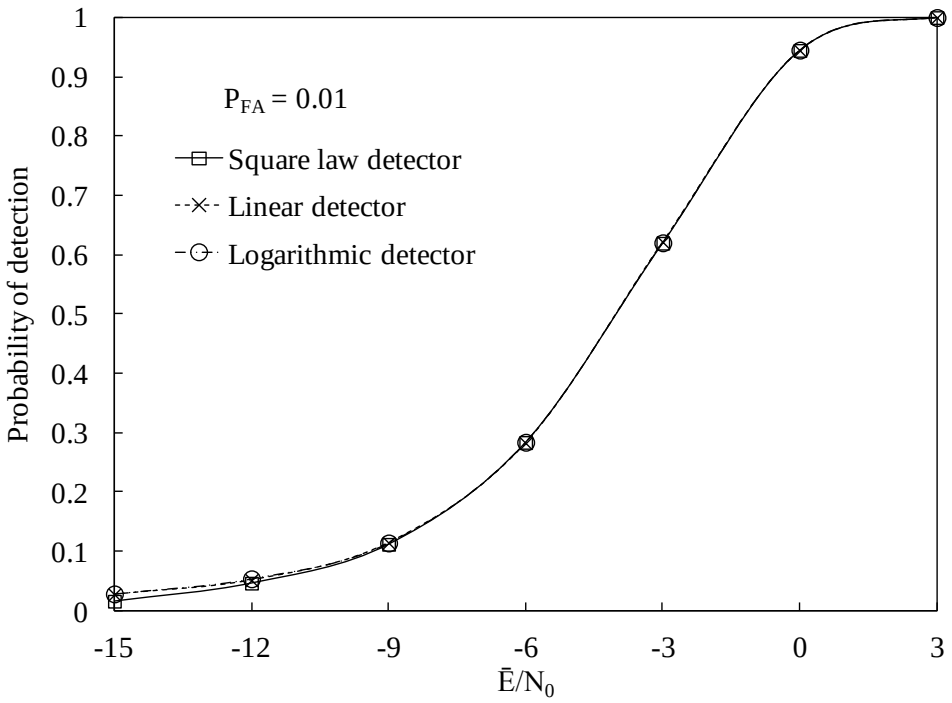

Figure 4.13 The detection probability vs. $\bar{E}/N_0$ for N_{nc} = 1.

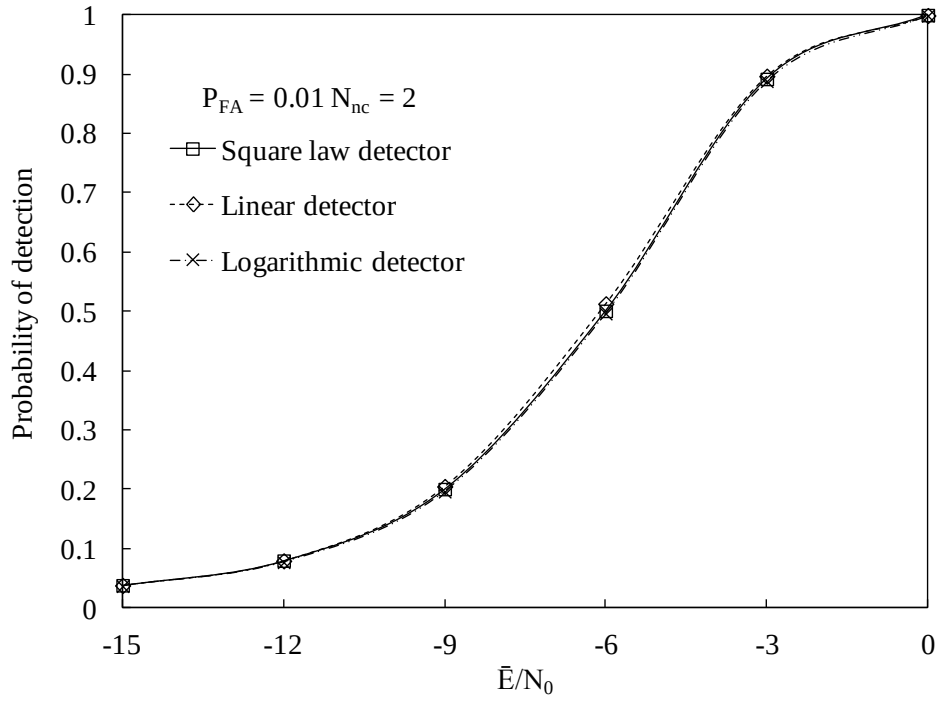

Figure 4.14 The detection probability vs. $\bar{E}/N_0$ for N_{nc} = 2.

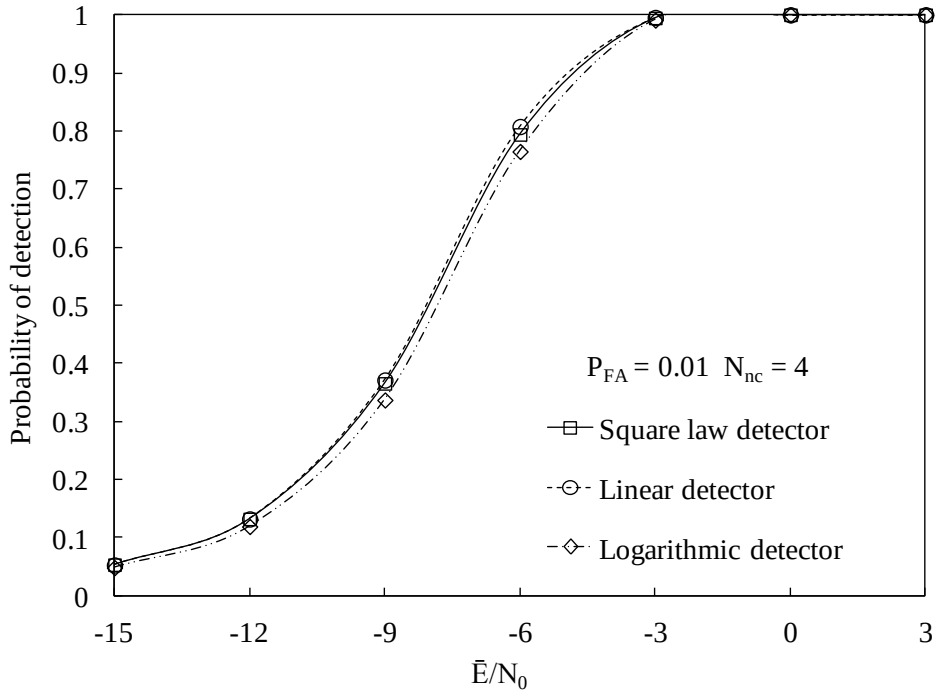

Figure 4.15 The detection probability vs. $\bar{E}/N_0$ for N_{nc} = 4.

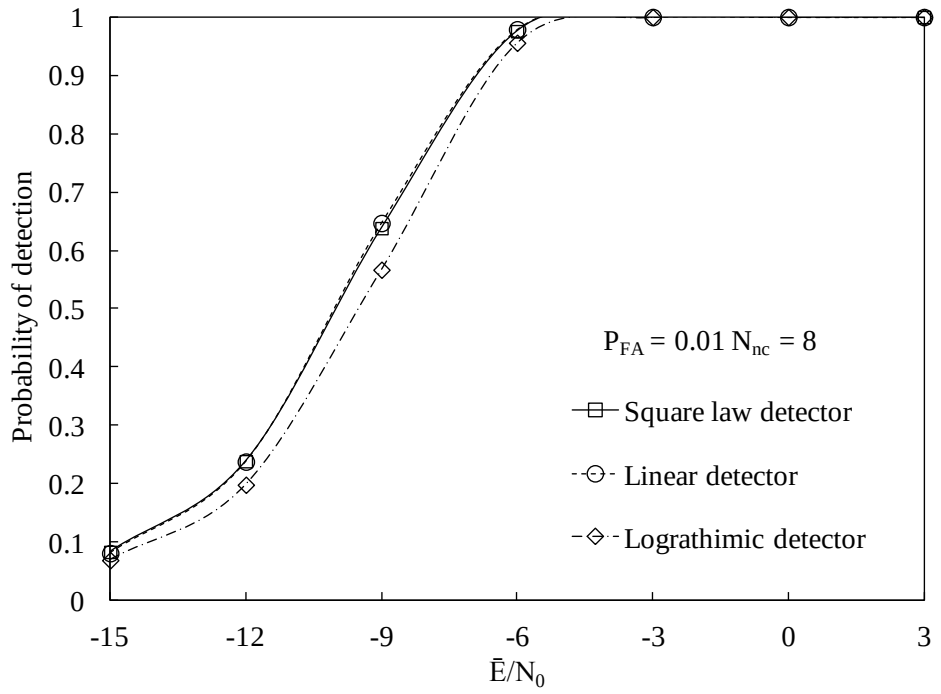

Figure 4.16 The detection probability vs. $\bar{E}/N_0$ for N_{nc} = 8.

4.6 Simulation result in Weibull Clutter environment for square law detector

4.6.1 Probability Density Function

The weibull distribution resembles the road clutter environment when the system bandwidth of more than 100MHz is used. The weibull distribution is used to analyze the performance of proposed detector in weibull clutter environment. A random variable ξ is said to have a weibull distribution if its probability density function has the following form

$$f(x)=\begin{cases}\dfrac{\alpha \ln 2}{x_m}(x/x_m)^{\alpha-1}e^{-\ln 2(x/x_m)^{\alpha}} & x \geq 0 \\ 0 & x<0\end{cases} \tag{4.82}$$

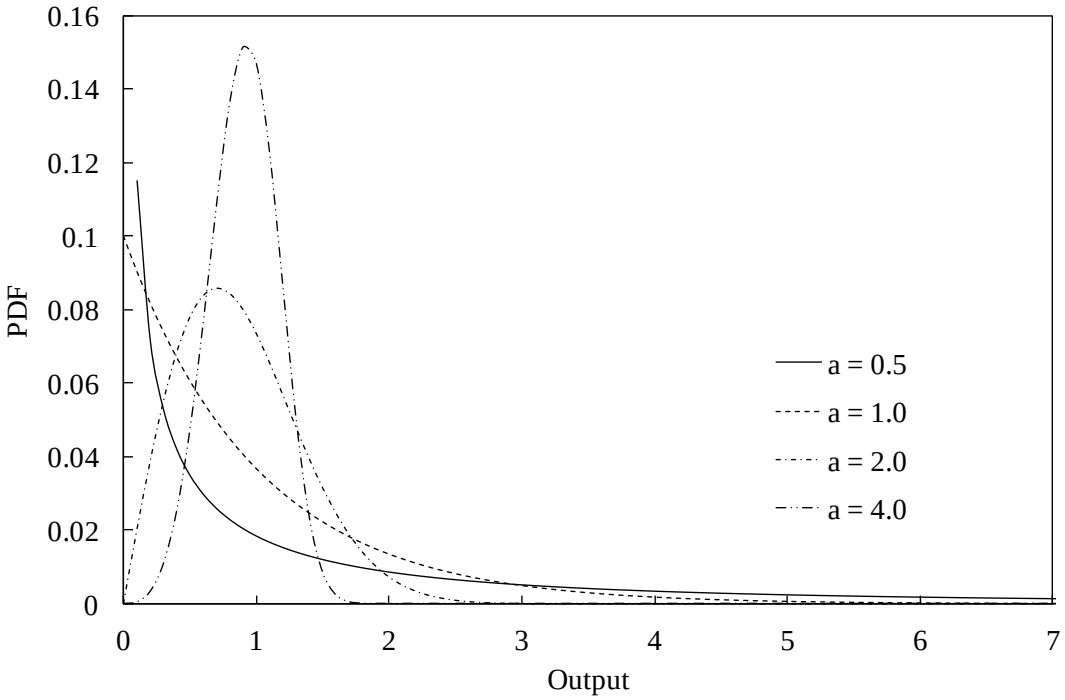

Figure 4.17 The probability density function of weibull clutter for various shape parameters.

4.6.2 Region of Convergence curve

The purpose of the simulation is to assess the detection performance of the non-coherent detector such as square law detector in uncorrelated weibull clutter environment. The various non-coherent detector parameters used in the simulation are as follows; the coherent integration number (N_c) and the non-coherent integration number (N_{nc}). The percentage of total energy reflected from a single target is assumed to be 1. The signal-to-clutter ratio (SCR) is defined as $\bar{E}/C_0$, where $\bar{E}$ represents the total average energy reflected from a target.

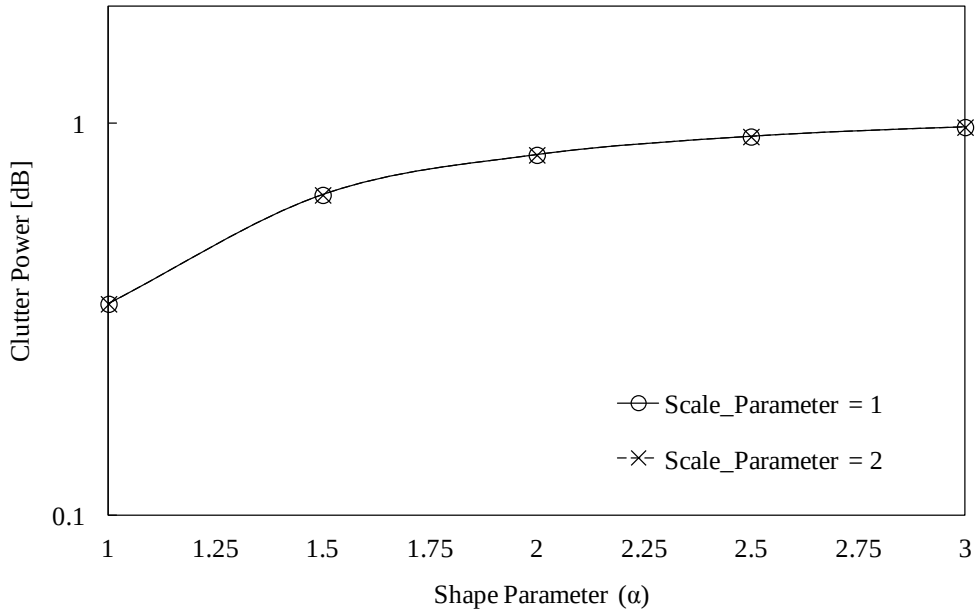

Figure 4.18 Weibull clutter power for various scale parameter.

The weibull distribution can be expressed as follows

$$p(x) = \frac{\alpha}{b}\left(\frac{x}{b}\right)^{\alpha-1} \exp\left[-\left(\frac{x}{b}\right)^{\alpha}\right], \tag{4.83}$$

Where b is the scale parameter ($b > 0$), α is the shape parameter ($\alpha > 0$) and x is the random variable of the weibull distribution. The clutter power (C_0) for weibull environment can be expressed as follows

$$C_0 = \frac{x_m^2 \Gamma(1+(2/\alpha))}{(\ln(2))^{2/\alpha}}, \tag{4.84}$$

where α is the shape parameter and indicates the degree of skewness, x_m is the median of weibull distribution [9]. From Fig. 4.18, we can predict that the clutter power is approximately 1 dB for shape parameter greater than 3. Also, we know that the weibull scale and shape parameter for 24 GHz automobile short range radar is 1.6 and 6.9 for traffic road clutter. Thus, we use the maximum scale and shape parameter value as 2 and 7 in the simulation. The detection performance of the proposed detector for various skewness and scale parameters is presented in Fig. 4.19. Integration of pulses is generally much less effective when detection is limited by clutter, since the clutter echo does not fluctuate from pulse to pulse so there is no much increase in signal-to-clutter ratio. Thus, integration of pulses will not be beneficial. Therefore, the maximum coherent integration number (N_c) of 10 is used. The non-coherent integration number (N_{nc}) is increased for various clutter power in order to obtain the maximum detection probability.

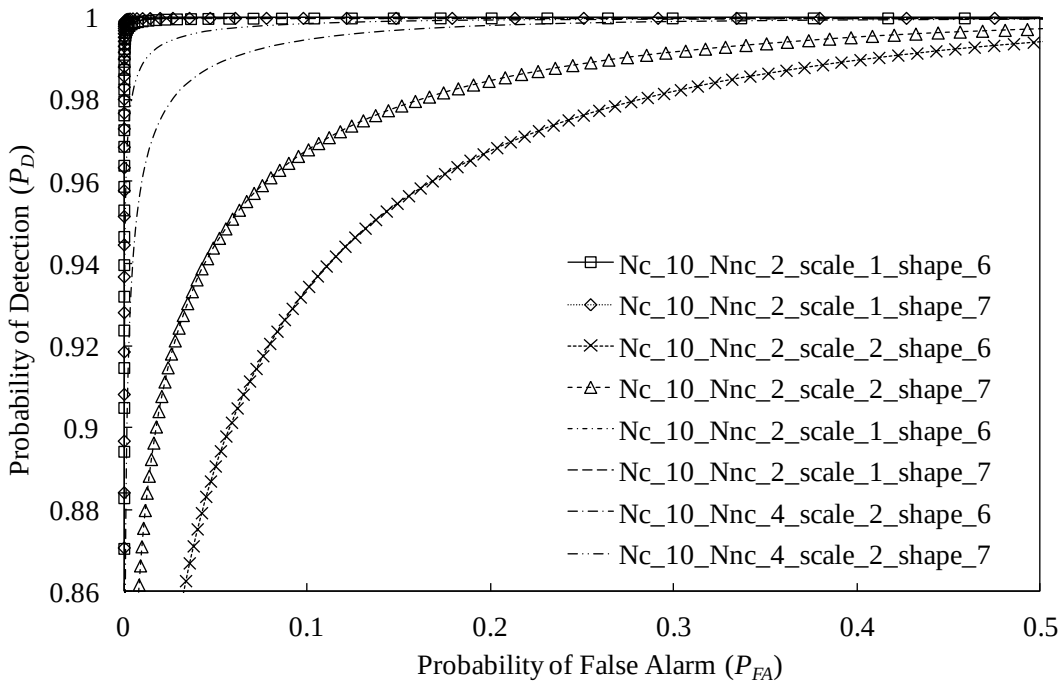

Figure 4.19 Region of convergence curve.

4.6.3 Detection Probability Vs Shape Parameter

Fig. 4.20 shows the detection probability versus weibull skewness parameter for various scale parameters at P_{FA} = 0.01. The proposed detector has better detection probability as the number of non-coherent integration increases. The simulation result shows that the probability of detection is approximately 1 for non-coherent integration number (N_{nc}) of 8.

On the other hand the probability of detection reduces by 0.2 when the number of non-coherent integration reduces to 2. Also, we can predict that the probability of detection is almost 1 for skewness (α) and scale parameter (b) greater than 4 and 2. Thus, in this section the coherent and non-coherent integration number of 10 and 8 is optimized for weibull clutter environment in automobile applications, and we get the maximum detection probability of more than 0.9 for the optimized parameters.

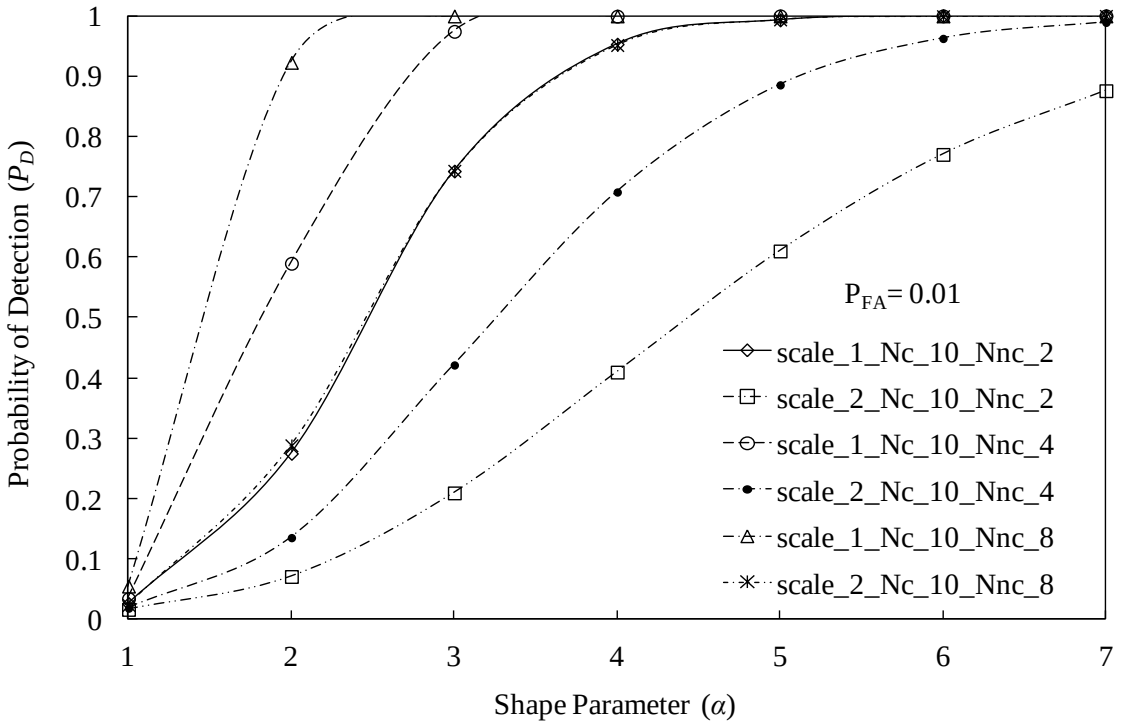

Figure 4.20 Probability of detection vs shape parameter.

5. Moving Target

5.1 System Description

In this sub-chapter, we consider the moving target and assume that the reflected signal has only one echo signal. Therefore we can rewrite the equation (4.66) as follows

$$r(t) = A_T \cdot \alpha \cdot e^{j\theta} \sum_{n=-\infty}^{+\infty} p(t - nT_{PRI} - \tau) \tag{5.1}$$

where we ignore the noise term in order to simplify the equation [7].

A target within the sensors field of view is located at range r_0 and moves at time of measurement with a nearly constant velocity v during the measurement interval. The range is

$$r(t) = r_0 + v \cdot t. \tag{5.2}$$

From equation (5.1), after a propagation time of $2 \cdot r(t)/c$, the received signal can be described as follows

$$r(t) = A_E \cdot \exp\left(-\frac{4\pi f_c v}{c} t + \underbrace{\theta - \frac{4\pi f_c r_0}{c} + \varphi_0}_{\varphi_I} \right) \cdot \sum_{n=-\infty}^{+\infty} p\left(t - nT_{PRI} - \frac{2 \cdot r(t)}{c} \right) \tag{5.3}$$

where

$A_E$is the amplitude of the received signal and can be $A_E.\alpha$

φ_I is the phase of the received signal

f_D is the Doppler frequency of the signal and can be $-2vf_c/c$

If only a single pulse at n=0 is considered, the baseband received signal can be

$$r(t) = A_E \cdot \exp(2\pi f_D t + \varphi_I) \cdot p\left[t - \frac{2 \cdot r(t)}{c} \right] \tag{5.4}$$

where

$$I_{input} = A_E \cdot \cos(2\pi f_D t + \varphi_I) \cdot p\left[t - \frac{2 \cdot r(t)}{c} \right] \tag{5.5}$$

$$Q_{input} = A_E \cdot \sin(2\pi f_D t + \varphi_I) \cdot p\left[t - \frac{2.r(t)}{c} \right] \tag{5.6}$$

5.2 Conventional Detection Algorithm for Velocity measure

This chapter provides a description of standard pulse Doppler radar system architecture with emphasis on the detection and their relationship to other radar system processes. A common MTI radar design, utilizing coherent processing and digital Doppler frequency determination, is illustrated in Fig. 5.1. The system consists of an antenna, duplexer, and two channels: a transmitting and a receiving channel. This architecture is the most popular receiver structure for systems performing range and velocity determination. The use of digital filter banks in the receiver structure is a recent but widespread addition to radar system architecture resulting from advances in micro-computer technology that has allowed for the implementation of high-speed digital Discrete Fourier Transform (DFT) algorithms. Early generation receivers tended to use the architecture illustrated in Fig. 5.4 where frequency discrimination was provided by a fixed set of analog filters.

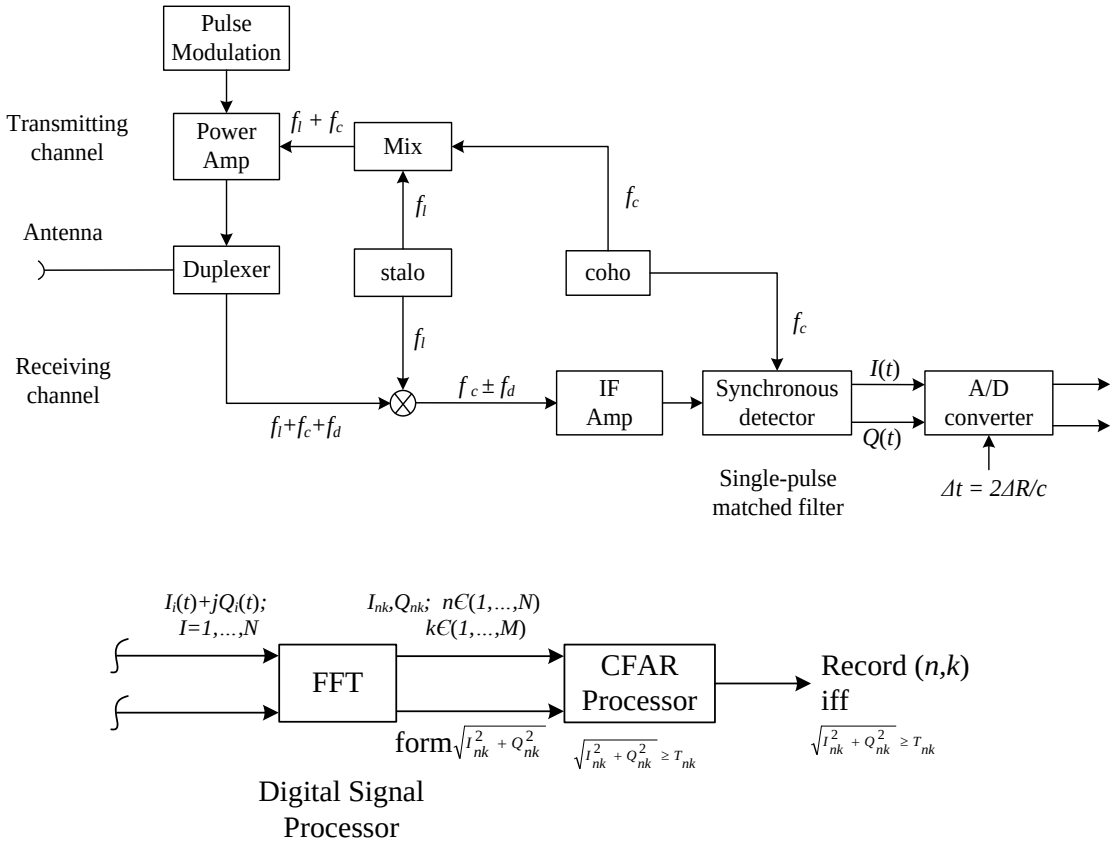

Figure 5.1 Pulse Doppler radar system architecture.

Analog filters banks are less flexible than digital filters; and, while digital filters operate on entire coherent pulse-trains, analog filters are suited more for single-pulse or noncoherent pulse-train reception. Because of the widespread and increasing use of digital filter techniques, the focus of this chapter is on the architecture and performance of those systems performing digital frequency discrimination, as illustrated in Fig. 5.1 However, some differences between the analog and digital filter structures are outlined and discussed.

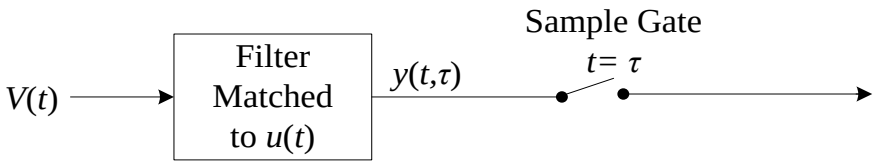

Figure 5.2 Matched Filter receiver.

Suppose that $v(t)$ is an arbitrary time-domain function input to a linear time-invariant filter, as illustrated in Fig. 5.2. Further, suppose that $u(t)$ is a time domain function taking non-zero values only on the interval $[0,\tau]$; and that the time-invariant filter is matched to $u(t)$. Then, the matched filter impulse response function $h(t)$ has the form

$$h(t)=\begin{cases} ku(\tau-t) & 0\le t\le \tau \\ 0 & \text{otherwise} \end{cases} \tag{5.7}$$

And, the input-output relationship of the matched filter can be described by,

$$\begin{aligned} y(t,\tau) &= \int_{-\infty}^{\infty} h(s)v(t-s)ds \\ &= k\int_{0}^{\tau} u(\tau-s)v(t-s)ds \end{aligned} \tag{5.8}$$

Let $x=\tau-s$, then

$$y(t,\tau)=k\int_{0}^{\tau} u(x)v(t-\tau+x)dx \tag{5.9}$$

Therefore, the output of the matched filter sampled at time $t=\tau$ is

$$y(\tau,\tau)=k\int_{0}^{\tau} u(x)v(x)dx \equiv I(\tau) \tag{5.10}$$

$I(\tau)$ is an important structure of modern receiver design, and is used in the development of detection statistics for most detection strategies.

In digital pulse Doppler, coherent processing, radar systems, a complex discrete Fourier transform (DFT) is performed on sets of samples from each range bin. DFT real outputs at each range bin are outputs for a set of filters approximately matched to waveforms $u_I(t)=a(t)\cos(\omega_k t)$ for $\omega_k=kPRF/N$, $k=0,\ldots,N-1$; and DFT imaginary outputs at each range bin are outputs from a set of filters approximately matched to waveforms $u_Q(t)=a(t)\cos(\omega_k t)$ for same values of ω_k.

Let $a(t)$ be a range-gating function identical to the gating function of the transmitted waveform. As illustrated in Fig. 5.3. τ is the pulse width of each individual pulse in the coherent pulse train, and T is the pulse repetition interval.

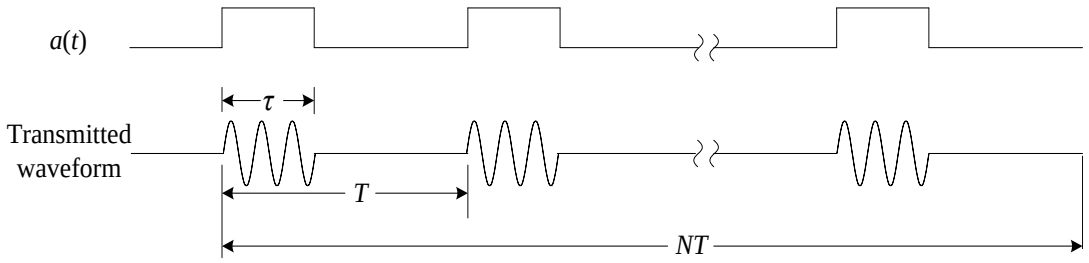

Figure 5.3 The sample gating function.

When an observation $v(t)$ is input to a range-gate sampling function and the output of the sampling function is passed to a DFT, then the DFT output at each frequency point k, is by definition,

$$G(\omega_k)=\frac{T}{2\pi}\sum_{n=0}^{N-1}v(nT)a(nT)e^{-j\omega_k nT} \qquad k=0,\ldots,N-1 \tag{5.11}$$

The discrete form of the Fourier transform is approximately equal to the continuous form; i.e,

$$\begin{aligned} G(\omega_k) &\approx \frac{1}{2\pi}\int_0^{NT} v(t)a(t)e^{-j\omega_k t}dt \\ &= \frac{1}{2\pi}\int_0^{NT} v(t)a(t)\cos(\omega_k t)dt - j\frac{1}{2\pi}\int_0^{NT} v(t)a(t)\sin(\omega_k t)dt \\ &= \frac{1}{2\pi}\int_0^{NT} v(t)u_I(t)dt - j\frac{1}{2\pi}\int_0^{NT} v(t)u_Q(t)dt \end{aligned} \tag{5.12}$$

Then, by the previous discussion, the real part of $G(\omega_k)$ is approximately the output of a filter matched to $u_I(t)$ sampled at time NT; and the imaginary part of $G(\omega_k)$ is approximately the output of a filter matched to $u_Q(t)$ sampled at time NT.

To perform target detection, the conventional radar system transmits a series of N pulses; each having an IF modulated RF carrier frequency. The pulse width (τ), inter pulse period (T), and transmission duty cycle (τ/T) are constant throughout the transmission of all N pulses. The inter-pulse period is called the pulse repetition interval (*PRI*) and is the inverse of the pulse repetition frequency (*PRF*). The N transmitted pulses are coherent; that is, pulses in the train are in-phase, as if formed from gated oscillator.

An A/D converter is synchronized so that M samples are gathered following each transmitted pulse in a CPI. Each sample represents the results obtained from one of M range bins: R_i = 1, 2, 3,…,M. Each range bin may contain energy from targets at one or more distinct ranges, depending on the range ambiguity. Medium or high PRF radar systems are range ambiguous.

The reflected-signal frequency spectrum is evaluated for each range cell, in each CPI, by performing a DFT on samples taken following each pulse. One DFT is formed for each range cell in each CPI. Typically, DFTs are performed with Fast Fourier Transform (FFT) algorithms. A 16 or 32 point DFT is used, and the number of coherent pulses in each pulse-train is approximately 16 or 32. The number of coherent pulses in a pulse-train is selected to provide the transmitted energy needed to achieve a specified maximum detection range, according to the radar range equation, and will generally not be equal to the number of frequency points in the DFT. Differences between the number of coherent pulses in the pulse-train and the exact number of DFT frequency points are resolved by either wrapping or zero filling incoming data prior to the DFT process. This difference causes a filter mismatch with respect to the received signal which results in a *S/N* loss that must be accounted for in the overall *S/N* loss budget. The DFT as a filter matched to receive signal is discussed. Each returning pulse train, reflected from an external object with non-zero radial velocity, will have its transmission frequency shifted by the reflecting object (the Doppler frequency). The

radar system front-end hardware, prior to the A/D conversion, removes the IF and RF components from incoming signals leaving only the residual Doppler frequencies to be sampled and passed to the signal processor. Then, the DFT filter bank formed for a range cell provides a direct measure of the Doppler frequency energy at the range represented by the range cell.

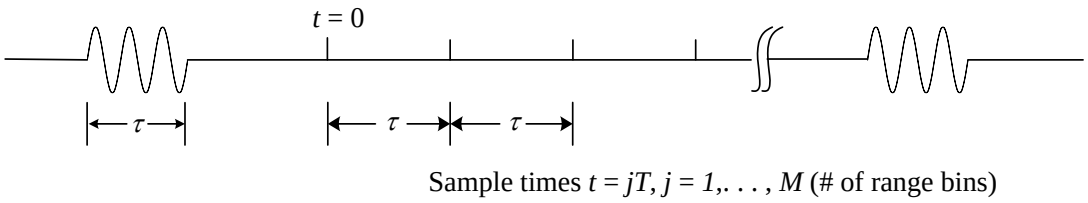

Figure 5.4 Coherent pulse trains.

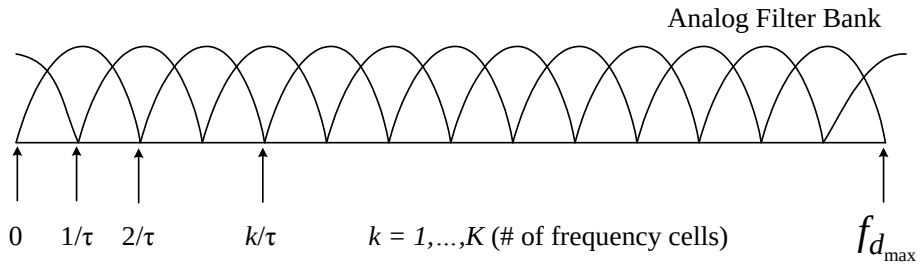

Figure 5.5 Fourier transform of *N* coherent pulses.

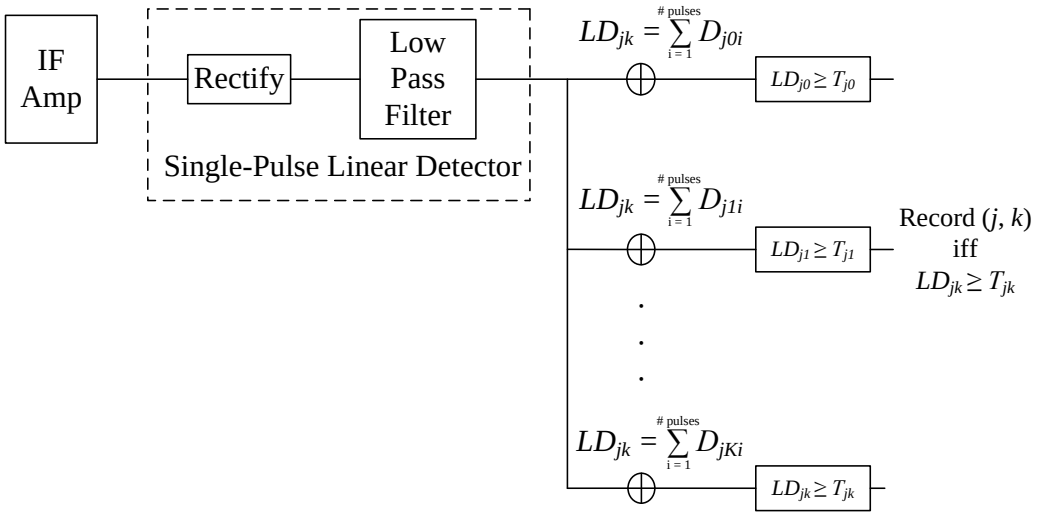

Figure 5.6 Analog filter bank with multiple pulse linear detection.

Each DFT frequency cell may contain energy from reflections at one or more distinct Doppler frequencies, depending on the frequency ambiguity of the system. Low and medium PRF radar systems are ambiguous in frequency. Usually, frequency ambiguities are resolved by applying post-detection algorithms to the result of three or more CPIs at the resolution angle.

Detection statistics (such as square law detection statistic $\sqrt{I_{nk}^2 + Q_{nk}^2}$ included in Fig. 5.1 are formed from DFT outputs according to the prescribed detection strategy, then passed to the CFAR process where they are compared against thresholds developed to provide detection algorithm while maintaining a relatively constant false alarm rate in the presence of low-level clutter variation and noise interference.

5.3 Proposed Detection Algorithm for velocity measure

5.3.1 Time and Memory efficient detector

In this section, we propose a new detection algorithm for measuring the range and relative velocity of the target. We first detect the range of the target and then measure the relative velocity at the decided range index by using FFT. The proposed detector consists of coherent integrator, non coherent integrator, decision block, and velocity calculator block as shown in Fig. 5.7. The coherent and non-coherent range gate's memory size (K) is less than the maximum range (i.e., $R_{max}/\Delta R$) and indicates the maximum target range to be tested.

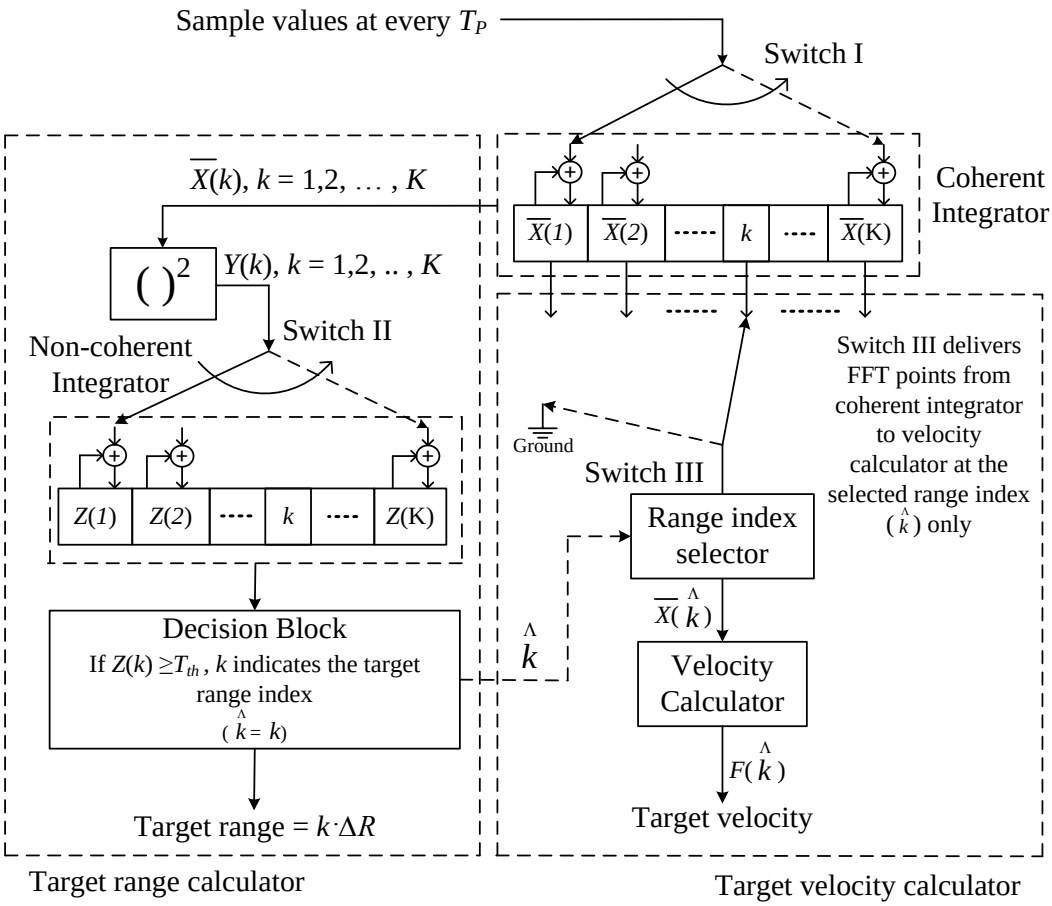

Figure 5.7 Detector to measure velocity.

In the ADC of Fig. 4.3, the sampling frequency is same to the pulse width (T_p), because the range resolution (ΔR) required for our application (i.e., stop-and-go or short range cruise control functionality) is between 0.2-0.5m as mentioned in [19]. Therefore, the switch I in Fig. 5.7 is shifted at every (T_P) for each sampled values of the in-phase (I) and quadrature (Q) channel during one T_{PRI} sequentially. At every T_{PRI}, we use the samples only

as much as the range gate's memory size (K). As shown in Fig. 5.8, the coherent integrator integrates the sample values at each range gate during $N_c \cdot T_{PRI}$ (where N_c is the number of coherent integration) and delivers to the non-coherent integrator i.e., the coherently integrated values for each range gate is given as ($\overline{X}$ (k), k =1, 2,..., K). Therefore, we can simultaneously get the coherently integrated values for all range gates. Similarly, the non-coherent integrator is also operated for all range gates at every $N_{nc} \cdot N_c \cdot T_{PRI}$ (where N_{nc} is the number of non-coherent integration). However, if the non-coherent integration number is increased, the processing time of proposed detector is also increased. Therefore, we have to choose appropriate non-coherent integration number (N_{nc}). The description about the processing time of proposed detector is more elaborated in subsection 5.4 of this dissertation. In the decision block, the range gates are compared with the threshold. And if it is greater than the defined threshold, then we can decide that the target is present. The decided range gate index (k) indicates the round trip delay from the target that is same to the distance. When the target is present, $\hat{k} = k$. Finally, the velocity calculator will receive each FFT point at every $N_c \cdot T_{PRI}$ from coherent integrator block through switch III at the decided target range index ($\hat{k}$) to determine the target velocity (i.e., the switch III will select only the decided range index ($\hat{k}$) for velocity calculator block).

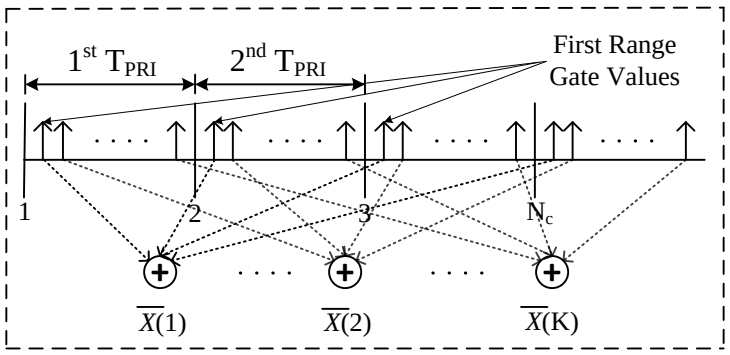

Figure 5.8 Coherent integration process.

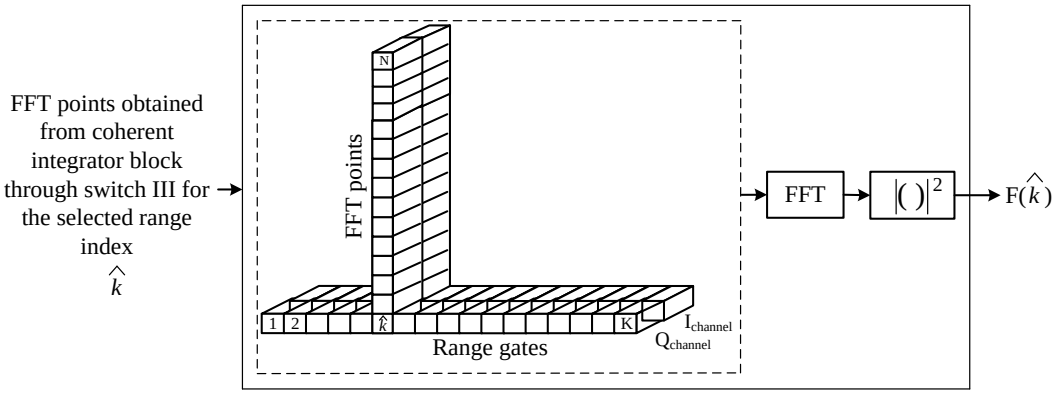

Figure 5.9 Velocity calculator.

The coherent integration for the *k*-th range rage in the proposed detector can be expressed as follows

$$\bar{X}(k) = X^I(k) + X^Q(k) = \frac{1}{N_c}\sum_{n=1}^{N_c} \bar{r}_n(k) \quad k = 1,2,...,K, \tag{5.13}$$

where N_c is the coherent integration number and from (3.63) the received *k*-th sample value at *n*-th T_{PRI} (i.e., $t = nT_{PRI} + kT_p$) is

$$\bar{r}_n(kT_P) = A_T \alpha \cdot e^{j\{\omega_d(nT_{PRI}+kT_P)-\theta\}} p(kT_P - \tau) + \bar{N}(nT_{PRI} + kT_P) \tag{5.14}$$

$$\bar{r}_n(kT_P) = A_T \alpha \cdot e^{j\omega_d(nT_{PRI}+kT_P)+\theta} + \bar{N}(nT_{PRI} + kT_P) \tag{5.15}$$

where $p\ (kT_p\text{-}\tau) = p\ (0) = 1$from Eq. (3.64) on condition that the round trip delay τ is the same as kT_P*;* if the synchronization is perfectly satisfied, these conditions are met. And $\bar{N}$ $(nT_{PRI}+kT_P)$ is a sampled value of $\bar{N}\ (t)$ at $t = nT_{PRI}+kT_P$.

After coherent integration and squaring the output can be represented as

$$Y(k) = \left|\bar{X}(k)\right|^2, \quad k = 1,2,...,K. \tag{5.16}$$

The value $Y(k)$, is stored in each memory of the non-coherent integrator and the output of non-coherent integration , $Z(k)$, can be written as

$$Z(k) = \frac{1}{N_{nc}}\sum_{m=1}^{N_{nc}} Y_m(k), \ \mathrm{k} = 1,2,..., \mathrm{K}, \tag{5.17}$$

where N_{nc} is the number of non-coherent integration. If the above result is greater than the defined threshold, then we can determine that a target is present. Therefore we can express as follows

$$H_1 : Z(k) \geq T_{th}$$
$$H_0 : Z(k) < T_{th}. \tag{5.18}$$

In this case of H_1 hypothesis, the index k represents the target range gate, $k \cdot \Delta R$ indicates the target range. Therefore $\hat{k}$ is equal to k, only when $Z(k) \geq T_{th}$ (for example, if $Z(10) \geq T_{th}$ then the range index $\hat{k} \geq 10$ is only given to range index selector block). The switch III in Fig. 4 7 delivers the FFT points from coherent integrator block to velocity calculator block at the selected range index ($\hat{k}$) only. The datas $\overline{X}(\hat{k})$ are the FFT points respectively (i.e., if N =32 then 32 FFT points of $X(k)$ are only delivered to velocity calculator through switch III as shown in Fig. 5.9. Thus, the output of the velocity calculator can be expressed as

$$F(k) = \left| \frac{1}{N} \sum_{l=1}^{N} X_l^I(\hat{k}) e^{-j\omega l} \right|^2 + \left| \frac{1}{N} \sum_{l=1}^{N} X_l^Q(\hat{k}) e^{-j\omega l} \right|^2 \quad k = 1,2,\ldots,K, \tag{5.19}$$

The value $F(\hat{k})$ is the output of the velocity calculator for the selected range index ($\hat{k}$) only. Therefore, the FFT processing time and memory requirement for the proposed method is reduced which is analyzed and presented in later section of this dissertation.

Table 5.1 System parameters for Moving target.

Parameter	Notation	Values	
		Proposed Detector	**Conventional Detector**
Pulse Repetition Interval	T_{PRI}	100ns	100ns
Pulse Width	T_P	2ns	2ns
Maximum Target Range	R_{max}	15m	15m
Range Resolution	ΔR	30cm	30cm
Number of Coherent integration	N_c	400	400
Number of Non-coherent integration	N_{nc}	4	
Velocity resolution	Δv	8.7 Km/hr	17.4 Km/hr
Number of FFT points	N	64	32

Algorithm for proposed detector

STEP 1: Declare the sampling frequency, input SNR.

STEP 2: Declare the total energy reflected from a single moving target as 1 and the UWB detector parameters as mentioned in table 5.1.

STEP 3: Declare the Doppler frequency (f_D) with the target model.

STEP 4: Create the XL file to print the FFT output and detector output separately.

STEP 5: Using malloc initialize the two dimensional arrays for storing the FFT output.

STEP 6 Generate the Gaussian noise using the Gaussian noise function.

STEP 7: Add the Gaussian noise with the received signal along with Doppler frequency in both I and Q channel.

STEP 8: First coherent integration is implemented for the received time domain signal and then non-coherent integration is implemented.

STEP 9: Repeat step 8 for all range gates.

STEP 10: The FFT is implemented for the decided range index by using FFT function.

STEP 11: The detector output is printed in XL file.

STEP 12: File is closed and dynamic memory is free.

STEP 13: end.

5.3.2 Sliding Window detector

The proposed detector consists of a coherent integrator, a sliding window, and a FFT block, as shown in Fig. 5.10. The coherent range gate memory size (K) is less than the maximum range and indicates the total size of the target range to be tested. In the ADC shown in Fig. 4.3, the sampling frequency is the same as the pulse width (T_P). Thus each sampled value of the in-phase (I) and quadrature (Q) channels are shifted at every T_P during one T_{PRI}. At every T_{PRI}, we use samples only as much as the range gate's memory size (K). As can be seen in Fig. 2, the coherent integrator integrates the sample values at each range gate during $N_c \cdot T_{PRI}$ (where N_c is the number of coherent integrations). Therefore, we can simultaneously obtain coherently integrated values ($\bar{X}(k)$, k=1,2,...,K) for all range gates. The coherently integrated sample values are delivered to the sliding window block. The M size sliding window samples are combined and then delivered to the FFT block sequentially. The FFT block operates for each range bin at every $N \cdot N_c \cdot M \cdot T_{PRI}$ and then dumps in a memory of range gates and FFT points (where N is the number of FFT points and M is the sliding window size). The complex outputs of the FFT block are squared, summed, and delivered to the k-th memory as ($Z(k)$, k=1,2,...,K). The coherent integration for the k-th range gate in the I_{input} and Q_{input} branch can be expressed as follows

$$\bar{X}(k) = X^I(k) + X^Q(k) = \frac{1}{N_c}\sum_{n=1}^{N_c} \bar{r}_n(k), k = 1,2,\ldots,K, \tag{5.20}$$

where N_c is the coherent integration number and, from (1), the received k-th sample value at n-th T_{PRI} (i.e., t=nT_{PRI}+kT_P) is

$$\bar{r}_n(kT_P) = A_T \sum_{l=0}^{L-1} \alpha_l \cdot e^{j\{\omega_d(nT_{PRI}+kT_P)+\theta_l\}} + \bar{N}_n(kT_P), \tag{5.21}$$

where the round trip delay τ_l is same as kT_p because $p(kT_p$-$\tau_l)$=$p(0)$=1. And, $\bar{N}_n(kT_P)$ is a sampled value of $\bar{N}(t)$ at t=nT_{PRI}+kT_p. The sliding window is operated for every M range gate, and then delivers the result to FFT block. The FFT block delivers a complex output, which is squared and combined. The output $Z(k)$ can be expressed as

$$Z(k) = \left| \frac{1}{N} \sum_{l=1}^{N} \sum_{m=1}^{M} \bar{X}_l(k+m) W_N^{lk} \right|^2, \tag{5.22}$$

where $W_N^{lk} = e^{-j(2\pi/N)lk}$, N is the number of FFT points, M is the sliding window size, the value $Z(k)$ is stored in the k-th memory. If the above result is greater than the defined threshold, then we can determine that a target is present. Therefore, we can write the results as follows

$$H_1 : Z(k) \geq T_{th};\ H_0 : Z(k) < T_{th}. \tag{5.23}$$

In the case of an H_1 hypothesis, the index k represents the target range gate, and $k \cdot \Delta R$ indicates the target range. It is well known that a non-coherent detector has non-central chi-square distribution $p_1(z)$, and central chi-square distribution $p_0(z)$ with 2 degrees of freedom for H_1 and H_0 hypothesis, respectively.

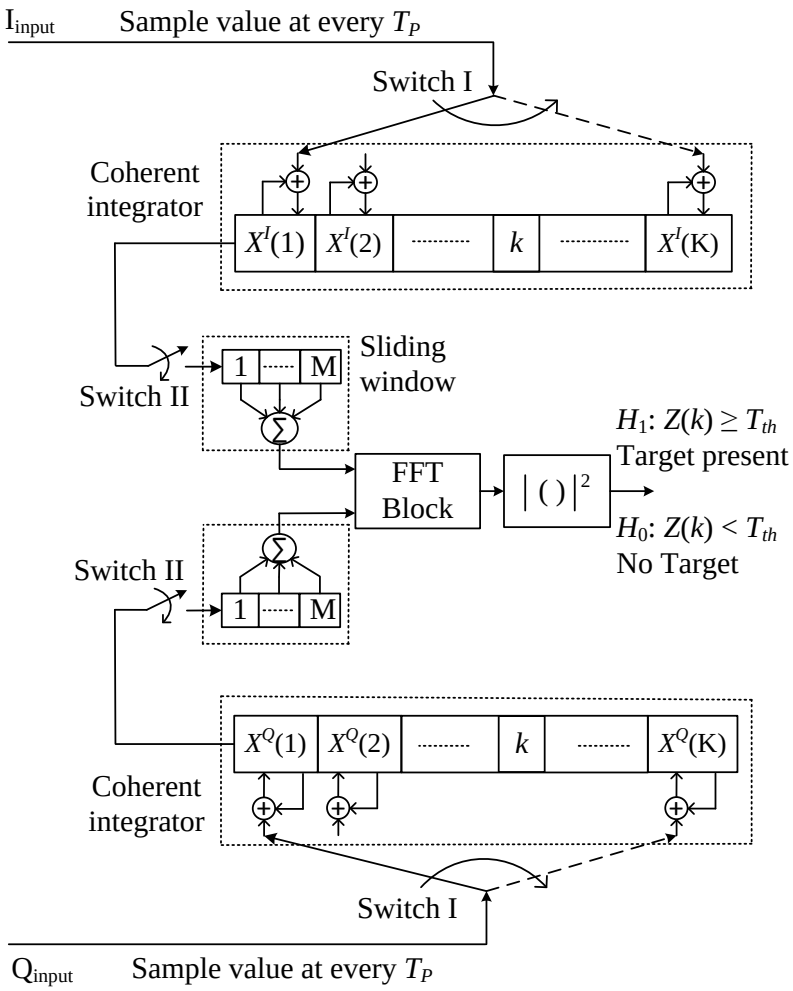

Figure 5.10 Sliding window detector.

5.4 Simulation result in Gaussian noise for time and memory efficient detector

In this section, we present the computer simulation results to assess the detection performance, time and memory efficiency of the proposed detector. First, the pulse width (T_P) and pulse repetition interval (T_{PRI}) are decided based on range resolution (ΔR) and maximum target range (R_{max}) for the required application [12]. In this work, we use pulse width of 2ns, because the range resolution required for our application (i.e., stop-and-go or short range cruise control functionality) is between 0.2-0.5 m as mentioned in [12]. Thus, we use the sampling frequency same to pulse width (T_P). Secondly, the system parameters such as the number of coherent integration and non-coherent integration are selected. Subsequently, the relative velocity resolution limitation is analyzed and number of FFT points is selected. Then the detection probability is evaluated. Finally, the measurement time and memory requirement is estimated. In the simulation, the total energy reflected from a single moving target is assumed as 1 and the selected parameters for proposed system is used as mentioned in Table 5.1. The proposed system and selected parameters is utilizable for single moving target case and not for multiple target case. The signal-to-noise ratio (SNR) is defined as $\bar{E}/N_0$, where $\bar{E}$ is the total average energy reflected from a single moving target.

5.4.1 Coherent and Non-coherent Integration

An important characteristic of the coherent integrator is that its effective bandwidth decreases as the integration time increases. Integration improves P_d and reduces P_{FA} by reducing the noise variance [38]. The quality of the signal detection can be improved by increasing the signal-to-noise ratio ($\bar{E}/N_0$), this can be achieved by using coherent integration. However, the coherent integration length is limited due to the relative velocity. The relation between the coherent integration length (N_c) and the relative velocity (v) can be expressed by the normalized signal mean power at the output of the coherent integrator without noise. When the Doppler frequency is large, the degradation of signal mean power vanishes in the form of *sinc* function (i.e., $D(f_d) = [sinc\ (\pi f_d T_{PRI} N_c)]^2$) as shown in Fig. 5.10 & 5.11 depending on the maximum target range [41]. Thus, the signal mean power is reduced slowly for target velocity of about 120 km/hr at the coherent integration length of more than 400 for maximum target range of 15m [41]. Therefore, the gain at the output of coherent integrator is decreased slowly for coherent integration length greater than 400 when the target velocity is greater than 120 km/hr and maximum target range of 15m.

The coherent integration number also depends on the selected FFT point as mentioned in later subsection of this dissertation. Therefore, the coherent integration number of 400 is used in simulation. The non-coherent integration number (N_{nc}) for the proposed detector is selected by using the detection probability (P_D) of the target range calculator. From Fig. 5.14, we can observe that as the input SNR decreases, the non-coherent integration number must be increased in order to achieve detection probability of almost 1 for false alarm probability of 0.001 [12]. However, if the non-coherent integration number (N_{nc}) is increased, we can predict that the processing time (i.e., $N_{nc} \cdot N_c \cdot T_{PRI}$) and hardware complexity of proposed detector are also increased as shown in Fig. 5.15 [15]. Therefore, we have to choose appropriate non-coherent integration number (N_{nc}). Thus, we use non-coherent integration number of 4 for the proposed detector in simulation so that we are able to achieve detection probability more than 0.9 when the input SNR is -18 dB for maximum target velocity of up to 150 km/hr.

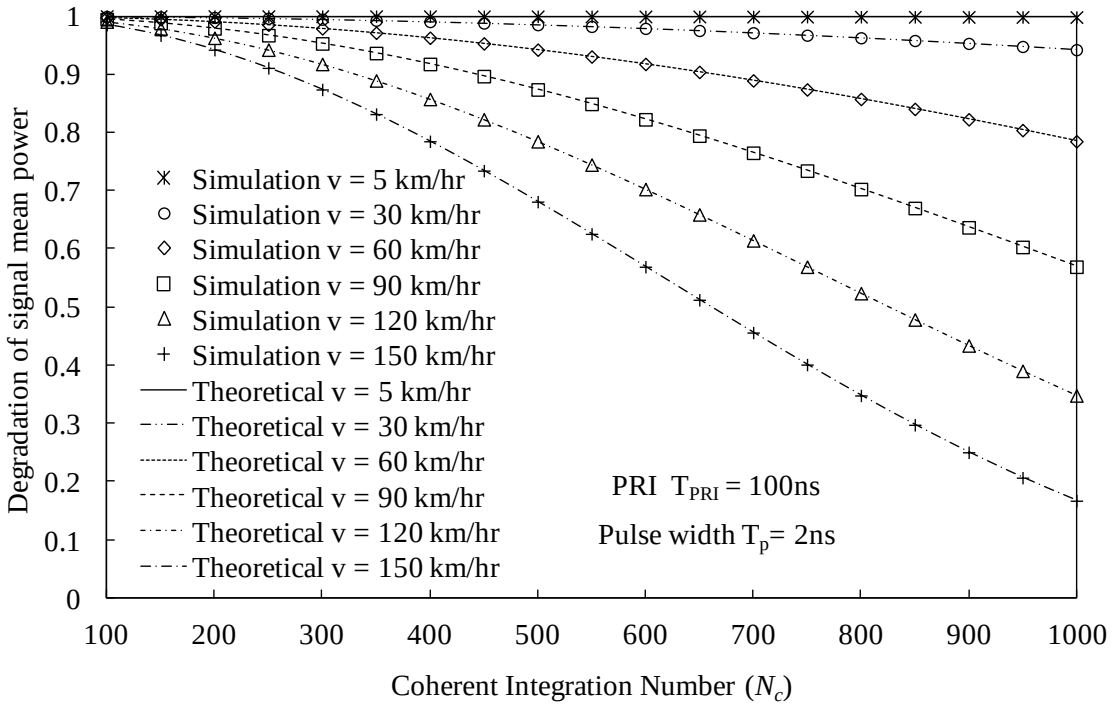

Figure 5.11 Degradation of signal mean power for various velocity (v).

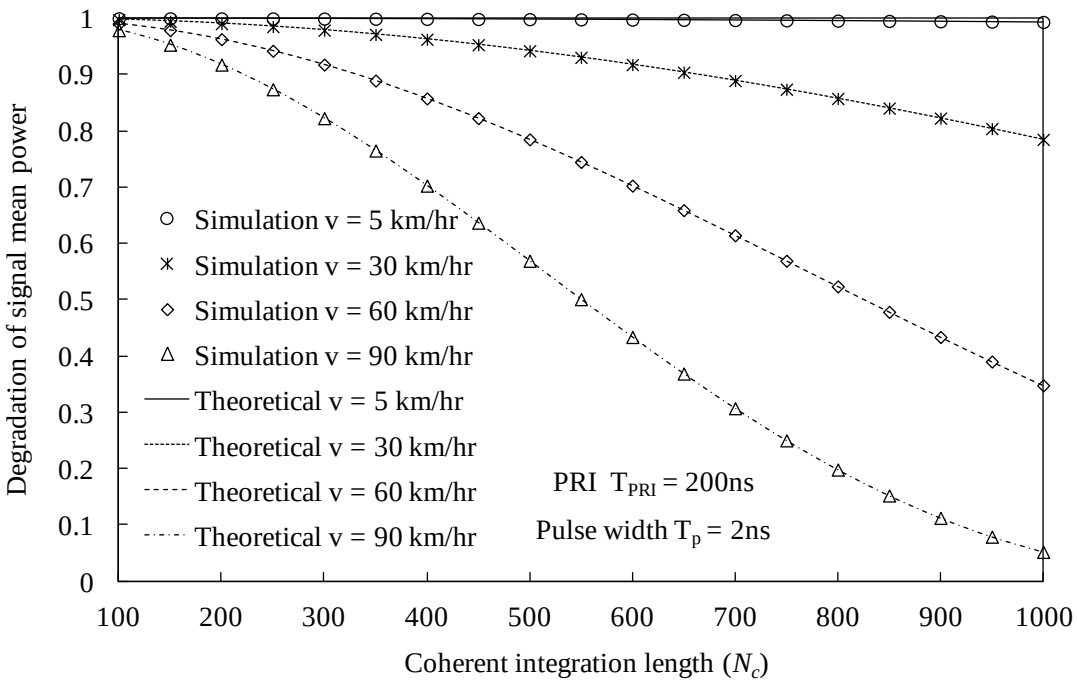

Figure 5.12 Degradation of signal mean power for various velocity (v).

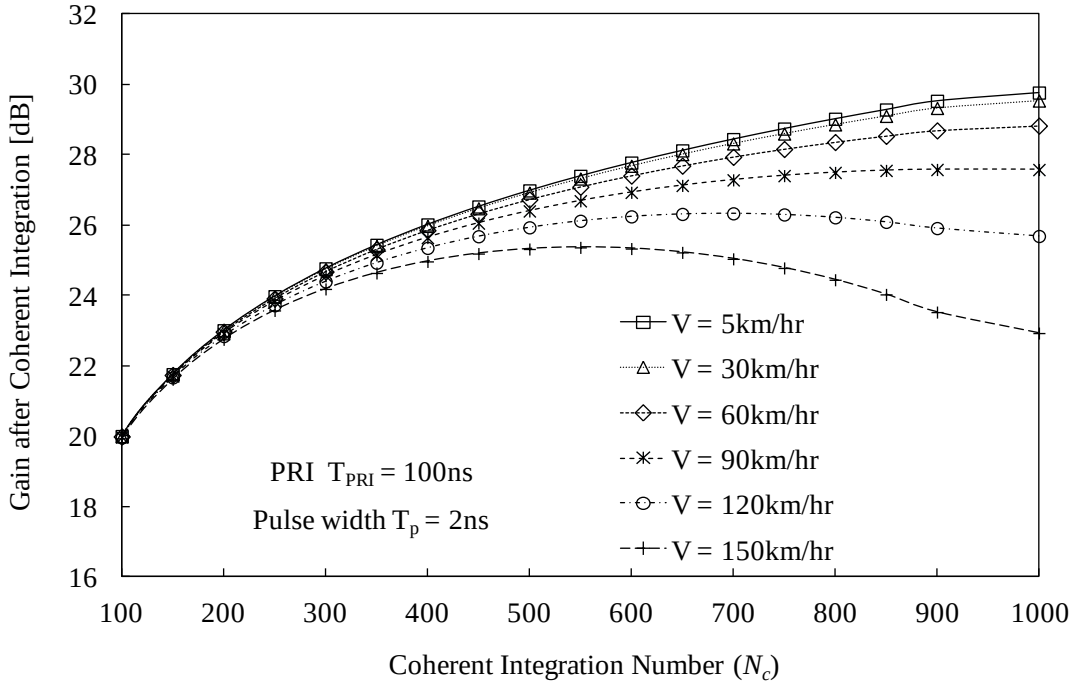

Figure 5.13 Gain obtained at the output of coherent integrator.

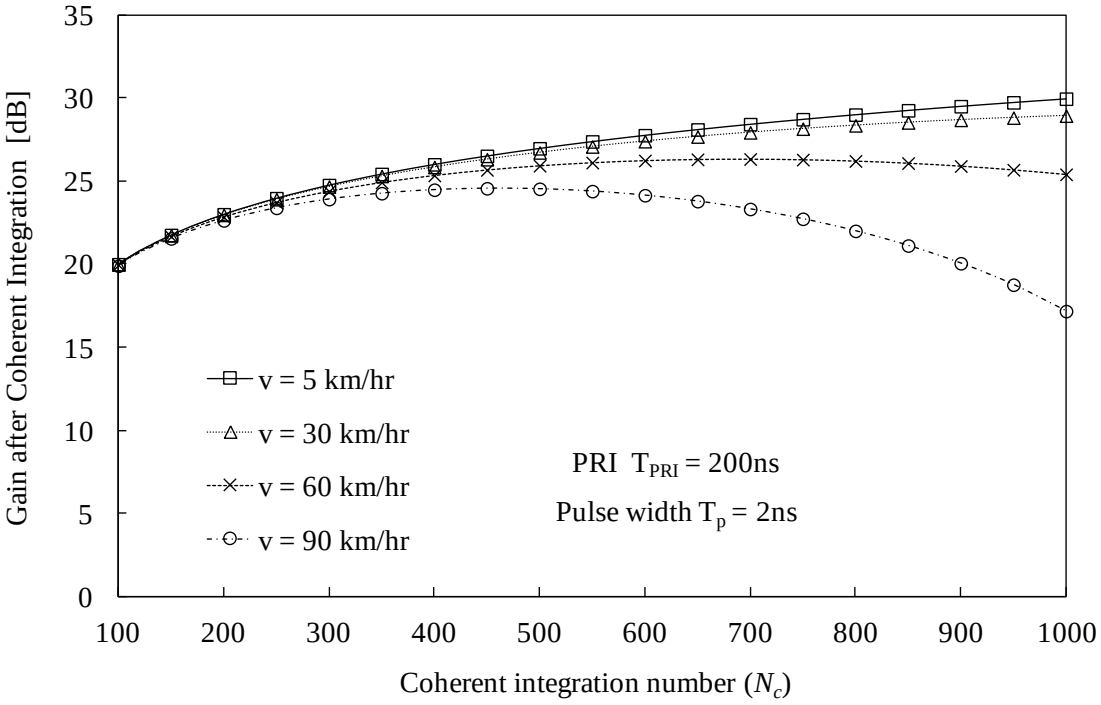

Figure 5.14 Gain obtained at the output of coherent integrator.

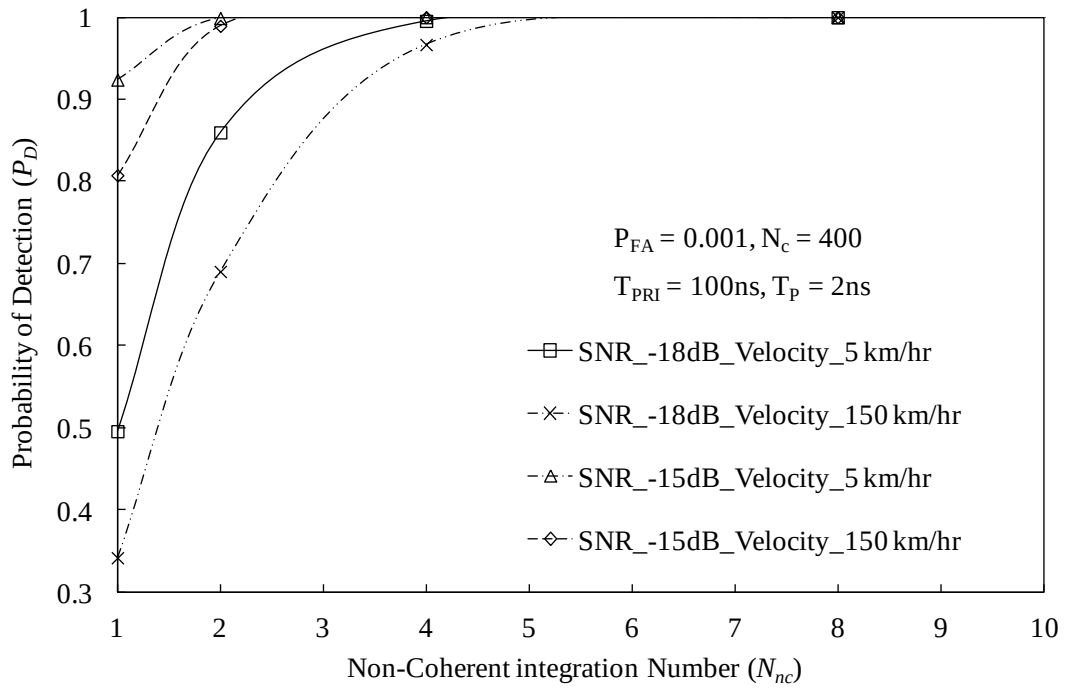

Figure 5.15 P_D for various N_{nc} at the output of non-coherent integrator.

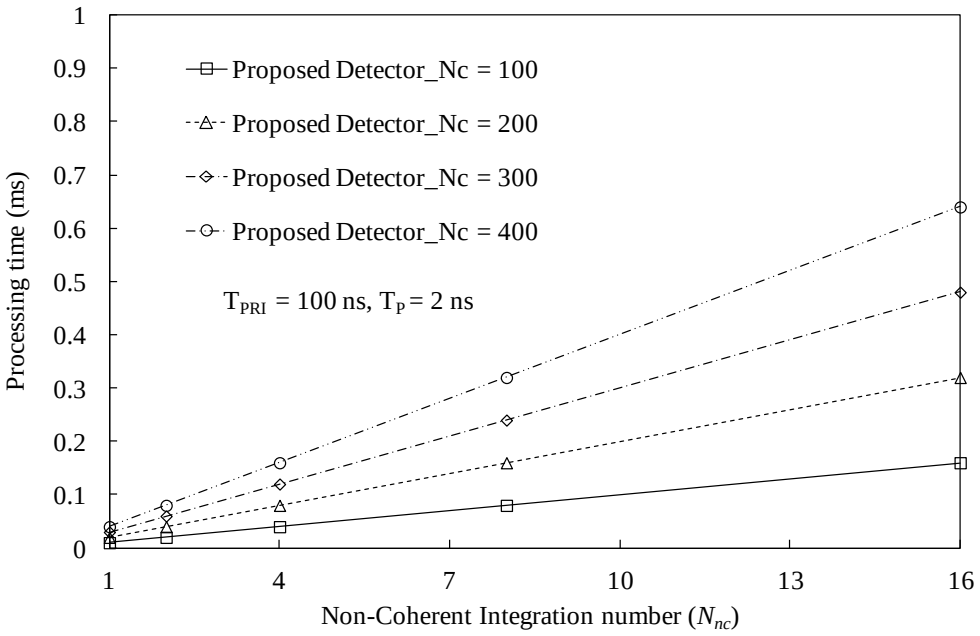

Figure 5.16 Processing time of target range calculator.

Based on the detection probability (P_D) above 0.9 [12], as shown in Fig. 7, the non-coherent integration number (N_{nc}) is selected to be 4. And we can observe that as the input SNR decreases, the non-coherent integration number must be increased in order to achieve detection probability of almost 1 for false alarm probability of 0.001 [12]. However, if the non-coherent integration number (N_{nc}) is increased, we can predict that the processing time (i.e., $N_{nc} \cdot N_c \cdot T_{PRI}$) and hardware complexity of proposed detector are also increased as shown in Fig. 8 [42]. Therefore, we have to choose appropriate non-coherent integration number (N_{nc}). Thus, we use non-coherent integration number of 4 for the proposed detector in simulation so that we are able to achieve detection probability more than 0.9 when the input SNR is -18 dB for maximum target velocity of up to 150 km/hr.

5.4.2 Doppler frequency resolution complexity

In this section, the complexity of Doppler frequency resolution for the proposed detector is presented. The minimum velocity resolution that can be achieved for the selected coherent integration number (N_c) for proposed UWB SRR is mentioned in Table 5.1. The required FFT input time (T_{FFT}), is given by the product of coherent integration length (N_c) and pulse repetition interval (T_{PRI}).

$$T_{FFT} = N_c \times T_{PRI} \tag{5.24}$$

where the Doppler frequency resolution depends on the FFT input time (T_{FFT}) and the number of FFT points (N). Therefore, the minimum Doppler frequency resolution that can be achieved is given by

$$\Delta f_D = (1/T_{FFT})/N \tag{5.25}$$

Fig. 5.16 shows the Doppler frequency resolution that can be achieved by using various FFT point for various coherent integration number (N_c). We can know that as the number of FFT points and coherent integration number are increased, the frequency resolution is decreased. However, if the number of FFT point is increased, the hardware complexity and FFT processing time is also increased. Therefore, we have to choose the appropriate number of FFT point. Thus, we use minimum FFT points as 64 so that we are able to achieve a Doppler frequency resolution of 390.625 Hz which is approximately equal to bicycle speed on road. Finally, the hardware complexity is reduced in proposed method because the FFT processing time and memory requirement is reduced which is discussed in later section of this thesis.

The velocity resolution that can be achieved from the minimum Doppler frequency resolution is

$$\Delta v = -\frac{\Delta f_D \cdot c}{2 \cdot f_c} \tag{5.26}$$

where Δf_D is the Doppler frequency resolution, f_c is the transmitter frequency and c is the speed of light. The proposed UWB SRR detector use selected FFT point (N) as 64, therefore an increase in FFT processing gain is possible at the output of the velocity calculator block as follows; the ratio of output SNR over known input SNR is called improvement factor or processing gain in FFT. The signal to noise ratio (SNR) is defined as the ratio of signal mean power (S^2) to noise power (N_0) of the received signal [43]. The FFT processing gain $G(N)$ obtained at the output of the velocity calculator (i.e., at $F(\hat{k})$) for various FFT points (N) and known input SNR before velocity calculator (i.e., at $\overline{X}(\hat{k})$), can be expressed as follows

$$G(N) = 10\log(N) \tag{5.27}$$

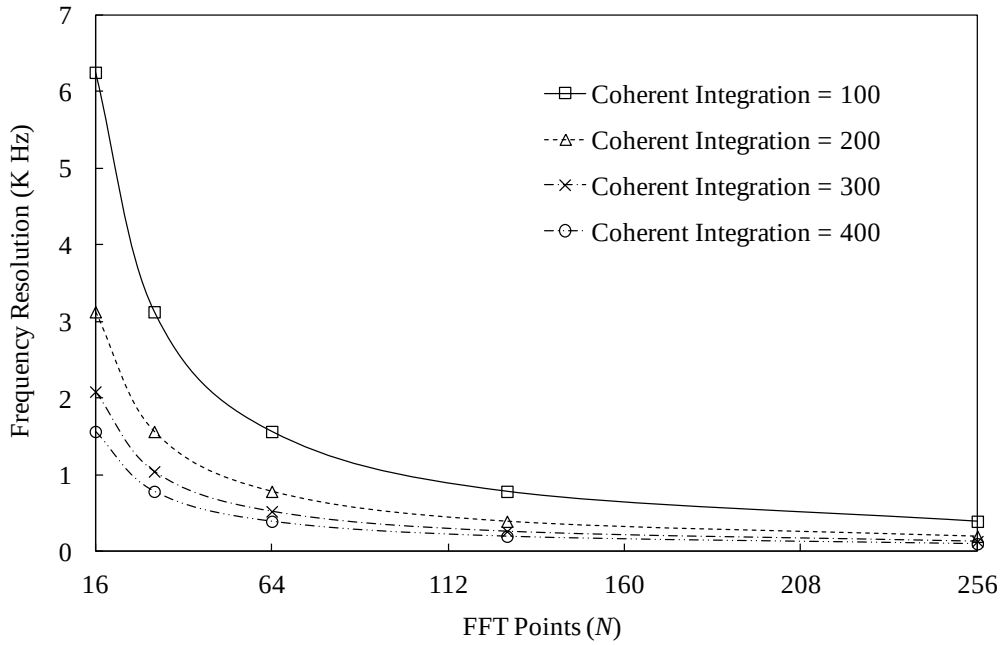

Figure 5.17 FFT points vs Doppler frequency resolution.

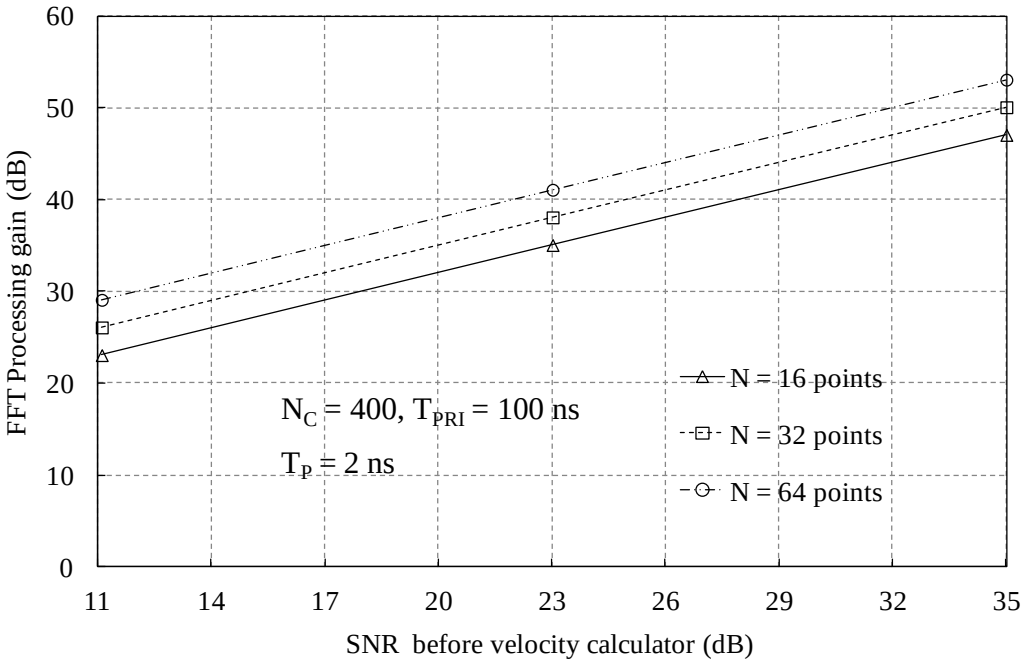

Figure 5.18 FFT processing gain for the proposed UWB SRR.

The FFT processing gain $G(N)$ is increased when N is increased because the noise power (N_0) is reduced as much as N0/N at the output of the velocity calculator block due to the normalization of N from (5.19). Therefore, for every increase in FFT points (N) (i.e., N = 2,4,8,. . . ,64) approximately a 3 dB increase in FFT processing gain $G(N)$ is possible as

shown in Fig. 5.17. The increase in FFT points decreases the frequency resolution that is narrow bandwidth. Also, if the received signal frequency is located in FFT frequency bin then the signal power is high. And, if the received signal frequency is located in middle of two FFT frequency bins the signal power is reduced slightly [45].

5.4.3 Detection Performance of Proposed Detector

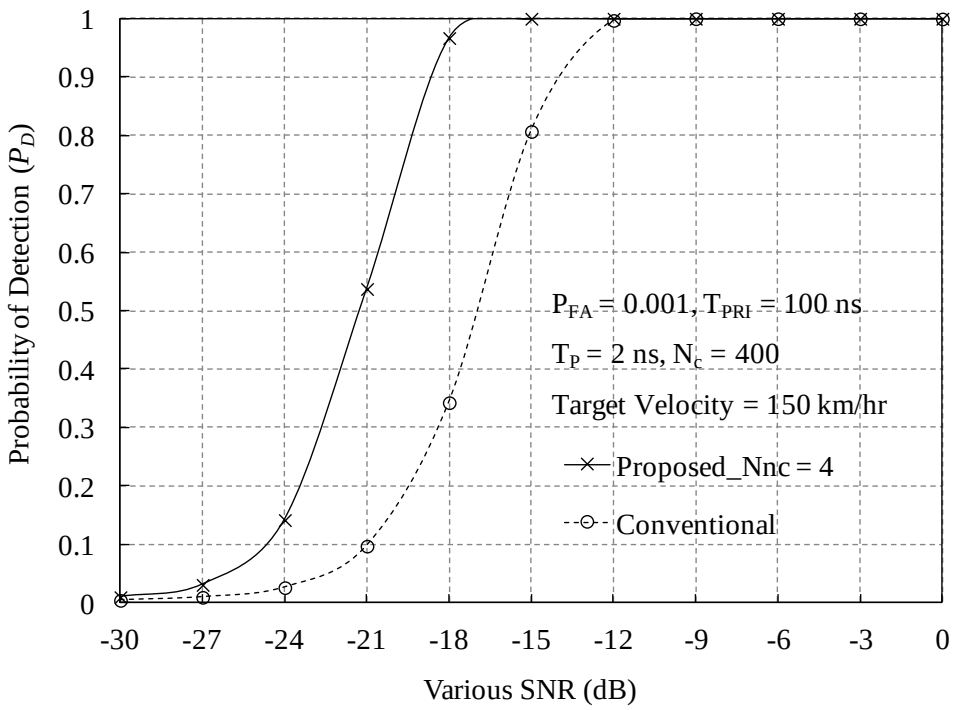

Figure 5.19 The detection probability vs various SNR.

The proposed detector has superior capabilities like FFT measurement time and memory requirement. Finally, the detection probability of the proposed UWB SRR detector is also superior to conventional UWB SRR detector for various $\bar{E}/N_0$ at P_{FA}=0.001 and system parameters mentioned in Table 5.1. The simulation result presented in Fig. 5.18 shows that proposed detector is having detection probability more than 0.9 for $\bar{E}/N_0$ =-18dB, whereas the conventional detector is able to achieve detection probability of approximately 1 only at $\bar{E}/N_0$ = -12dB. The 6dB increase of $\bar{E}/N_0$ in proposed detector is due to the non-coherent integrator block used in the target range calculator of proposed detector as shown in Fig. 5.7 Also, the detection performance of proposed UWB detector is almost same for shorter sampling time based on the range resolution (ΔR) requirement of UWB short range radar system applications such as blind spot, parking aid, stop-and-go, and simple pre-crash [12].

However, the focus of this work is reducing the FFT processing time and the memory requirement of 24 GHz UWB SRR system used for automobile safety applications. Because, the reaction time for the deployment of auto braking systems for stop-and-go, pre-crash, and security devices such as airbags are given high priority in order to avoid accidents or simply to monitor a high traffic road. Therefore, the safety system used in automobile application requires minimum processing time [12]-[42].

5.4.4 FFT Measurement time and Memory requirement

The FFT measurement time is a very important design parameter for developing UWB SRR detector for automobile safety systems such as pre-crash and airbag systems. Therefore, the proposed detector is mainly focused on reducing the FFT measurement time and also the memory requirement in order to reduce the hardware complexity. The FFT measurement time for various velocity resolutions is presented in Fig. 5.19. The required FFT measurement time depends on the velocity resolution and also the number of FFT points. The FFT measurement time is given by

$$T_{FFTmeasure} = N \times K \times T_{FFT} \tag{5.28}$$

where N is the number of FFT points, K is the maximum range gates used in FFT (i.e., for proposed detector K is 1 and for conventional detector K is 50 approximately) and T_{FFT} is the FFT input time for each FFT points as mentioned in (5.20). The FFT measurement time ($T_{FFTmeasure}$) for the proposed detector is approximately 2.56ms for the selected FFT points (N) as mentioned in Table 5.1, because the target velocity is determined for the decided range index ($\hat{k}$) only. Also, we can predict from Fig. 5.15 and 5.19 the total processing time for the proposed detector to determine the target range and velocity sequentially is approximately 2.72ms (i.e., the target range calculator require 0.16ms to determine the target range and target velocity calculator require 2.56ms to determine target velocity). Whereas, the conventional detector requires FFT measurement time ($T_{FFTmeasure}$) of more than 60ms for minimum FFT points (N) as mentioned in Table 5.1 because the conventional detector will use all the range gates to determine the target range and velocity simultaneously.

The implementation of FFT algorithm involves many memory references to access butterfly inputs, twiddle factors. Therefore, high power consumption and memory is required in digital signal processors. The focus of the proposed UWB SRR detector is to reduce the memory requirement and also economically efficient when compared with conventional

UWB SRR detector. The proposed method requires less than 200 bytes (i.e., 2×*K*×*N* bytes for storing complex FFT points and 1×*K*×*N* bytes for storing FFT output) for the selected FFT points (*N*) of 64 points. However, the conventional method requires more than 5 kilo bytes for minimum FFT points (*N*) of 32 [7]-[20]. The memory requirement for the conventional and proposed detector is presented in Fig. 5.20.

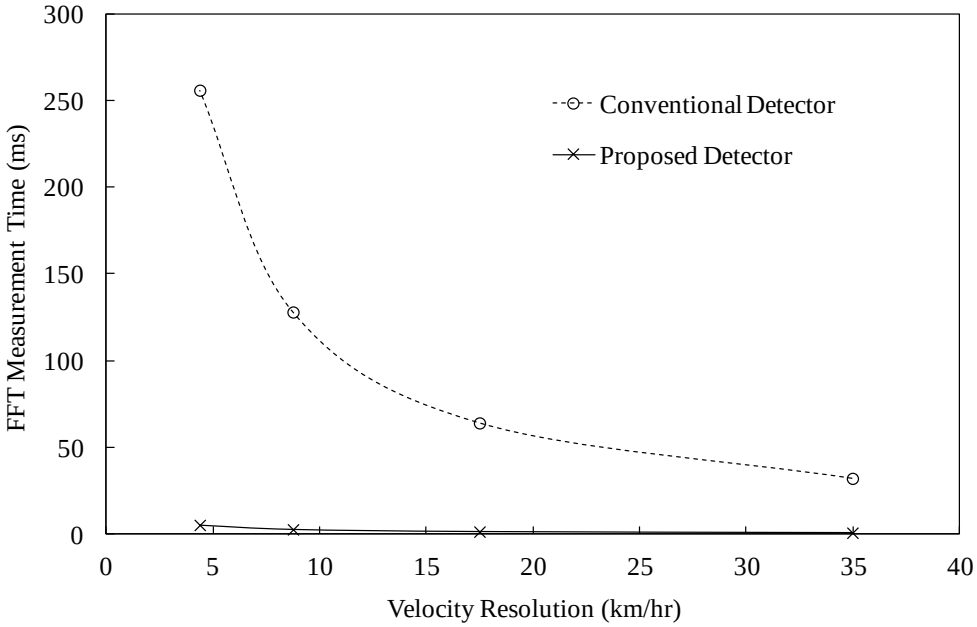

Figure 5.20 Velocity resolution vs FFT measurement time.

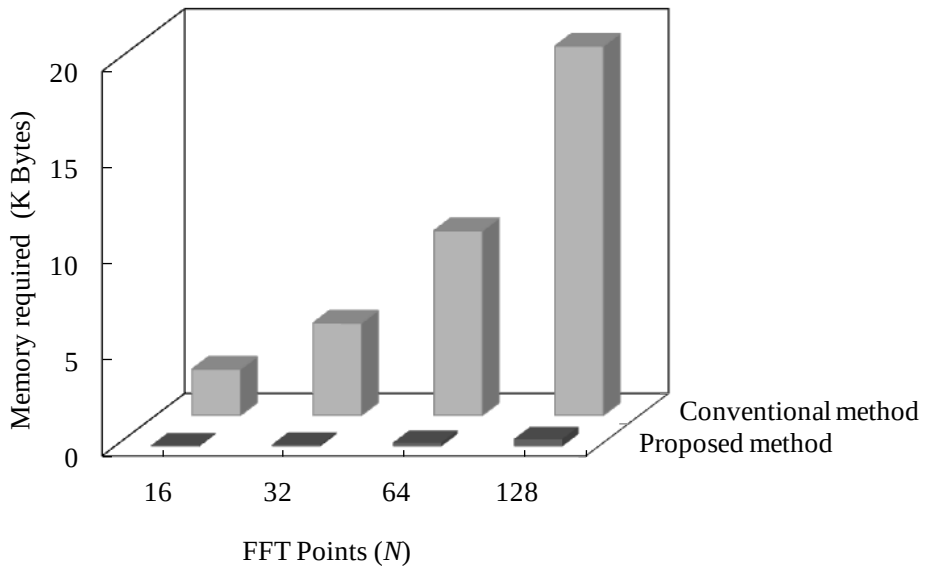

Figure 5.21 FFT points (*N*) vs Memory requirement.

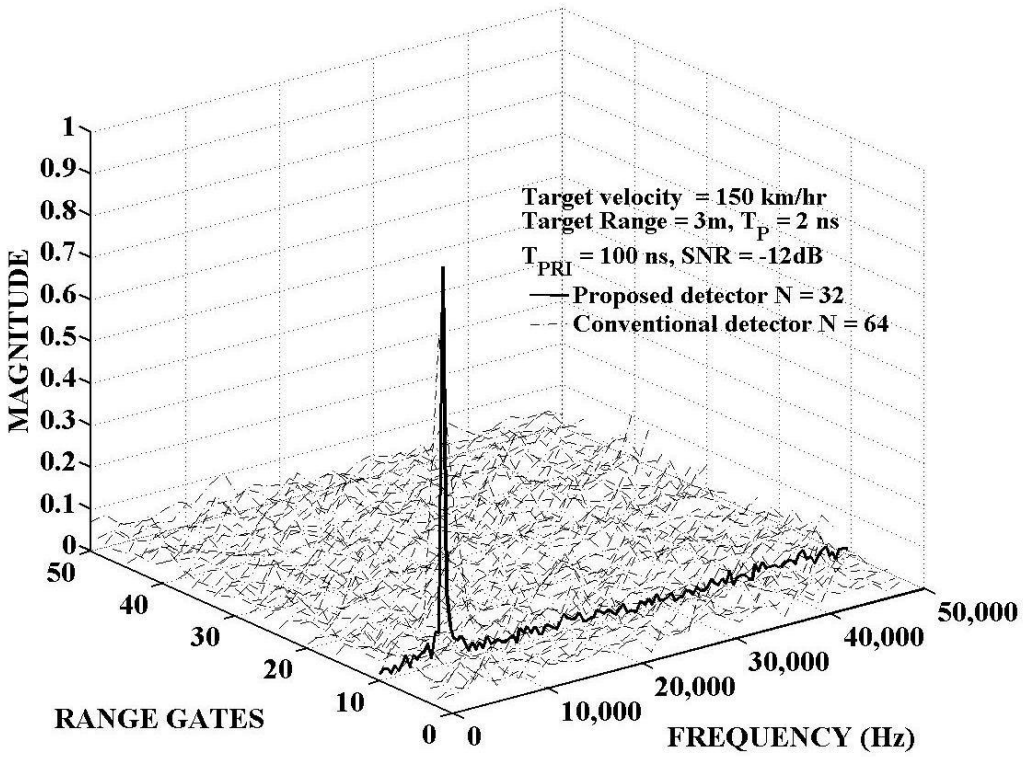

Figure 5.22 3D graph of conventional and proposed detector output.

From the above discussion and simulation results we show that the proposed detector is superior to conventional detector in terms of time, memory efficiency and detection performance. Finally, we compare the proposed and conventional UWB SRR detector output in 3D plot against a background of additive white Gaussian noise as shown in Fig. 5.21, for maximum target velocity of 150 km/hr, assumed target range of 3m and optimized parameters as mentioned in table 5.1.

5.5 Detection Performance of sliding window detector in Gaussian noise environment

The detection probability for various SNR (i.e., Signal-to-Noise ratio) at P_{FA}=0.001 is presented in Fig. 3 [12]. The simulation results in Fig. 3 shows that the proposed detector has a detection probability of more than 0.9 for SNR=-6dB, whereas the conventional detector is able to achieve detection probability of more than 0.9 at SNR = 0dB. The 6dB increase of SNR in the proposed detector is due to the proposed sliding window. The sliding window size (M) is assumed to be 3 in this simulation because the number of reflected echo signals is approximately 3 in [32] for the sample car. Also, we use a minimum number of FFT points (N) of 32 and a coherent integration number (N_c) of 400 so that we are able to achieve a Doppler frequency resolution of 781.25 Hz, which is approximately equal to motorbike speed

on a road [9].

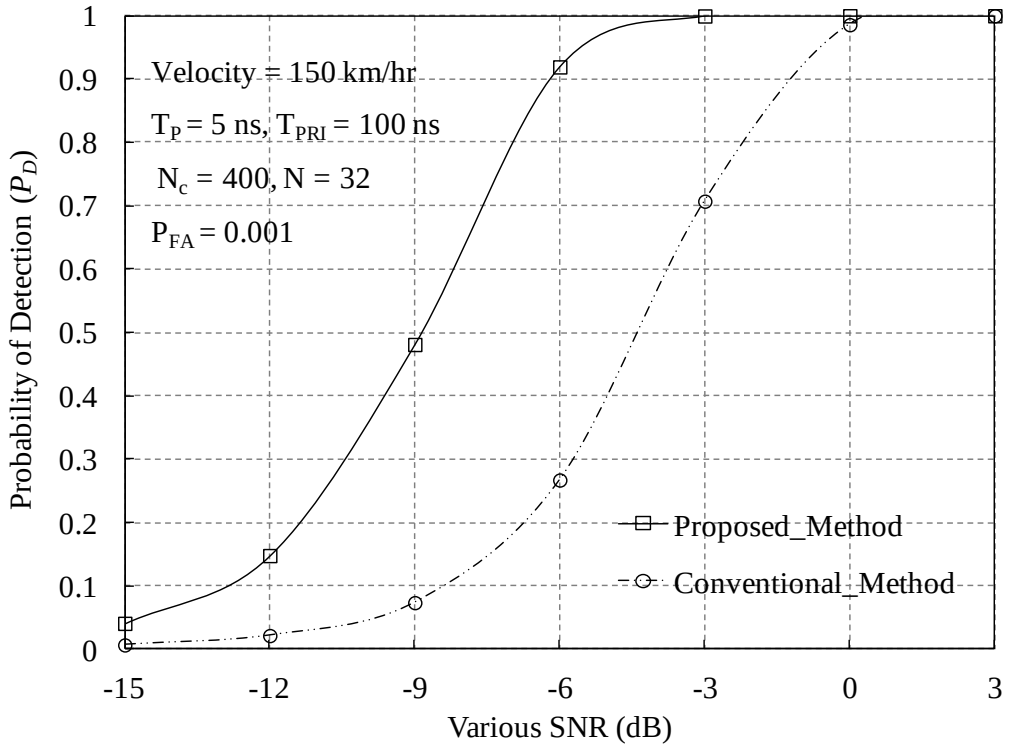

Figure 5.23 The detection probability vs various SNR.

5.6 Simulation result in Coherent Weibull Clutter environment

5.6.1 Probability Density function

The purpose of the simulation is to assess the detection performance of the time and memory efficient detector in correlated coherent weibull clutter environment developed in chapter 2 of this dissertation. The various parameters used in the simulation are as follows; the coherent integration number (N_c) and the non-coherent integration number (N_{nc}). The percentage of total energy reflected from a single target is assumed to be 1. The signal-to-clutter ratio (SCR) is defined as $\bar{E}/C_0$, where $\bar{E}$ represents the total average energy reflected from a single target. The probability density function presented in Fig. 5.24 is obtained for detector parameters such as coherent integration number of 200, non-coherent integration number of 2 and the relative velocity (Δv) is 100 km/hr.

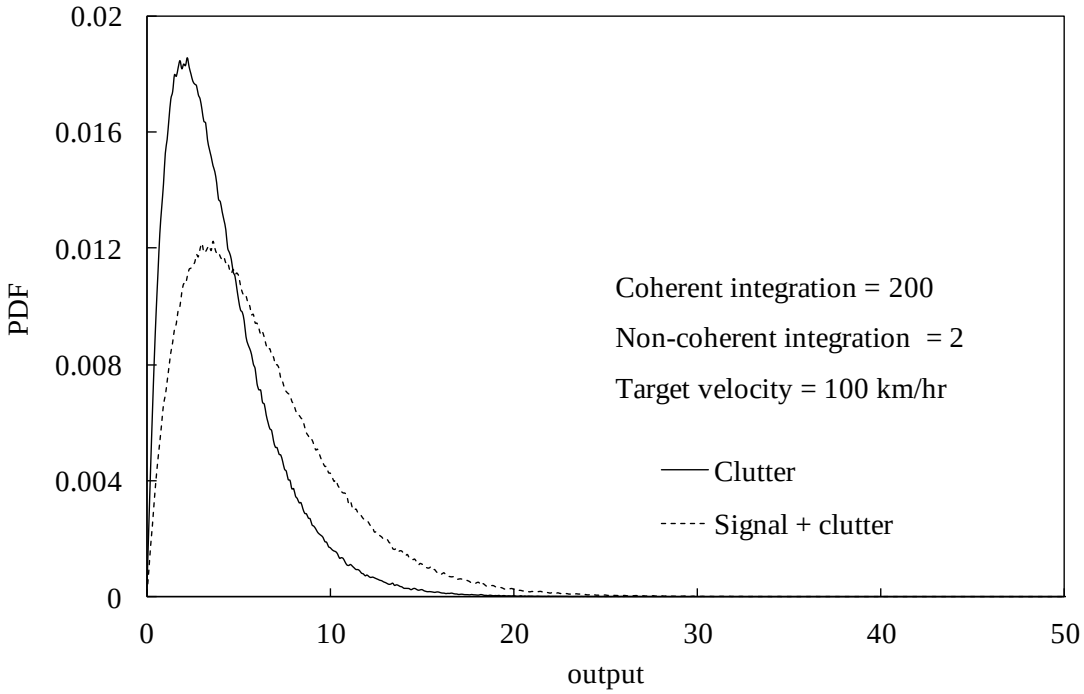

Figure 5.24 The probability density function of coherent weibull clutter.

5.6.2 Region of Convergence

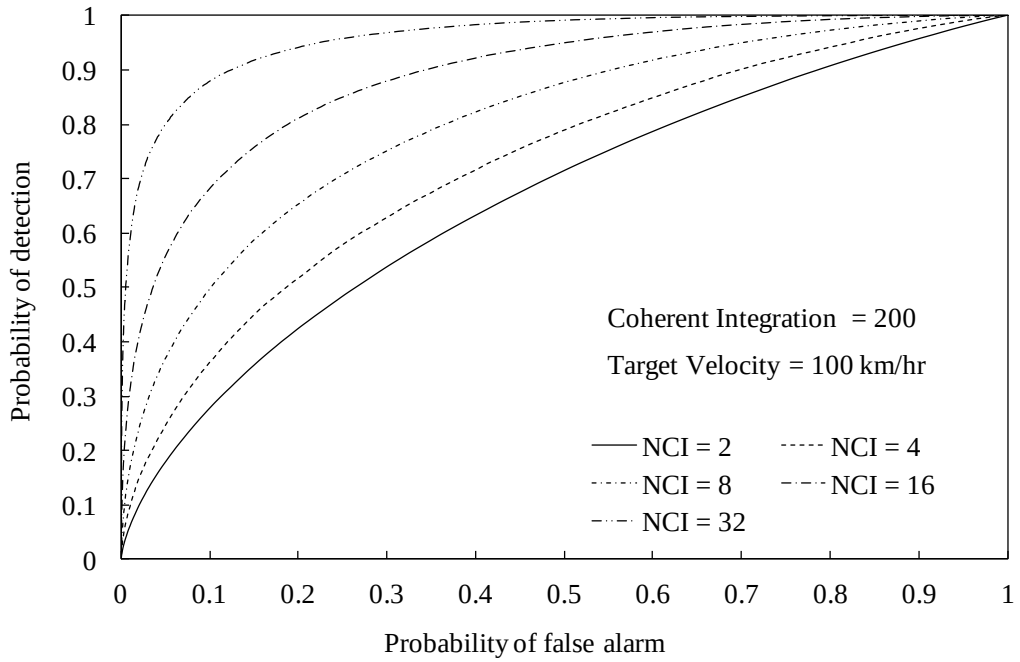

Figure 5.25 ROC curve for various N_{nc}.

Fig. 5.25 presented in this section is the region of convergence curve obtained in coherent weibull clutter environment for various parameters such as coherent integration number of 200, non-coherent integration number of 2, 4, 8, 16 and 32. As we know integration of pulses is generally less effective when detection is limited by clutter, since the clutter echo does not fluctuate from pulse to pulse so there is no much increase in signal-to-clutter ratio. Thus, integration of pulses will not be beneficial. Therefore, the maximum coherent integration number (N_c) of 200 is used in simulation for correlated coherent weibull clutter. The non-coherent integration number (N_{nc}) is increased in order to obtain the maximum detection probability. The coherent weibull clutter model is developed by using the method described in chapter 2 of this dissertation and the experimental datas obtained from [23]. We can predict from Fig. 5.25 as the non-coherent integration number increases the detection performance of the proposed detector is increased also the processing time of the proposed detector will increase. Therefore, appropriate non-coherent integration number must be selected and the clutter must be suppressed in order to get a detection probability of more than 0.9 [12]

6. Conclusions

In this work, the research and development of 24GHz UWB short range radar in automobile application is presented. Detection algorithm for UWB SRR in automotive applications is developed for single stationary and moving target. Also, the optimal parameters of proposed detectors are presented. The detection performance of the proposed detectors is analyzed in a background of Gaussian noise and weibull clutter environment. The correlated coherent weibull clutter model developed in this work is more appropriate to actual road clutter in real situation. Therefore, the clutter model can be used to analyze the detection performance of proposed detectors more efficiently by using Monte Carlo simulation.

The proposed detection algorithm for single stationary target has a squared sliding window in order to combine the reflected signals from the target. The proposed detector has better detection performance in comparison with the conventional detector when the energy reflected from the target is more distributed. Detection depends on the percentage of total energy reflected from each flare point of the target. If the pulse width is very narrow such as UWB signal, then the energy is more spread and the proposed detector with sliding window is superior. Also, in order to get the detection probability above 0.9 for P_{FA}=0.01 in Gaussian noise environment; $\bar{E}/N_0$ is required to be more than 2 dB. Therefore it is necessary that the number of coherent integration must be increased. The detection performance of non-coherent detector such as square law detector for single stationary target in a background of weibull clutter environment is also analyzed. The detection probability is found to be more than 0.9 for coherent and non-coherent integration number of 10 and 8 at P_{FA} = 0.01. The clutter power is almost same for weibull skewness parameter greater than 3. Therefore, the detection probability of square law detector is not decreased unless there is a significant change in received clutter power.

Detection algorithm for single moving target is proposed in this work. Also, the optimal parameters such as the number of coherent integration, non-coherent integration and FFT points under the target maximum relative velocity of up to 150 km/hr is presented. The proposed algorithm first detects the range and then measure the relative velocity of the decided range index by using FFT. The proposed algorithm has superior capabilities like less FFT processing time and memory requirement compared with conventional detector, which is very important in using UWB SRR system for automobile safety applications. Also, we show that the proposed detector detection probability is superior to conventional detector and has a

detection probability of more than 0.9 for P_{FA} = 0.001 and SNR more than -18 dB in AWGN. Finally, the detection performance of the time and memory efficient detector is analyzed in a background of correlated coherent weibull clutter environment developed in this work. Integration of pulses is generally less effective when detection probability is limited by clutter. The clutter echo does not fluctuate from pulse to pulse so there is no much increase in signal-to-clutter ratio. Thus, integration of pulses will not be beneficial. Therefore, the maximum coherent integration number (N_c) of 200 is used in simulation for correlated coherent weibull clutter. The non-coherent integration number (N_{nc}) is increased in order to obtain the maximum detection probability.

Summary

This dissertation presented an overview of UWB radar research and development challenges in the field of automotive applications. The application of 24 GHz Ultra Wide Band short range radar in automobile sector is an emerging hot research topic with an idea to avoid collision and increase road safety and passenger's security. The unique nature of the UWB radar signal by comparing its frequency and bandwidth with the other bands of signal is also presented. The demand for 24 GHz Ultra Wide Band Short Range Radar (UWB SRR) which is used for the target detection has been increased fabulously in automotive sector. In this thesis, the main focus is on the design of 24 GHz UWB SRR detectors for automotive applications. The European commission has identified UWB SRR as a significant technology for the improvement of road safety globally. In Europe, the European commission approved the decision on allocation of the 24 GHz frequency band for automotive applications. According to this decision, the frequency band of 21.625-26.625 GHz is allocated for the use of UWB SRR in automotive applications.

The purpose of this research is to analyze the detection performance of proposed 24 GHz UWB SRR detectors for fixed false alarm probability by using Monte Carlo simulation. The detection performance of proposed detectors is analyzed in Gaussian noise environment and coherent weibull clutter environment for a single stationary and moving target. Therefore, multiple target case is not considered in this dissertation. The coherent weibull clutter model developed in this dissertation is more appropriate to actual road clutter in real situation. Also, the clutter model can be changed to the most appropriate clutter environment for automobile applications by using zero-mean non-linear transformation block (ZMNL) for both stationary and moving target by performing experiments on various road conditions. The proposed sliding window detector has better detection performance in comparison with the conventional detector when the energy reflected from the target is more distributed. As we know detection performance of 24 GHz UWB detectors depends on the percentage of total energy reflected from each flare point of the target. If the pulse width is very narrow such as UWB signal, then the energy is more spread and the proposed detector with sliding window is superior. Finally, the proposed detector is a time and memory efficient UWB SRR detector for measuring the target maximum relative velocity of up to 150 km/hr. The proposed pulse radar first decides the target range and then computes the target velocity by using FFT at the decided range index sequentially. Therefore, we can reduce the FFT processing time and the

memory requirement of proposed 24 GHz UWB SRR detector used for automobile safety applications. The safety system used in automobile applications requires minimum processing time and less memory in order to reduce the hardware complexity because, the reaction time for the deployment of auto braking systems for pre-crash and security devices such as airbags are given high priority in order to avoid accidents or simply to monitor a high traffic road.

References

1. Karl M. Strohm, et al., "Development of Future Short Range Radar Technology," *Radar Conference*, 2005.
2. The CEPT Report 37 to the European Commission in response to part 2 mandate automotive short range radar 25 June 2010.
3. http://europa.eu.int/information_society/programmes/esafety/index_en.htm
4. James D.Taylor, ed., "Ultra-Wideband Radars Technology: Main Features Ultra-Wideband (UWB) Radars and differences from common Narrowband Radars", *CRC Press*, 2001.
5. James D.Taylor, ed., "Introduction to Ultra-Wideband Radars (UWB) systems", *Boca Raton, FL*, 1995.
6. Merrill I. Skolnik, Introduction to radar systems, *Third Edition: McGraw-Hill*, 2001.
7. Hermann Rohling, Frank Kruse, et al.: 'Target Classification with a narrowband 24 GHz Radar system', *1st international workshop on Intelligent Transportation*, WIT 2004.
8. http://www.smartmicro.de/
9. Michael Klitz, "An Automotive Short Range High Resolution Pulse Radar Network", Ph. D. Dissertation, Jan. 2002.
10. Michael Klitz, H. Rohling, "24 GHz Radar Sensors for automotive Applications," *Journal of Telecommunications and information technology*, 2001.
11. F. Kruse, F. Folster, M. Ahrholdt, M.-M Meinecke, H. Rohling: "Object Classification with Automotive Radar" International Radar Symposium, Dresden/Germany, September 30 – October 2, 2003.
12. Ian Gresham, Alan Jenkins, Robert Egri, et al., "Ultra-Wideband Radar Sensors for Short Range Vehicular Applications," *IEEE transactions on microwave theory and techniques*, Vol. 52, No. 9, September 2004.
13. Dr. Ralph Mende, Marc Behrens, Dr Stefan Milch "A 24 GHz ACC Radar Sensor" February 28, 2005.
14. Meineckke, Marc-Michael; To, Thanh-Binh; Obermann, Jan: "A24 GHz radar-based automotive pre-crash system" International Workshop on Intelligent Transportation, Hamburg/Germany, March 23-24, 2004.

15. Hermann Rohling, Marc-Michael Meinecke: Waveform Design Principles for Automotive Radar Systems, CIE International Conference on Radar, Beijing, China, October 2001
16. Hermann Rohling, Florian Folster, Marc-Micharl Meinecke, Ralph Mende: A new Generation of Automotive Radar Waveform Design Techniques. IEE Conference. On Waveform Diversity and Design, November 2004, Edinburgh/UK.
17. Kouemou, G. and Opitz, F.: Impact of Wavelet Based Signal Processing Methods in Radar Classification Systems Using Hidden Markov Models, in: Proc. Of the 2008 International Radar Symposium, Wroclaw, Poland, 21-23 May 2008, 1-4, 2008.
18. He, F., Huang, X., Liu, C., Zhou, Z., and Fan, C.: Modeling and Simulation Study on Radar Doppler Signatures of Pedestrian, in: Proc. Of the 2010 IEEE Radar Conference, Washington DC, USA, 10-14 May 2010, 1322-1326, 2010.
19. Benitez, D. and Zhazhang, J.: Method for Human only Activity Detection Based on Radar Signals, U.S. Patent Application US2011/0032139A1, 2011.
20. A. Bartsch, F.Fitzek, and R.H.Rasshofer.: "Pedestrian recognition using automotive radar sensors" Journal of Advances in Radio Science, 10. 45-55, 2012.
21. Bruno Neri & Sergio Saponara.: "Advances in Technologies, Architectures, and Applications of Highly-Integrated Low-Power Radars" IEEE A&E Systems Magazine, January 2012.
22. Ralph Mende, Marc Behrens: The UMRR 24 GHz Radar Sensor Family for short and medium range applications, ATA EL conference, Juni 2004, Parma/IT
23. Isamu Matsunami, Youichiro Nakahata, Katsushi Ono, Yuusei Noguchi and Akihiro Kajiwara, "Empirical Study on Ultra-Wideband" Vehicular Technology Conference, 2008 fall.
24. S.Sayama, M. Sekine, "Observations and suppression of sea ice clutter by means of millimeter wave radar," IEICE Trans Commun (Japanese Edition)., vol.J86-B, no.7, pp. 1104-1111, July 2002.
25. S.Sayama, M. Sekine, "Amplitude statistics of ground clutter included town using millimeter wave radar," IEICE Trans. Commun (Japanese Edition)., vol.J86-B, no.5, pp. 829-836, may 2003.
26. Farina, A., Russo, A., Scannapieco, F., and Barbarossa, F: "Theory of radar detection in coherent Weibull clutter", *IEE Proc. F,* 1987, **134,** (2), pp. 174-190.
27. Hawkes, C.W., and Haykin, S.S.: "Modeling of clutter for coherent pulsed radar", IEEE ***Trans.,*** 1975, IT-21, pp. 703-707.

28. Abramowitz, M., and Stegan, LA.: "*Handbook of mathematical functions*" (Dover Publications Inc., New York, 1972.
29. John Makhoul.: "Linear Prediction: A Tutorial Review" IEEE *Proceedings*, VOL. 63, No. 4, April 1975.
30. Charles W. Therrien.: "Discrete Random Signals and Statistical Signal Processing". ISBN 0-13-852112-3.
31. Gang Li, Kai-Bor Yu.: "Modelling and simulation of coherent weibull clutter". IEE *proceedings*, 136, Pt. F, 1 (Feb 1989), 2-12.
32. G. Minkler and J. Minkler, "The Principles of Automatic Radar Detection In Clutter CFAR", *Magellan Book Company*, 1990.
33. P.K. Hughes, "A High-Resolution Radar Detection Strategy," *IEEE Transaction on Aerospace and Electronic Systems*, Vol. ASE-19, NO. 5, pp. 663-667, Sept. 1983
34. Gerard A. Van Der Spek, "Detection of a Distributed Target," *IEEE Transaction on Aerospace and Electronic Systems*, Vol. ASE-7, NO. 5, pp. 922-931, Sept. 1971
35. Ian Oppermann, Matti Hamalainen and Jari Iinatti, "UWB Theory and Applications", *John Wiley & Sons Ltd*, 2004.
36. John G. Proakis, Digital Communications, *McGraw-Hill*, 2001.
37. Purushothaman Surendran, Seok Jun Ko, Sang-Dong Kim, and Jong-Hun Lee, "A Novel Detection Algorithm for Ultra Wide Band Short Range Radar in Automobile Application", *IEEE VTC2010 Spring*, May 2010.
38. K.S. Miller and R.I. Bernstein, "An analysis of coherent integration and its application to signal detection," *IRE transactions on information theory 1957.*
39. W.Weidmann and D. Steinbuch, "A High Resolution radar for short range automotive applications", in *28th European Microwave Conference, Amsterdam*, Netherlands, 1998, pp. 590–594.
40. Mende R, Zander: "A multifunctional Automotive Short Range Radar System", *German Radar Symposium, GRS2000*, Berlin, October 10–11, 2000.
41. Jong-Hun Lee, Myung-Hun Jang, and Seok-Jun Ko, "Measuring the target range and relative velocity in UWB radar for automobile applications," *Proceedings of the 8-th European Radar Conference 2011*.
42. T. Wilson. (1994, Feb) "IVHS countermeasures for rear-end collisions, task 1: Volume VI-Human factor studies", *U.S Dept. Transportation, Washington, DC. [Online]*. DOT Rep. HS 808 565.

43. Leon-Garcia, “Probability and Random Processes for Electrical Engineering”, *second edition Addison-Wesley Publishing Company* ISBN 0-321-18963-9.
44. Yuke Wang, Yiyan (Felix) Tang, Yingtao Jiang, “Novel Memory Reference Reduction Methods for FFT Implementations on DSP Processors” *IEEE transactions on signal processing*, Vol. 55, No. 5, May 2007.
45. Bassem R. Mahafza, “Radar Systems Analysis and Design Using MATLAB”, *by Chapman & Hall/CRC*, 2000. ISBN 1-58488-182.
46. Marc-Michael Meinecke; Marian Andrzej Obojski: “Enhancing Pedestrian Safety by using the SAVE-U pre-crash system.
47. S. Munder, M.-M. Meinecke, D.M. Gavrila, M. A. Obojski “SAVE-U: Driver Warning and Vehicle Actuator Concepts (Deliverable D22).” EU-Project SAVE-U, www.save-u.org, 19-08-2005.
48. Meinecke, Marc-Michael, Holze, Raimond, *et al*. “Side-Pre-Crash Sensing system for Automatic Vehicle Height Level Adaptation” 3rd International Workshop on Intelligent Transportation (WIT), Hamburg/Germany, March 14-15, 2006.
49. Freund, S.: Object Recognition from Radar Raw Data Using Image Processing Methods, Diploma thesis, Ludwigs-Maximilians-Universitat Munich, Institute of Computer Science, Munich, Germany, 2007.
50. J.V. Difranco and W.L. Rubin, Radar detection, Prentice-Hall, Englewood Cliffs, NJ, 1968.